UC Berkeley
UC Berkeley Electronic Theses and Dissertations

Title
The Descent of Ant

Permalink
https://escholarship.org/uc/item/64k8n0z3

Author
Munk, Jonathan Daniel

Publication Date
2011

Peer reviewed|Thesis/dissertation

eScholarship.org Powered by the California Digital Library
University of California

The Descent of Ant

by

Jonathan Daniel Munk

A dissertation submitted in partial satisfaction of the
requirements for the degree of
Doctor of Philosophy

in

Integrative Biology

in the

Graduate Division

of the

University of California, Berkeley

Committee in charge:

Professor Mimi A.R. Koehl, Chair
Professor Robert Dudley, Co-chair
Professor Mark Stacey
Professor Stephen P. Yanoviak

Fall 2011

The Descent of Ant

Copyright 2011
by
Jonathan Daniel Munk

Abstract

The Descent of Ant

by

Jonathan Daniel Munk

Doctor of Philosophy in Integrative Biology

University of California, Berkeley

Professor Mimi A.R. Koehl, Chair

Professor Robert Dudley, Co-chair

The gliding ant *Cephalotes atratus* was the first described example of an animal capable of sophisticated aerodynamic control in the absence of obvious morphological adaptations for aerial behavior. In this thesis I present a series of studies aimed at quantitatively describing the aerodynamics of stability and control in *C. atratus*, using a combination of field studies and modeling experiments.

In Chapter 1, I present a quantitative analysis of the 3-D trajectories followed by gliding *C. atratus* ants, measured using multiple-camera photogrammetric techniques in a natural rainforest environment. These trajectories represent the first attempt to measure gliding trajectories in a natural environment for any animal, and provide a data-driven view of variation in aerodynamic characteristics and trajectory shape across multiple *C. atratus* individuals. The 3-D analysis conducted in Chapter 1 shows that *C. atratus* reach equilibrium glide speed ($\mu = 4.12, \sigma = 0.59$) within 1 s of dropping from the canopy. Lift-to-drag ratios during equilibrium gliding were higher for ants dropped further from a target tree trunk, but for a given horizontal distance between drop point and target tree trunk, lift-to-drag ratios were not observed to vary significantly with size.

In Chapter 2, I present a kinematic analysis of the use of posture by gliding *C. atratus* ants. By dropping *C. atratus* workers into a vertical wind tunnel and analysing their behaviors using multiple cameras and posture estimation techniques, I show that gliding *C. atratus* ants immediately adopt a parachuting pose with the legs elevated above the body axis when dropped. Changes in gaster flexion angle as well as the fore-aft angles of the mid- and hind-legs were observed in all analysed bouts of gliding, but statistical attempts to find correlations between static postures and body kinematics were ultimately unsuccessful due to the rapidity with which ants in the wind tunnel changed posture.

In Chapter 3, I present a quantitative description of stability and control in gliding ants, using dynamically scaled physical models to show how the postural changes discovered in Chapter 2 result in changes in the aerodynamic forces experienced by the ant as well as its stable body orientation. I show that the standard gliding posture adopted by a falling

C. atratus ant is aerodynamically stable in both pitch and roll, and that subtle changes in posture and the location of the center of mass result in significant changes in the magnitude and direction of the aerodynamic force experienced by the ant. The postures associated with pitching and turning maneuvers, moreover, are also aerodynamically stable, which means that gliding *C. atratus* ants do not jeopardize their stability while conducting aerial maneuvers. Finally, by testing the aerodynamic performance of a flat, splayed-out posture for *C. atratus*, as well as a modified *C. atratus* with shortened legs, I show that the elevated-legs posture adopted by *C. atratus* is fundamental to its stability, and that leg length is a key predictor of aerodynamic stability and control.

For The Sizzler

Contents

List of Figures

List of Tables

Acknowledgments

This thesis would not have been possible without the contributions of a great many people, all of whom have contributed in significant ways to the formation of the initial ideas, collection of data, design of analysis methods, writing, the mental well-being and happiness of myself, or combinations thereof.

First and foremost, I would like to thank my advisors, Robert Dudley and Mimi Koehl. I have learned a great deal from them over the course of my studies at Berkeley, but perhaps the most important lesson I have learned is that in biology it tends to be important to pay attention to what the actual organism you claim to be studying does in the real world — that, and that sometimes a stick and a piece of duct tape is an acceptable substitute for a custom part finely machined from aircraft-grade aluminum. Their guidance and support has been invaluable in the effort to bring this project to completion, and their comments on the work as it evolved vastly improved the final product.

I would also like to thank Steve Yanoviak, whose invaluable instruction has included the art of climbing trees without falling down, where to find the good ants on BCI, and tips on photography — not to mention being a most excellent conversationalist over a bottle of fine rum and one of the finest naturalists and field scientists I have had the pleasure of meeting. Steve's enthusiasm and encouragement helped steer me through some dark waters, especially during the writing phase.

To Mark Stacey, I am grateful for the guidance you provided me in the course of building up a reasonable aerodynamics and fluid dynamics background in preparation for taking on this project. I can only hope that I have made an even number of sign errors in the mathematics.

To those members of my qualifying exam committee not already mentioned, Jim McGuire and Sheila Patek, thank you for all of the conversations about comparative methods and ideas about conducting biomechanical research within a phylogenetic framework. It turned out that I had plenty of work cut out for me in studying a single species, but one of these days I'll get around to all those broad comparative questions we spent hours talking about back in the day.

I am deeply grateful to the undergraduates who have assisted me with various aspects of data collection and analysis over the years: Tyson Read, Greg Reynolds, Nicole Soltis, Justine Velasco, Karin Harrington, Elliot Chan, Allan Woodworth and Jeffrey Yeh. It is probably somewhat optimistic to hope that you did not feel mildly exploited for manual labor, especially those of you who were on digitization duty, but I hope it was at least a little bit fun.

I am also grateful for my family: for the Sizzler, who always made sure that there was good physics in what I was doing; for Dr. Bloodnut, who's a top bloke and good value, even for a physician; for Chuckie and Pete, who were always ready to step in and prevent me from becoming sane on the odd occasions when that spectre reared its ugly and unfamiliar head; for Irene, whose hospitality I have mercilessly abused several times over the years; and for

Mom, who the Sizzler tells me would have been proud (and I think he may actually be right on this one).

To the friends I have made in graduate school, whose advice, scientific awesomeness, conversational ability, and tolerance for alcohol have helped me so much over the years — Shai Revzen, Dennis Evangelista, Sam Burden, Lindsay Waldrop, Eve Robinson, Kelly Dorgan, Jim Kreft, Rideyback, Simon Sponberg, Jenny McGuire, Erin Meyer, Becca Calisi, Ben Carter, Chris Nasrallah, Sarah Werning, The Jolly Roger, and Lord Biggleswade — thank you all so much. 'Tis a fine thing indeed to have such magnificent friends.

And most of all, thank you Abber. Your support and encouragement has meant more to me than I could ever hope to express here. I couldn't have done this without you.

Chapter 1

Skydivers under the canopy: the twists and turns of gliding ants

1.1 Introduction

The discovery of directed aerial descent in wingless workers of the canopy ant species *Cephalotes atratus* by Yanoviak et al. (2005) was the first described example of sophisticated aerodynamic control in an animal without obvious morphological adaptations for aerial behavior. Following a fall from the rainforest canopy, *C. atratus* workers execute a series of maneuvers by which they stabilize their orientation, visually target a nearby tree-trunk, and finally glide to and land upon that tree trunk. *C. atratus* was also the first discovered example of a backwards gliding animal: by painting the hind-legs of the subjects in their trials, Yanoviak et al. (2005) observed that *C. atratus* approaches its target tree with its hind-legs and abdomen leading.

While it may be tempting to posit that the study of gliding in *C. atratus* could shed light on the evolutionary origins of powered flight in insects, it is important to note that ants comprise a highly-derived lineage of insects, and the workers are secondarily wingless. While gliding has been observed in ancestrally wingless bristletails (Yanoviak et al., 2009), ablation studies conducted separately on *C. atratus* ants and bristletails have shown that the bristletails rely on their caudal filaments to allow for aerodynamic stability and control (Yanoviak et al., 2009), whereas for *C. atratus* the abdomen and hind-legs are the most important features for enabling aerodynamic performance (Yanoviak et al., 2010).

Nevertheless, the fact that these ants are using presumably non-adapted structures to perform sophisticated aerial maneuvers while falling from the canopy makes them a fascinating system for the broader study of the aerodynamic role of non-wing structures in controlling flight in insects. While many flying insects are known to use their legs and abdomen as secondary control surfaces to the wings to facilitate steering control (e.g. Arbas (1986); Camhi (1970); Hinterwirth and Daniel (2010) among many others, reviewed in Taylor (2001)) and mitigate perturbations due to turbulence (Combes and Dudley, 2009), the role

played by these features is secondary to the primary role played by the wings. The example of *C. atratus* has shown, fascinatingly, that even in the absence of wings these control surfaces can provide ants with the ability to significantly alter the trajectory of their descent in a controlled, targeted fashion.

Understanding how *C. atratus* ants achieve aerodynamic stability and control without wings begins with measuring the trajectories that they follow as they return to the target tree trunk. Yanoviak et al. (2005) provided a 2-dimensional trajectory analysis of a few select ants gliding to a white cloth column (simulating a tree trunk) in a controlled, non-forest environment, but the results of their analysis indicate that the surrogate tree in this experiment did not elicit identical performance to that observed in a natural environment. Ants dropped from the canopy exhibited a >90% success rate in targeting and landing upon a tree trunk when dropped in a natural forest environment, whereas of the 28 ants that were dropped in the controlled experiment only 6 successfully targeted the surrogate tree. Furthermore, videos of ants gliding to a target tree in a natural environment (Yanoviak et al. (2005), supplementary materials) feature spiralling motion not captured by the linear trajectories observed in the controlled experiment. Measurement of the curvature of natural trajectories of gliding *C. atratus* ants would help to quantify the degree of control *C. atratus* workers have over the shape of their trajectory.

Yanoviak et al. (2005) also reported an inverse correlation between body size and glide index, where glide index was defined as the ratio of the horizontal and vertical distances between the point from which the experimental subject was released and its landing point on the target tree. This was attributed to an expectation that smaller ants should reach a minimum viable glide velocity ($U_{\min}$, *sensu* Kingsolver and Koehl (1994)). Equilibrium gliding requires that the gravitational force acting on a glider be balanced by the net aerodynamic force, where the former is proportional to mass and the latter is proportional to surface area; as the surface area to mass ratio is expected to be proportional to $M^{-\frac{1}{3}}$ (see, e.g., Alexander (2003)), smaller ants are expected to reach equilibrium glide velocity after a shorter period of falling time than larger ants. This phenomenon is expected to cause the glide index for larger ants to decrease, but is not the only potentially contributing factor. An additional possible contributing factor might be that the lift-to-drag ratio for a *C. atratus* ant body shape is not constant over the Reynolds number range spanned by falling *C. atratus* ants of differing body size; if this were the case, we would expect to see smaller ants with lower equilibrium glide velocities exhibiting a shallower glide angle than larger ants due to their increased lift-to-drag ratio (see Vogel (1994) for further discussion of the effect of Reynolds number on lift and drag). Another hypothesis could be that smaller ants are more maneuverable than larger ants; in this case we would expect the trajectories followed by smaller ants to exhibit curves of a tighter radius in the early, targeting phase of their descent, followed by a more direct path to the target once the targeted lateral motion phase of the glide has begun.

In this study I present the first 3-dimensional trajectories ever obtained for a gliding animal in a completely natural field environment, characterizing the variation in paths followed by gliding *C. atratus* worker ants towards a target tree after being dropped from the

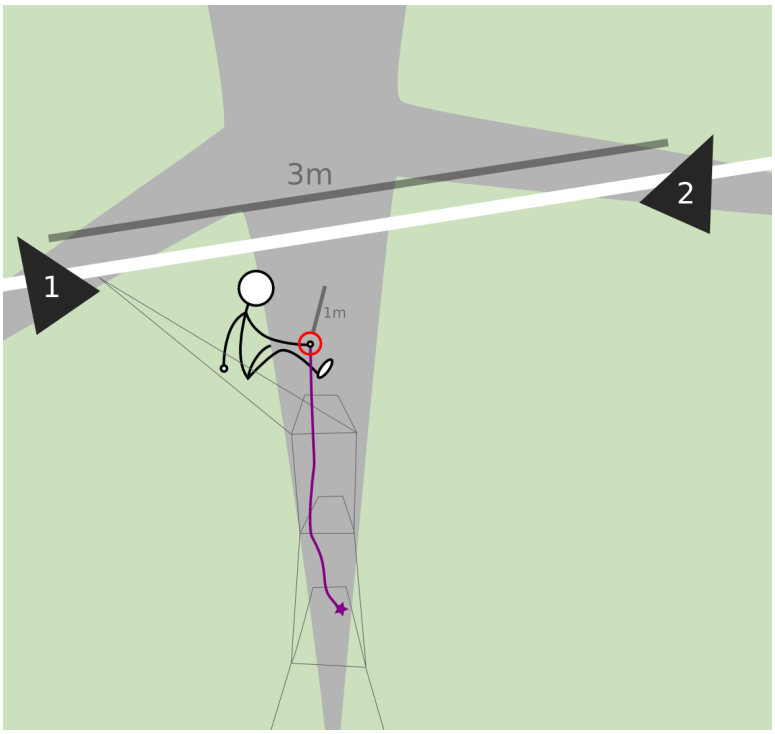

Figure 1.1: Experimental rig for BCI dataset. Ants were held in forceps and dropped at a distance of 1 m from the target tree trunk. The ant trajectory was filmed by two cameras (shown as dark triangles) attached to a PVC mount in the tree crown. Also shown are the tensioned lines that form the camera calibration frame.

canopy of the tropical rainforest. I then investigate how time to reach onset of equilibrium gliding, lift-to-drag ratio, and trajectory curvature vary as a function of the equilibrium glide velocity.

1.2 Methods

3-D trajectories were gathered for *C. atratus* ants on Barro Colorado Island (BCI), Panama, and at the Amazon Conservatory for Tropical Sciences (ACTS), near Iquitos, Peru (see Leigh (1999) and Madigosky and Vatnick (2000), respectively, for further information on these sites). In Section 1.2.1, I will describe the experimental rigs used to measure 3-D gliding ant trajectories, as well as the differences between the rigs used for the two sites.

1.2.1 Tree drop experiments

1.2.1.1 BCI dataset

The first set of tree drop experiments were conducted in an *Anacardium excelsum* tree (N09.160°, W79.841°) on Barro Colorado Island in Panama — see Figure 1.1. The chosen tree featured an exposed trunk section 21 m in height and ∼1 m in diameter beneath the first branches of the tree crown. Climbing ropes were installed in the tree using standard arborist methods (Jepson, 2000), and a length of PVC pipe was lashed across two branches in the crown (∼21 m above the forest floor) to serve as a camera mount. Two cameras (Casio EX-F1, Casio Computer Corporation) were attached to this PVC mount using Manfrotto Super Clamps and Model 3025 tripod heads (Manfrotto Supports, `http://www.manfrotto.com`). The cameras were set to a 20 fps burst mode, where over the course of 3 seconds each camera recorded 60 full-frame images (2816 × 2112 pixels, JPEG format).

Spatial calibration of the two cameras was performed using a 3-D calibration frame installed in the tree, consisting of two tensioned lines stretched from the tree canopy to the forest floor, with cross-tensioned lines maintaining a pyramid structure. Flagging tape markers were attached to this structure, and a tape measure was then used to make a series of point-to-point measurements between the markers. A custom Python script was used to estimate the 3-D locations of the markers relative to one another by least squares optimization.

The ants used in the experiment were collected from several native colonies on BCI, and were kept in plastic food containers with access to sugar water for <24 hrs prior to being used in experiments. Each worker was painted on its dorsal surface with a white paint marker (Mark-All brand) to improve their visibility against a dark forest background. For each trial, a single *C. atratus* worker was held in a haphazardly chosen orientation with 30 cm forceps and dropped from a position visible to both cameras, ∼1 m away from the tree trunk. The opening of the forceps as the ant was released was used as an optical cue for synchronizing the two video sources. No attempt was made to recapture ants that returned to the tree trunk, although experimental individuals were observed climbing back up into the canopy post-trial.

1.2.1.2 ACTS dataset

Experiments carried out at the Amazon Conservatory for the Tropical Sciences (ACTS; S03.251°, W72.908°) used a different camera arrangement, taking advantage of the extensive network of walkways and canopy platforms at this site — see Figure 1.2. A quasi-pyramidal calibration object formed from tensioned lines and markers was again used, installed in a target tree that was near to but not part of the walkway. Four cameras (Casio EX-F1) were mounted on the railings of the walkway platforms in two adjacent trees, set up with a clear view of the calibration frame. The cameras were separated by distances of up to 10 m in an effort to improve the accuracy of the triangulation process. In this experimental setup, a custom wireless triggering setup was developed using a series of Arduino microcontrollers

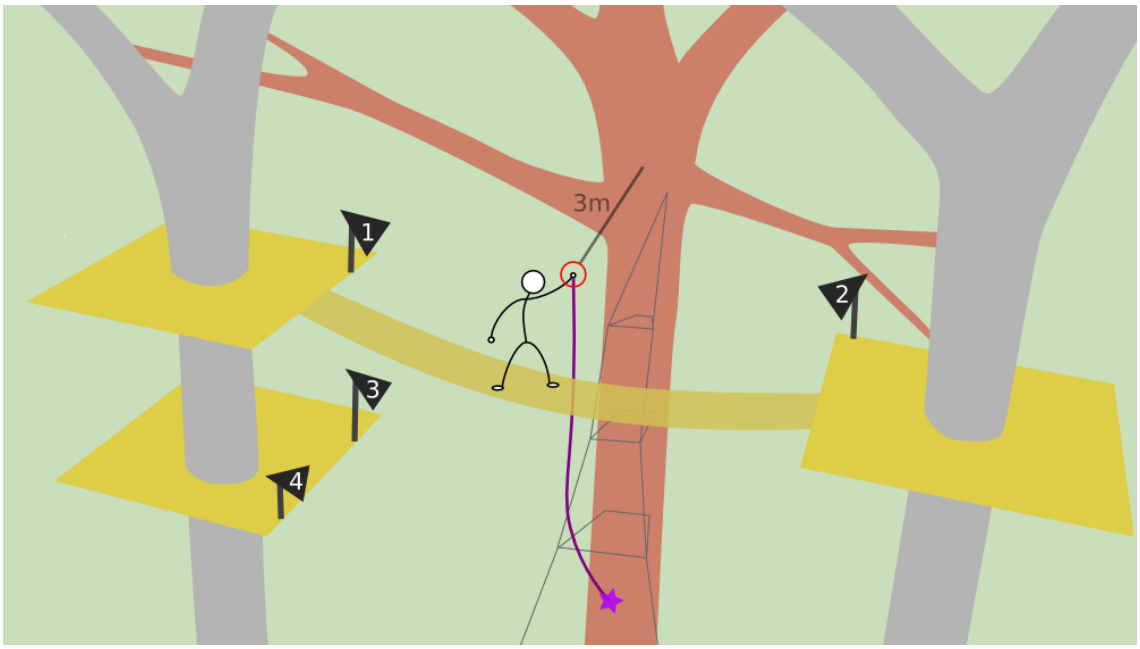

Figure 1.2: Experimental rig used to acquire ACTS dataset. Ants were dropped from a canopy walkway approximately 3 m from a target tree (shown in red), filmed simultaneously with synchronized cameras (represented by triangles) attached to platforms (shown in yellow) in neighboring trees.

(`www.arduino.cc`) and XBee radios (XBee Pro 802.15.4 extended range module, Digi International Inc., `www.digi.com`). A wireless transmitter held by the experimenter triggered the shutter release inputs of all four cameras simultaneously.

C. atratus ants were gathered from a nearby colony and used in experiments within 4 hours of collection. These subjects were painted as described in Section 1.2.1.1 to improve their visibility. Ants were dropped from the hanging walkway connecting the two camera trees, at a distance of approximately 3 m from the tree trunk and 22 m above the forest floor. Prior to their release, ants were held inside plastic vials dusted internally with fluorescent powder, as described by Yanoviak et al. (2010), to minimize handling.

1.2.2 Video analysis

Prior to tracking the motion of the ants in the videos, the complex rainforest background was subtracted using a frame-differencing method implemented in Python. By subtracting each video frame from the frame immediately preceding it, only the position of moving objects remained in the resulting processed video, as shown in Figure 1.3. The processed videos were imported into ImageJ (Version 1.44j, `http://rsbweb.nih.gov/ij/`), and then the position of the ant in every frame and view where it was visible was manually digitized using the MTrackJ plugin (`http://www.imagescience.org/meijering`).

Figure 1.3: **Left:** Crop from raw video frame, showing forest background. Highlighted with red circles are the markers that comprise the calibration frame. **Right:** Composite image of a trial, showing ant position in successive frames. Spline interpolation is shown in red.

To obtain 3-D trajectories from these digitized videos, it was necessary to develop a projection model for each camera describing the perspective transformation mapping 3-D points onto the 2-D image plane of the camera. Using the `calib3d` functionality provided by the OpenCV library (`http://opencv.willowgarage.com`), a pinhole camera model was estimated for each camera using the known 3-D locations of the calibration object markers and the pixel locations of these markers on the image plane — Hartley and Zisserman (2004) provides an introduction to the mathematical techniques used in this process.

Once the cameras had been calibrated, the pixel trajectories of the gliding ants digitized in the various camera views could then be used to determine the 3-D trajectories followed by the gliding ants in real world coordinates. For each point in time for which the position of the ant was visible in at least two camera frames, the 3-D location of the ant was estimated using a least-squares optimization process (using the `optimize.leastsq` routine from the SciPy library). The pinhole camera model for each of the cameras was used to calculate

the projected location of the estimated ant 3-D position on the image plane of the camera, and this projected location was compared to the digitized pixel location to calculate the projection error. The least-squares optimization process was used to estimate the location of the ant as the point in 3-D space that minimized the projected position error for all cameras.

These positional data were then smoothed and interpolated using three-dimensional cubic smoothing B-splines, via the SciPy `interpolate.splprep` function (smoothing parameter set to 0.01). The position of the spline was evaluated at all time-frames using the `interpolate.splev` function; values for the first and second derivatives of the position spline (i.e. velocity and acceleration) were also calculated using the same function.

1.2.3 Data analysis

1.2.3.1 Time taken to reach equilibrium

Trajectories from the BCI dataset were analysed to determine their equilibrium glide speed, the time taken for the ant to reach equilibrium, as well whether the ant landed successfully or not on the target tree. Each trajectory was classified as a "hit", "bounce" or "miss", according to whether or not the ant glided towards the tree and landed on the first attempt, glided towards the tree but failed to land successfully on the first attempt, or failed to impact on the tree, respectively.

The velocity of the ant estimated from the spline fit to the trajectory was used to determine the period of time elapsed between the release of the ant and when the ant reached its equilibrium glide speed. The beginning of the equilibrium glide phase was determined by the point in the time series where the vertical velocity of the ant settled to an approximately constant value (i.e. the equilibrium glide speed), identified by eye. A positive correlation between the time taken to reach equilibrium and the equilibrium glide speed would indicate that ants with a higher equilibrium glide speed take more time after beginning their descent to reach equilibrium.

1.2.3.2 Lift-to-drag ratios

By comparing the magnitude of the horizontal component of the glide velocity to the magnitude of its vertical component, it was possible to determine a lift-to-drag ratio for gliding ants in their equilibrium glide phase. In this analysis, trajectories were only used if they featured an equilibrium glide section of at least 0.5 s duration, ensuring that there were at least 10 time points (given the filming rate of 20 fps) where a lift-to-drag ratio could be estimated for each trajectory. Trajectories from both the BCI and the ACTS datasets were used, and the mean lift-to-drag ratio observed in each equilibrium glide section was compared to the mean equilibrium glide speed. A linear regression analysis was performed on these data to determine whether a relation existed between equilibrium glide speed and lift-to-drag ratio.

1.2.3.3 Equilibrium trajectory curvature

To investigate whether trajectories with lower equilibrium glide speeds exhibited tighter trajectory curvature, which would indicate the potential for greater maneuverability, the curvature of the equilibrium glide sections was determined using the standard formula for 3-D curvature:

$$\kappa(t) = \frac{|\dot{\mathbf{r}}(t) \times \ddot{\mathbf{r}}(t)|}{|\dot{\mathbf{r}}(t)|^3} \tag{1.1}$$

where $\kappa(t) = 1/R(t)$ (where $R(t)$ is the radius of curvature of the trajectory at time t), and $\dot{\mathbf{r}}(t)$ and $\ddot{\mathbf{r}}(t)$ are the velocity and acceleration of the ant at time t (estimated from the spline fit to the ant trajectory). For each trajectory, the average curvature of the steady state section was compared with the equilibrium glide speed to determine whether lower glide speeds were correlated with greater maneuverability. Trajectories from both datasets were only used if their equilibrium glide section lasted longer than 0.5 s.

1.3 Results

1.3.1 BCI trajectories

A total of 44 usable trajectories were obtained from the tree drop experiments performed on Barro Colorado Island (described in Section 1.2.1.1); trajectories were discarded if the ant was visible in both cameras in fewer than 20 frames (1 s of real time) out of the total 60 frames for each trial. A subset of these trajectories are plotted in Figure 1.4, where the trajectories shown are the usable trajectories obtained over the course of one day of experiments. All of the trajectories exhibit a J-curve shape, in which a period of near-vertical descent is followed by a shallowing of glide angle and eventual landing; many of the trajectories, including some of those shown in Figure 1.4, curve away from the tree trunk before returning to land.

All trajectories, regardless of whether or not the ant successfully targeted and landed upon the tree trunk, exhibited some degree of horizontal motion and curvature. Of the trajectories scored as "misses", none could be classified as pure vertical descents; in these cases, the ants often appeared to be targeting nearby secondary vegetation (the sole "miss" trajectory shown in Figure 1.4 is a good example).

Furthermore, as can be seen in Figure 1.4, many of the ants did not successfully land on the tree trunk at first impact; these ants bounced off the trunk, re-stabilized, and returned to the tree trunk for a second landing attempt. In Figure 1.4, it appears that only those ants which land higher up on the tree trunk bounce upon impact; this probably does not indicate that ants landing lower on the tree trunk did not bounce, but rather that by the time these ants reached their landing spot they were no longer distinguishable from the background in the video.

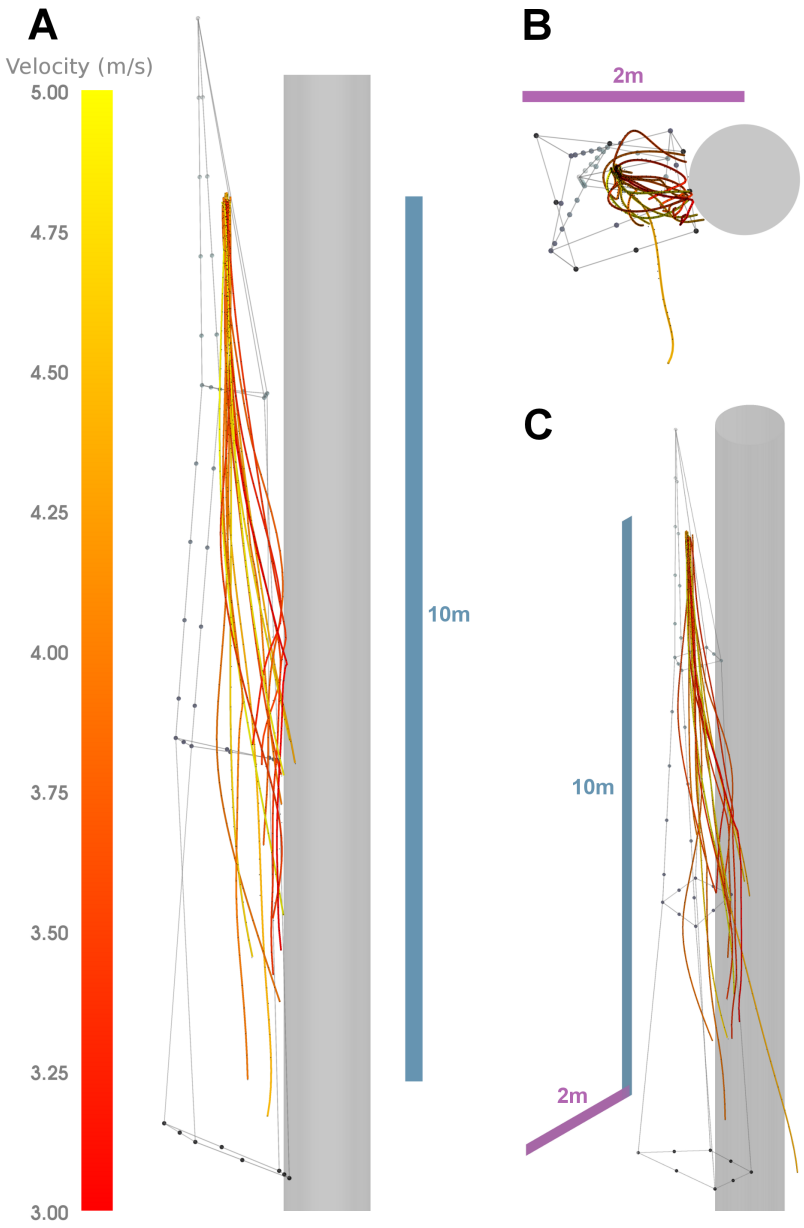

Figure 1.4: 3-D trajectories of gliding *C. atratus* ants from the BCI dataset. Ants were released at a distance of 1 m from the target tree trunk (represented as a grey 1 m diameter cylinder in these plots). The pyramidal calibration object used to calibrate the camera views is also shown, with the markers used for calibration represented as spheres. Trajectories are colored according to the average glide speed in the equilibrium phase. **A:** Side view, with 10m scale bar. **B:** Top view, with 2m scale bar. **C:** Isometric view, with scale bars from top and side views shown.

1.3.2 ACTS trajectories

A total of 12 usable trajectories were obtained for the ACTS rig, in which the ants were dropped at a distance of ∼3 m from the target tree. 15 ants were dropped in total; of these, only one did not successfully target and impact with the tree trunk. In these trajectories, shown in Figure 1.5, the release and initial section of the glide was not within the field of view of the cameras; the goal in this set of experiments was to determine whether the trajectories of ants dropped further from their target were shallower and more direct than the trajectories of ants dropped closer to the target tree (1 m for the BCI dataset, Section 1.3.1).

In this experiment, the mottled texture of the target tree trunk made it virtually impossible to distinguish the ant from the background when the projected location of the ant was in front of the tree trunk in a camera view, with the effect that the impacts of the ants with the tree trunk, and the outcome of that impact (hit or bounce), could not be observed.

1.3.3 Cylindrical trajectories

In Figure 1.6, equilibrium glide sections of all trajectories from the BCI dataset are shown transformed into cylindrical coordinates: the vertical z-axis remains unchanged, and the x and y axes are combined into a radial coordinate, r, describing the distance of the ant from the surface of the tree trunk. The trajectories are colored according to the equilibrium glide speed. This mapping of the 3-D trajectories onto a 2-D plane removes information regarding turning maneuvers within the horizontal plane, but enables easy comparison of the trajectory glide angles.

1.3.4 Time to onset of equilibrium

In Figure 1.7, we see that there is a significant positive correlation between the terminal velocity of an individual ant and the elapsed time between release of the ant and onset of the terminal velocity phase. Each trajectory is represented by a single point color-coded according the outcome of the trial, where a hit represents a successful landing without a bounce, a bounce represents a landing on the target following an initial impact, and a miss represents a failure to reach the tree trunk. The mean equilibrium glide speeds for the hit and bounce groups were indistinguishable ($\mu_{\text{hit}} = 4.03\,\text{m/s}$, $\mu_{\text{bounce}} = 3.85\,\text{m/s}$), but the miss group mean equilibrium glide speed ($\mu_{\text{miss}} = 4.53\,\text{m/s}$) was significantly higher ($p < 0.05$; ANOVA/Tukey honest significant differences test performed in R).

1.3.5 Lift-to-drag ratios

Figure 1.8 shows trajectories from the BCI and ACTS datasets (where the primary difference between these experiments was the horizontal distance between the point of release of the subject ant and the target tree; 1 m and 3 m, respectively), where trajectories are represented by their mean equilibrium glide speed and the mean lift-to-drag ratio exhibited by the subject

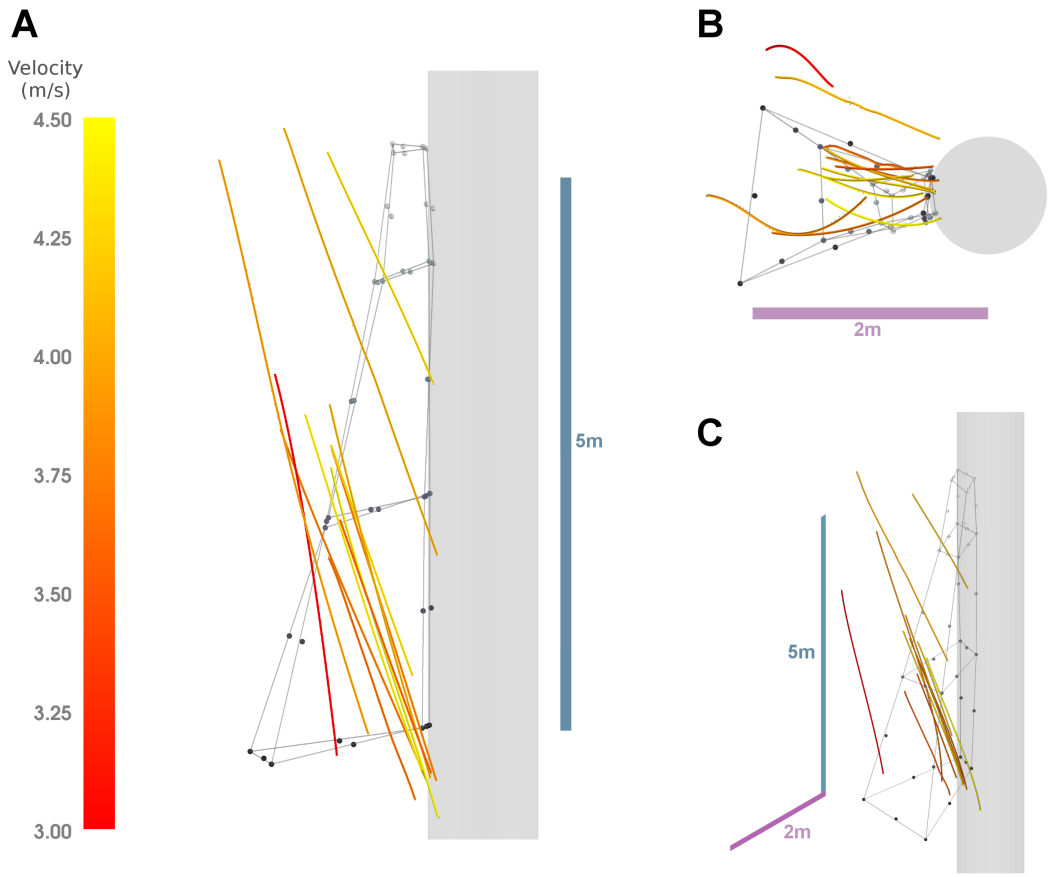

Figure 1.5: 3-D trajectories of gliding *C. atratus* ants from the ACTS dataset. Ants were released 3 m away from the target tree trunk (shown as a grey cylinder of 1 m diameter). The point of release of the ants was not within the field of view of the cameras, and these trajectories all represent ants gliding at equilibrium. The tensioned frame of markers used to calibrate the cameras is also shown, with the markers represented as spheres. Trajectories are colored according to the average glide speed. **A:** Side view, with 5m scale bar. **B:** Top view, with 2m scale bar. **C:** Isometric view, with scale bars from top and side views shown.

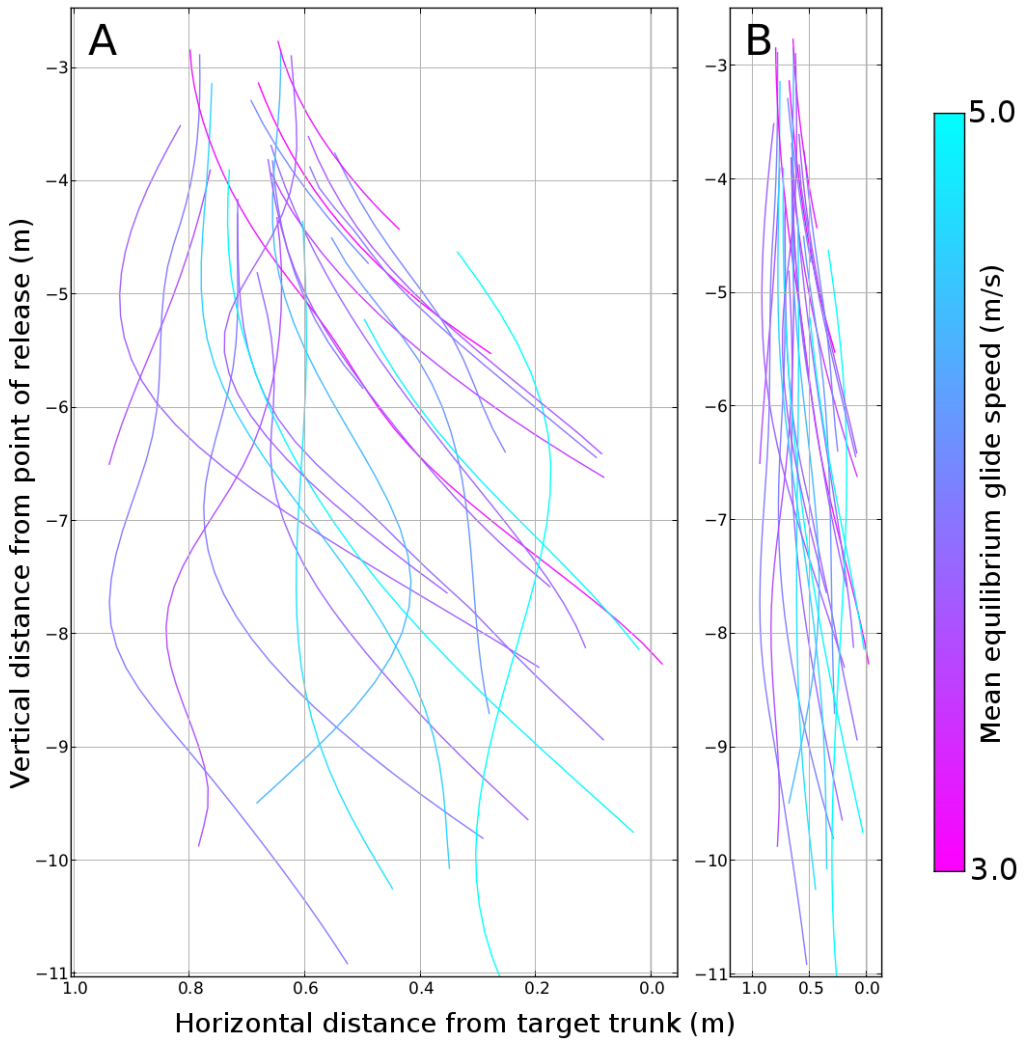

Figure 1.6: Trajectories for ants released 1 m from the target tree, converted to cylindrical coordinate system and color-coded by equilibrium glide speed. **A:** Trajectories with uneven scaling of horizontal and vertical dimensions to highlight differences in glide angles. **B:** Same trajectories, with equal scaling of horizontal and vertical dimensions.

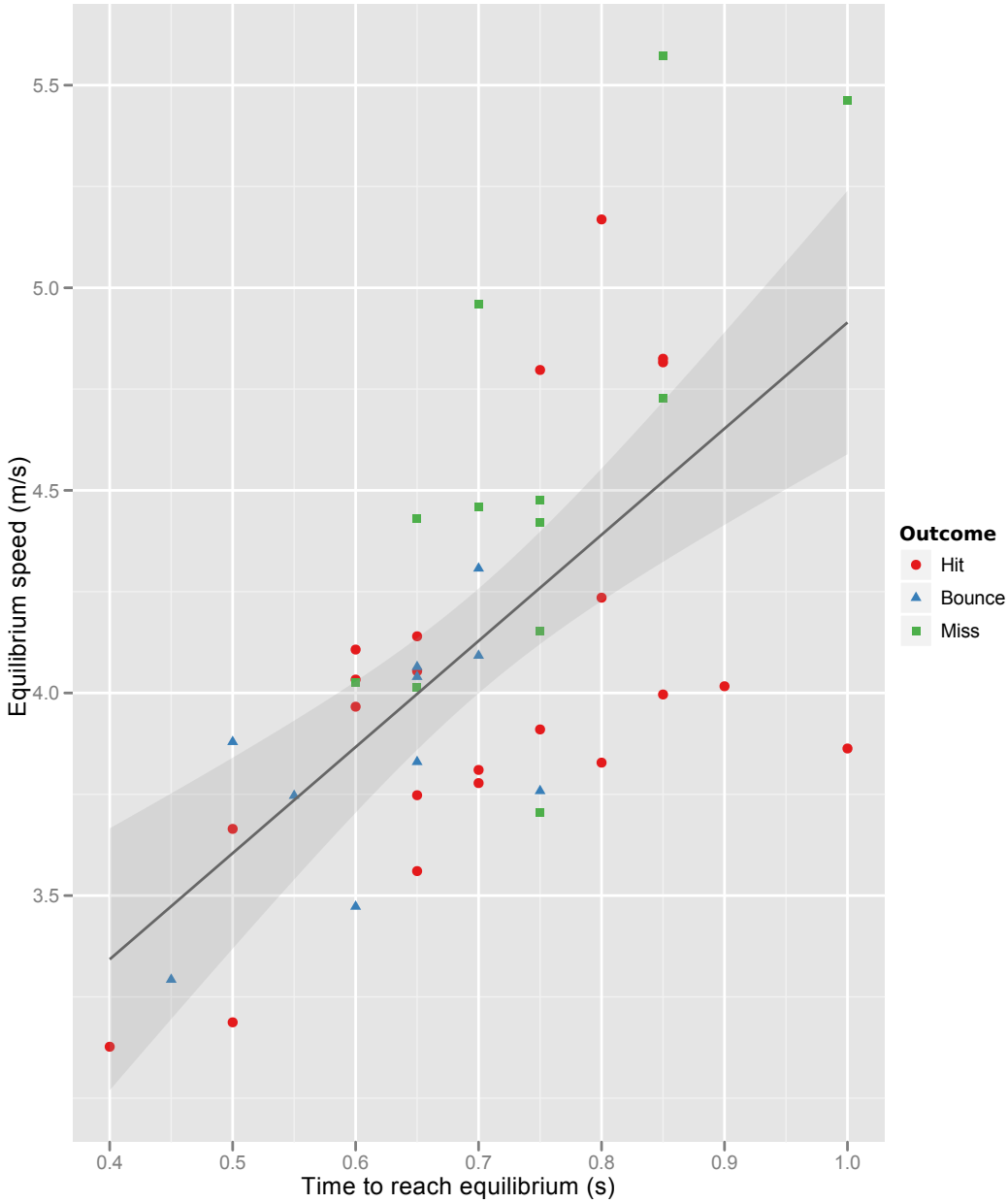

Figure 1.7: 44 trajectories from the BCI dataset, represented as the equilibrium glide speed attained plotted against the time elapsed between release and reaching equilibrium. A linear fit to the data reveals a significant positive correlation ($y = (2.6 \pm 0.5)x + (2.3 \pm 0.3)$, $R^2 = 0.40$, statistics calculated in R).

in the equilibrium glide section. As described in Section 1.2.3, the trajectories used in this analysis were those which featured an equilibrium glide section with a duration of at least 0.5 s. All of the ACTS trajectories met this criterion, compared with only 22 of the 44 BCI trajectories. This filtering process was necessary to ensure that the equilibrium glide sections being analysed had at least 10 time points where the lift-to-drag ratio could be estimated, ensuring that a trustworthy statistical mean could be calculated, but has the effect that only those trajectories from the BCI dataset where the ant took at least 0.5 s to reach its target are included.

Within datasets, ants dropped 3 m from the target tree (ACTS dataset) exhibited significantly higher lift-to-drag ratios than ants dropped 1 m from the target tree (BCI dataset). Neither dataset had a significant correlation between equilibrium glide speed and mean lift-to-drag ratio, with the caveat that the filtering process applied to the BCI dataset removed trajectories where the trunk was reached in less than 0.5 s, effectively removing high performance trajectories.

1.3.6 Curvature and maneuverability

As described in Section 1.2.3, mean trajectory curvature was estimated for the equilibrium glide sections of those trajectories with an equilibrium glide section lasting at least 0.5 s. This filtering process removed 22 of the 44 BCI trajectories in which the ant reached the target tree trunk in under 0.5 s after reaching aerodynamic equilibrium. The results of this curvature analysis are shown in Figure 1.9.

For the ACTS dataset, curvature was not significantly correlated with equilibrium glide speed. For the BCI dataset, a significant correlation was found, but largely on account of the influence of three trajectories exhibiting high curvature ($\kappa > 0.2\,\mathrm{m}^{-1}$) and low equilibrium glide speed ($v < 3.5\,\mathrm{m/s}$). Upon inspection of the 3-D shapes of these trajectories, these were found to be "bounce" trajectories, where the ant did not land successfully on the first attempt and entered a second equilibrium glide phase before returning to land on the tree trunk. If these three bounces are treated as outliers, the correlation between mean equilibrium curvature and glide speed for the BCI dataset is no longer significant. However, even with these outliers removed, mean curvature was found to be significantly higher in the BCI dataset than in the ACTS dataset — see caption of Figure 1.9 for statistical details.

1.4 Discussion

The three-dimensional trajectories in this study are the first ever reported for a gliding animal in natural conditions. The subjects of this study were dropped within a natural forest environment with trees used for visual cues; aside from the unavoidable handling of the animals prior to their being dropped and the presence of a visually unobtrusive calibration frame installed on the target tree, every effort was made to elicit natural behavior. The

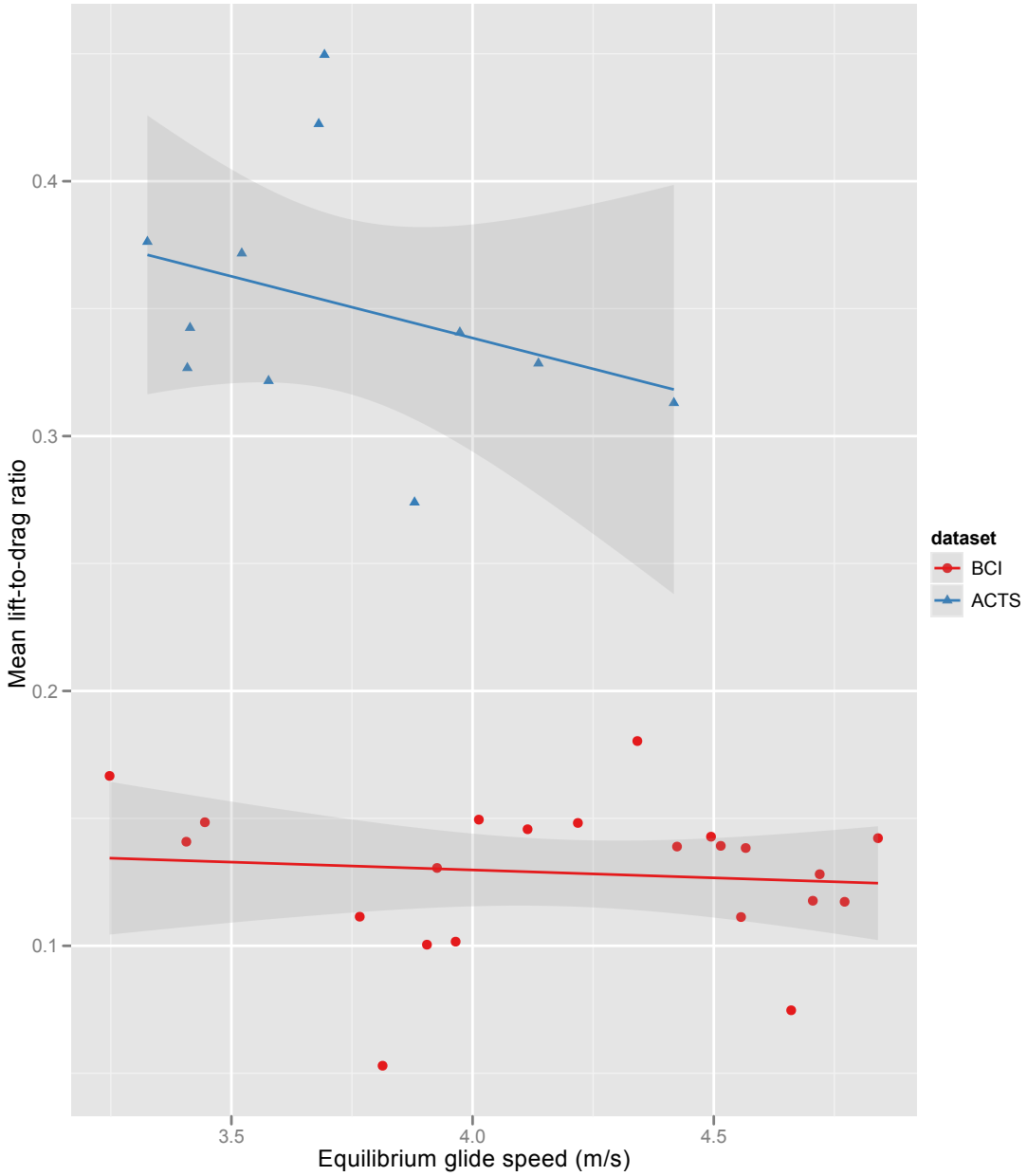

Figure 1.8: Trials from BCI and ACTS datasets, using only trajectories with an equilibrium glide section of minimum 0.5 s duration. Differences in mean lift-to-drag ratio between groups was highly significant ($\mu_{\text{BCI}} = 0.13, \mu_{\text{ACTS}} = 0.35, t = -13.6$, Welch Two Sample t-test performed in R). Within-group variation in lift-to-drag ratio was not significantly correlated with equilibrium glide velocity for either dataset (slope coefficient confidence $p > 0.05$, linear regression analysis performed in R).

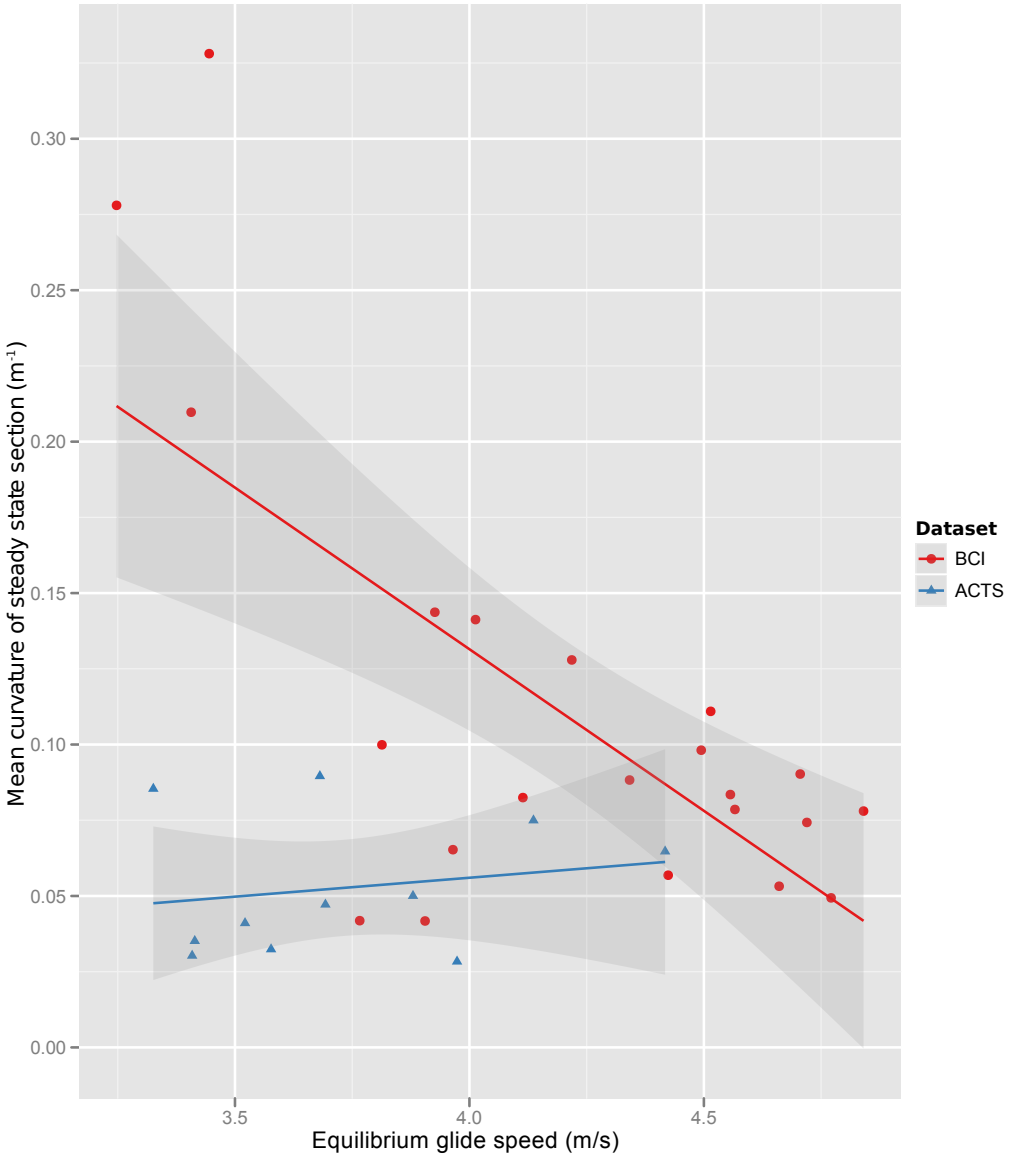

Figure 1.9: Mean trajectory curvature plotted as a function of equilibrium glide speed for BCI and ACTS datasets, using only trajectories with an equilibrium glide section of minimum 0.5 s duration. Correlation between equilibrium speed and curvature is not significant for ACTS dataset. For BCI dataset, correlation is significant due to effect of 3 data points with low equilibrium speed and high curvature; if these points are treated as outliers, correlation between equilibrium speed and curvature is no longer significant. Even with these outlier points removed, mean curvature was higher for BCI dataset than ACTS dataset ($\mu_{\text{BCI}} = 0.085, \mu_{\text{ACTS}} = 0.053, t = -3.29, p < 0.05$, Welch two sample t-test performed in R).

animals were not trained in any way, were used in experiments within 24 hours of collection, and each subject was not used more than once.

As documented by Yanoviak et al. (2005), *C. atratus* ants exhibit an inverse correlation between body size and glide index, defined as the ratio of the horizontal to vertical distance between the point of release and the landing point. Yanoviak et al. (2005) speculated that the primary contributor to this variation in glide index was the additional time required for large ants to reach their minimum viable glide velocity ($U_{\min}$, as described by Kingsolver and Koehl (1994)). In this study, analysis of the 3-D trajectories followed by gliding *C. atratus* ants showed a significant correlation between equilibrium glide speed and the time taken to reach equilibrium (Figure 1.7). In the trials recorded for the BCI dataset, ants with high equilibrium glide speeds took up to 0.5 s longer to reach equilibrium than ants with lower equilibrium glide speeds — which, for terminal velocities in the range of 4 m/s, could lead to an increase in the vertical distance required to return to a target tree trunk by up to 2 meters.

In the introduction to this study, an additional hypothesis explaining the variation in glide index with size was introduced, postulating that smaller ants may exhibit a higher lift-to-drag ratio than larger ants. For the trajectories used in this analysis, lift-to-drag ratios were significantly higher for ants dropped 3 m away from the tree trunk (ACTS dataset) than ants dropped 1 m from the tree trunk (BCI dataset); these results are shown in Figure 1.8. Within the two datasets, no significant correlation between equilibrium glide speed and lift-to-drag ratio was discovered. The most plausible explanation for the difference in lift-to-drag ratios observed in these two datasets is that ants have some degree of control over their lift-to-drag ratio, and use this control to influence the shape of the J-shaped curve they follow as they travel towards their target. It is also important to note that half of the trajectories from the BCI dataset were not used in this analysis on account of the duration of their equilibrium glide section being too short to measure a mean lift-to-drag ratio. These trajectories included the ants which targeted and landed upon the tree trunk within 0.5 s after reaching equilibrium, and may have exhibited a higher equilibrium lift-to-drag ratio.

Trajectory curvature, defined as the inverse of the local radius of curvature along the trajectory, was not significantly correlated with equilibrium glide speed for either dataset, as shown in Figure 1.9. Mean curvature of the equilibrium glide sections was lower in the ACTS dataset than the BCI dataset, indicating that ants dropped 3 m away from a target tree trunk follow a more direct path to the trunk than those dropped 1 m away. As gliding behavior in *C. atratus* is visually mediated (Yanoviak and Dudley, 2006), this reduction in curvature for trajectories approaching a more distant target is possibly due to the smaller visual angle subtended by a more distant target.

These results support the suggestion by Yanoviak et al. (2005) that the decrease in glide index with increasing body size is due to the additional time and vertical distance required for a larger ant to reach its equilibrium glide speed. Trajectory curvature and lift-to-drag ratios were variable across individuals but were not significantly correlated with equilibrium glide speed.

It appears likely, given the variation in curvature and lift-to-drag ratios both within

and between trajectories, that *C. atratus* ants have some degree of behavioral control over both of these variables. However, it is not possible, given the resolution of the video data gathered in this study, to determine what postural behaviors are being used by the ants in effecting aerodynamic control. A logical next step, and the focus of Chapter 2, is to obtain high-resolution postural data linking changes in posture with aerial maneuvers affecting trajectory curvature and lift-to-drag ratio.

Chapter 2

Postural kinematics of skydiving ants

2.1 Introduction

The trajectories presented in Chapter 1 show that *Cephalotes atratus* ants are capable of effecting sophisticated aerodynamic control, allowing them to glide towards and land upon a target tree trunk after falling from the canopy of the tropical rainforest.

While videos of gliding *C. atratus* ants gathered for previously published studies (Yanoviak et al., 2005, 2010) have sufficient resolution to determine that the ants glide backwards (that is, with the gaster leading) and that the hind-legs are held outstretched, it has remained unclear as to how these ants use postural control to influence the aerodynamic forces acting upon them during aerial descent and thereby control their trajectories to perform targeted gliding. Ablation studies have confirmed the importance of legs in ensuring landing success in *C. atratus* ants gliding to a tree: Yanoviak et al. (2010) showed that targeting success and glide index (defined as the ratio of the total horizontal distance to the total vertical distance travelled by the ant between its point of release and its landing point) both decline significantly for ants with hind-legs removed. Ablation of the gaster did not have a significant effect on the success rate of ants returning to the target tree, but did significantly decrease the glide index. Yanoviak et al. (2010) also provided preliminary evidence that asymmetries in hindleg angle in the coronal plane are associated with turns in yaw.

Use of the abdomen and legs in aerial control has been previously documented across diverse groups of flying insect taxa (e.g. locusts (Arbas, 1986; Camhi, 1970) and flies (Zanker, 1988); see reviews by Dudley (2000) and Taylor (2001). Outside of Orthoptera and Diptera, Combes and Dudley (2009) reported that male orchid bees extend their hind-legs during flight to increase their stability while flying in turbulent air, and Hinterwirth and Daniel (2010) showed that hawkmoths modulate abdominal flexion angle in response to oscillatory visual stimuli. However, in these cases, the abdomen and legs are presumed to act as a set of control surfaces supplemental to the aerodynamic effects of the flapping wings. In the case of gliding *C. atratus* ants, the lack of wings suggests that the abdomen and legs assume the role of primary control surfaces.

In the current study, postures utilised by gliding *C. atratus* ants are measured using a vertical wind tunnel and multiple synchronized cameras. From the data presented in Chapter 1, it is expected that *C. atratus* ants are able to achieve aerodynamic stability as well as some degree of control over the direction of the net aerodynamic force vector acting upon them, allowing them to perform pitching and turning maneuvers. Regarding aerodynamic stability, while active control of orientation in passively unstable aircraft is possible (e.g. in highly maneuverable military airplanes), it seems more likely that *C. atratus* ants adopt a gliding posture that is passively stable. Passive aerodynamic stability requires a vertical separation of the centers of gravity and aerodynamic pressure, with the center of aerodynamic pressure above the center of gravity — examples include dandelion seeds, ballooning spiders, and human parachutists. In *C. atratus*, it is reasonable to hypothesize that this vertical separation of the centers of gravity and aerodynamic pressure is achieved by elevation of some or all of the legs, as such a configuration elevates the center of aerodynamic pressure while changing the vertical location of the center of mass to a lesser extent.

With regard to control of the direction of the net aerodynamic force acting on the ant, the ablation studies reported by Yanoviak et al. (2010) strongly suggest that the legs are implicated in control of maneuvers. Based on expectations from elementary aerodynamic theory, it is expected that control of body pitch angle is achieved by symmetric fore-aft motions of the legs, which are expected to move the center of aerodynamic pressure along the anteroposterial axis and thereby cause the ant to pitch up and down. Turns, conversely, are expected to be associated with left-right postural asymmetries. The kinematic analysis presented by Yanoviak et al. (2010) indicates that asymmetric fore-aft postures of the hind-legs are associated with turns, but the other legs may play a role; it is also possible that asymmetric changes in dorsoventral leg elevation may have an effect on the sideways component of the aerodynamic force experienced by a gliding *C. atratus* ant.

Control of pitch angle, furthermore, is expected to be associated with changes in the relative magnitude of the fore-aft horizontal component of the aerodynamic force acting on a gliding *C. atratus* ant. Assuming that the axial body parts of the ant (head, trunk and gaster) behave approximately like a cylinder, changes in the pitch angle of the ant body are expected to cause changes in the lift acting on the body (Ellington, 1991; Flower, 1964). In the current study, it is hypothesized that the pitch orientation of a gliding *C. atratus* ant is correlated with the relative magnitude of the horizontal component of the aerodynamic force acting upon it.

2.2 Methods

2.2.1 Trial subjects

Vertical wind tunnel experiments were conducted at the Amazon Conservatory for Tropical Sciences (ACTS), north of Iquitos, Peru — details of the site are reported by Madigosky and Vatnick (2000). *Cephalotes atratus* workers were collected from a local colony tree

(S 03°15.121', W 072°54.370') and were held in plastic food containers for less than 4 hours prior to being used in experiments. The mass of each trial subject was measured using a battery powered 0.1 mg resolution scale (Tanita 1210N).

2.2.2 Wind tunnel design

Close up video of gliding ants was obtained using a custom-built vertical wind tunnel, shown in Figures 2.1 and 2.2. This wind tunnel was designed as an open-circuit blower-type tunnel, meaning that air is blown (rather than sucked) into the working section, and the air is not recirculated. The main components used in the design were inspired by the design guidelines provided by Mehta and Bradshaw (1979) and Barlow et al. (1999), although some significant changes were made in the interests of portability and light weight.

2.2.2.1 Fan and power control

The working section of the wind tunnel was 14 cm ×14 cm in cross-section (area = 0.0196 m^2). To provide a vertical wind speed in the working section approximately equal to the terminal velocity of a falling *C. atratus* ant (∼ 4 m/s, see Chapter 1), the fan driving air into the wind tunnel had to provide a flow rate of ∼0.08 m^3/s.

Blower-type wind tunnel designs typically use centrifugal fans rather than axial fans (Mehta and Bradshaw, 1979), as the blade of a centrifugal blower operates at the same lift coefficient along its entire span (the blades of axial fans operate at non-constant lift-coefficient as the distal tip of the blade moves at a higher speed than the parts of the blade closer to the center). This helps centrifugal blowers produce a more uniform flow profile cross-section; a disadvantage of this fan type, however, is their lower power efficiency. High flow-rate centrifugal fans typically require a mains voltage supply and draw substantial current; the Papst D2E146 fan (`http://www.ebmpapst.us`), for example, provides a volume flow rate of ∼0.1 m^3/s and draws 160 W of power. Using such a fan would have required the use of an external generator to provide power to the drive section of the wind tunnel and, as portability and light weight were two of the most important design goals for this wind tunnel, this was deemed to add unacceptable weight to the tunnel. The wind tunnel was therefore designed around an axial fan (Comair-Rotron Caravel, 0.27 m^3/s max, `http://www.comairrotron.com`) to drive air into the apparatus — the fan required a 24 V DC power supply and drew a maximum of 1.5 A, allowing it to be easily powered by a lightweight nickel metal-hydride (NiMH) 24V battery pack.

The fan speed was controlled using an Arduino (`http://www.arduino.cc`) controller to provide a pulse-width modulated voltage to the base pin of a TIP-120 Darlington transistor, with the battery connected to the collector pin via the fan and the emitter pin connected to ground. The PWM signal rapidly switched the fan on and off, with the duty cycle of the signal controlling the fan speed. The duty cycle of the Arduino PWM pin was controlled using a potentiometer connected to one of the Arduino analog inputs, and an LCD screen

Figure 2.1: Photograph of portable wind tunnel used in this study, with 188 cm tall human provided for scale. Photo credit: Steve Yanoviak

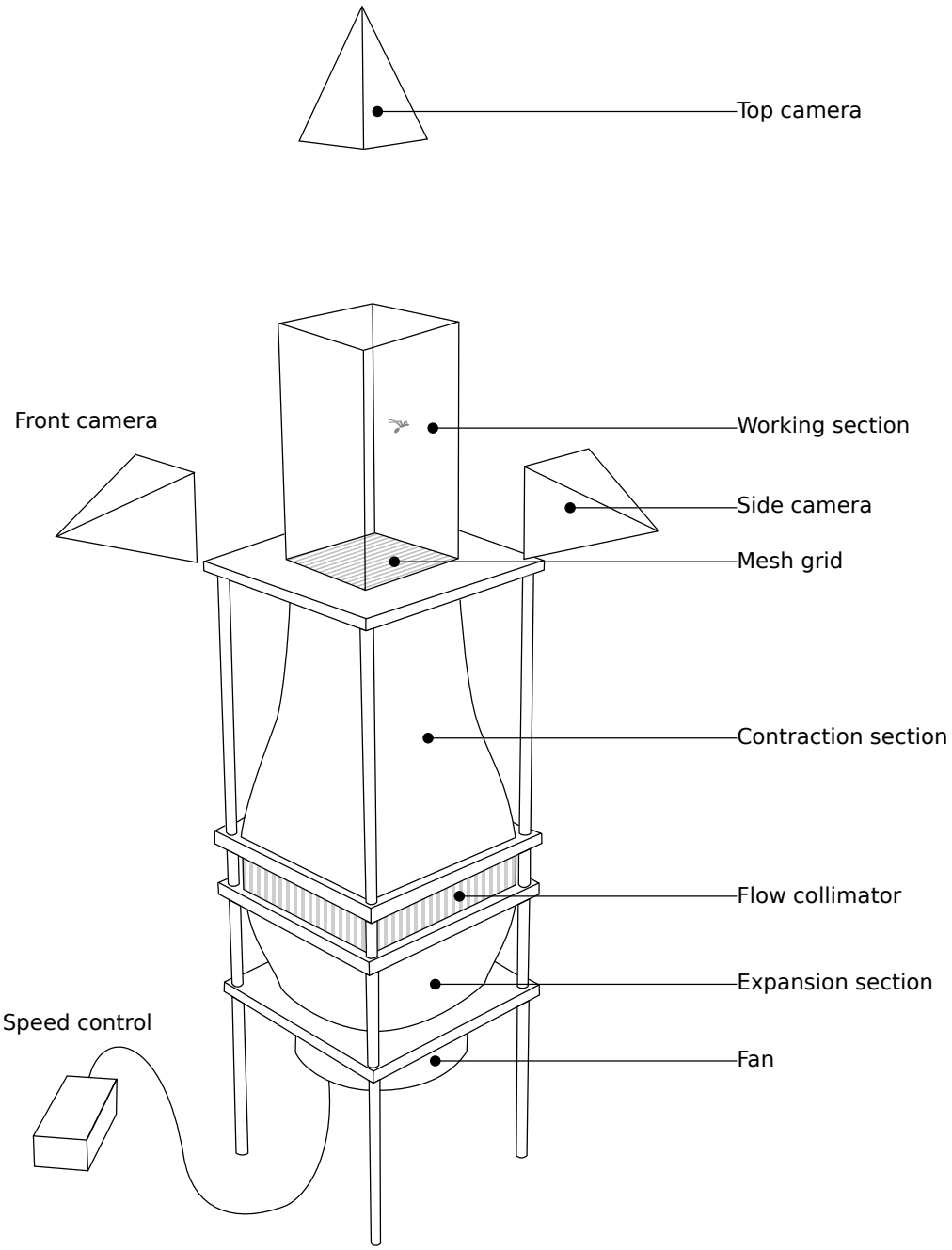

Figure 2.2: Diagram of wind tunnel components referred to in the text.

connected to the Arduino digital outputs was used to provide visual feedback of the duty cycle.

2.2.2.2 Flow shaping

To ensure a steady, even flow within the working section, the air travelling through the wind tunnel passed through a series of stages designed to mix the air, remove the swirl generated by the axial fan, and reduce turbulence.

The fan first forced air upwards into an expansion cone sewn from windproof nylon fabric and held tautly in shape with webbing straps (visible in Figure 2.1). This expansion cone increased the cross-sectional area of the wind tunnel from $0.051\,\mathrm{m}^2$ to $0.079\,\mathrm{m}^2$, with the goal of lowering the air speed within the tunnel prior to the honeycomb stage and thereby reducing the pressure loss within the tunnel due to the impedance of the honeycomb (Mehta and Bradshaw, 1979).

The honeycomb stage was formed by a 4 cm thick sheet of aluminum honeycomb with a cell cross-sectional area of $\sim 35\,\mathrm{mm}^2$. This stage functioned as a flow collimator, removing swirl in the flow introduced by the axial fan and reducing turbulent eddies larger than the cell size.

Air leaving the honeycomb section subsequently entered a contraction section, reducing the cross sectional area of the tunnel from 24×24 cm to 14×14 cm over the course of 40 cm in the vertical direction. As for the expansion cone, this contraction section was sewn from windproof nylon tent fabric and held tautly in shape with webbing straps. The goal of this stage of the wind tunnel was to increase the mean flow speed of the wind tunnel before reaching the working section, as well as reduce the relative magnitude of the variations in flow velocity (Mehta and Bradshaw, 1979).

Prior to entering the working section of the wind tunnel, the air was forced through a grid formed from nylon mesh (square holes, 2×2 mm). This mesh improved the uniformity of the flow by introducing a significant static pressure drop (reducing variation in longitudinal mean velocity) and reducing turbulence intensity (Mehta and Bradshaw, 1979), and also prevented objects dropped into the working section from falling into the preceding stages of the tunnel. This screen was the major impedance against which the driving fan had to work: without the screen in place the maximum air speed in the working section was $> 8\,\mathrm{m/s}$, compared to 4.5 m/s with the screen in place (flow speeds measured with a TSI Velocicalc hot-wire anemometer).

2.2.2.3 Tunnel structure and working section

The frame of the wind tunnel was formed from 4 aluminum tubes with feet at one end for the wind tunnel to stand on. Four 1 cm thick acrylic mounting plates were used to mount the various stages of the wind tunnel, which were designed in Solidworks 3D (Solidworks Corp., Massachusetts, USA) and cut on a laser cutter; these plates were used as interfaces between the fan, expansion, honeycomb, contraction and working sections, as shown in Figure 2.2. All

joining interfaces were covered internally with windproof Dacron sail repair tape to prevent air leaks.

Plate 1 joined the fan and the expansion cone, and had a circular cutout with mounting holes for connecting the axial driver fan as well as larger holes for connecting the webbing straps of the expansion cone. Plates 2 and 3 joined the expansion cone, honeycomb section, and contraction section with a 0.24×0.24 m square cutout for the honeycomb and mounting holes for the webbing staps of the fabric expansion and contraction sections. Plate 4 joined the contraction section with working section, with a 0.15×0.15 m cutout for the working section plates, cutouts for attaching the webbing straps of the contraction section, and reinforced sections with mounting holes for the camera rails (discussed in Section 2.2.2.4.

The working section was formed from 4 acrylic plates ($30 \times 15 \times 0.5$ cm), sealed at the edges with clear cellophane tape and bound together at the top with electrical tape. The interior surfaces of the plates were marked with small crosses in permanent marker at 3 cm intervals, for a total of 160 camera calibration markers.

2.2.2.4 Cameras

Three cameras (Casio Exilim EX-F1, `http://www.casio.com`) were attached to the top plate (Plate 4) of the wind tunnel structure, providing nominally orthogonal top, front and side views of the working section. The front and side cameras were mounted on 4 cm square aluminum tube sections with Manfrotto Super Clamps and Model 3025 tripod heads (`http://www.manfrotto.com`), and the top camera, looking down into the working section, was mounted on a Manfrotto Magic Arm. The cameras were set to record a 1 s burst of images at a filming speed of 60 fps (2816×2112 pixel resolution, JPEG format), and were synchronized by connecting a single button switch trigger to the remote trigger inputs of all three cameras.

Due to the proximity of the cameras to the working section, small aperture values were required to ensure that camera focus was maintained over the full depth of the working section, and exposure times were set to a minimum of 1.25 ms to avoid motion blur. These requirements necessitated working outdoors in direct sunlight, as depicted in Figure 2.1.

2.2.3 Trial protocol

For each trial, an ant was placed into an opaque plastic tube internally coated with fluorescent powder to prevent the tarsi from being able to stick to the surface. A few initial trials were conducted to determine an appropriate speed for the wind tunnel for the subject, ideally finding a speed slightly less than the terminal velocity of the subject. The ant was then dropped into the wind tunnel repeatedly until five suitable bouts of stable gliding were obtained, where suitability of a given bout was defined as being at least 0.3 s in duration, including a full extension of the legs, and localized within the center of the working section at least 1 cm away from the walls.

2.2.4 Video Analysis

2.2.4.1 Video pre-processing

For each trial, the location of the trunk of the ant was digitized in each camera view using ImageJ (version 1.44, `http://rsbweb.nih.gov/ij/`) and the MtrackJ manual tracking plugin (`http://www.imagescience.org/meijering/`). These pixel locations were used to crop a 400×400 pixel window out of the source image, and the three camera views were then assembled into a single 800×800 pixel image containing the top, front and side view of the ant over the course of a glide trial. Subsets of these three-view videos were then selected for posture analysis, where the main criteria for selecting a suitable subset of frames were distance of the ant from the walls of the working section of the wind tunnel and visibility of all features.

2.2.4.2 Digitization procedure

For each view and frame of a given subsequence, 19 morphological landmarks were manually digitized (see Fig 2.3). A sequence of 20 frames thus required the digitization of a maximum of 1140 landmarks (19 features × 3 views × 20 frames). However, occlusion of landmarks by other body parts was common; if features were not visible in a given camera view, no point was digitized.

2.2.4.3 Camera calibration

The three camera views were calibrated using the Python bindings to the OpenCV library (Version 2.3, `http://www.willowgarage.com/opencv`), as described in Chapter 1. Briefly, a pinhole camera model was built for each camera using the pixel locations of the markings on the working section walls as projected onto the image plane of the camera. This model described the projection of points in 3D space onto the 2D pixel space of the image produced by the camera (Hartley and Zisserman, 2004).

2.2.4.4 3-D estimation

The 3-D location of each landmark for each frame of the subsequence was estimated using a least-squares approach. An initial guess for the 3-D location of a given landmark was provided, and the projection error for this location was calculated by measuring the difference between the pixel coordinates of the 3-D location as projected onto the three camera views using their respective pinhole camera models and the digitized pixel coordinates. Least-squares optimization (using the SciPy `optimize.leastsq` function, `http://www.scipy.org`) was used to refine the initial guess to the 3-D location that minimized the projection error as seen by the three camera views. In the cases where a feature was only visible in two of the three camera views, the projection error was calculated using two camera views instead of three. If, for a given feature and frame, a 3-D location could not be found where the total

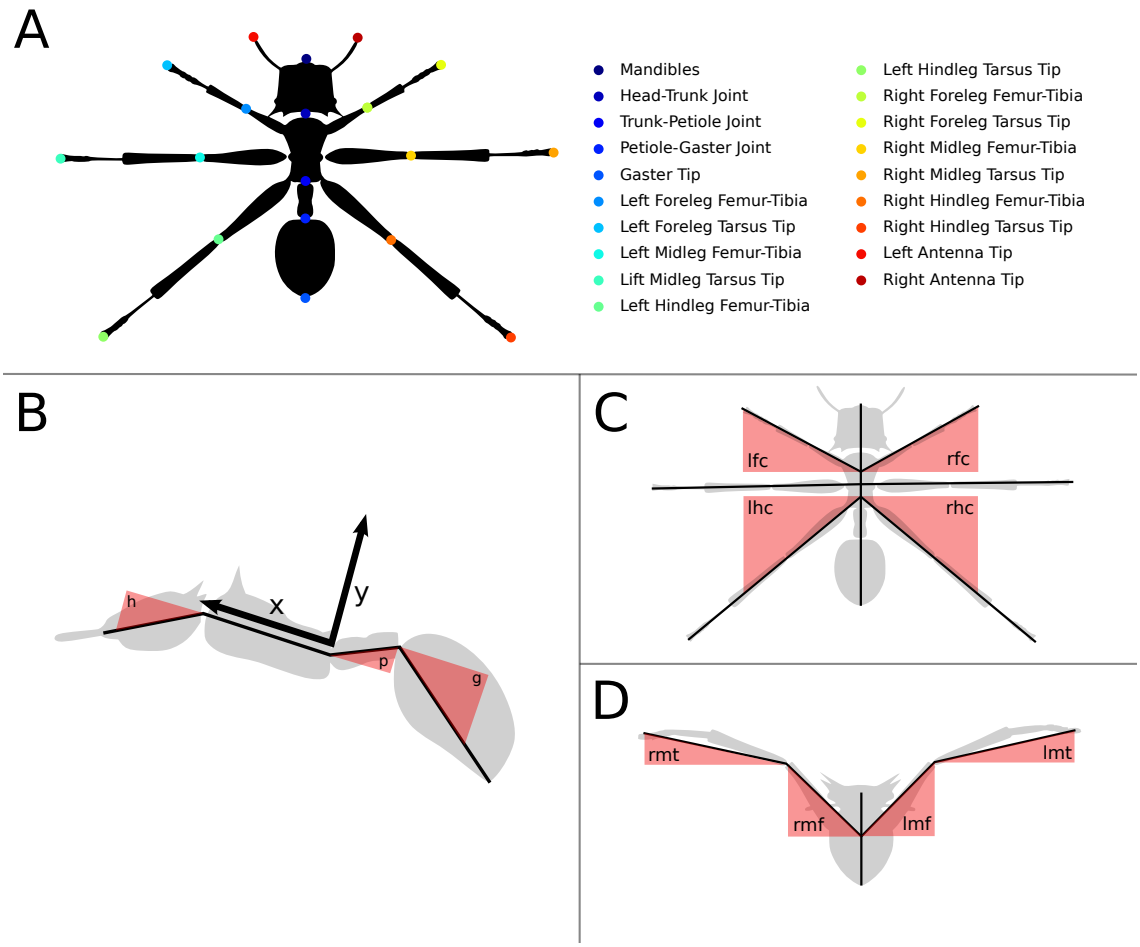

Figure 2.3: A) Locations of 19 tracked features, with a key to these landmarks. B) In the alternative joint angle representation, the local coordinate system is set so that the X-axis is aligned with the trunk of the ant, and the Y-axis is aligned dorso-ventrally. The Z-axis, not shown, is positive on the right-hand side of the ant. Relative to the trunk heading, the head, petiole and gaster are confined to motion within the sagittal plane. C) The fore-aft positions of the legs are controlled in the joint-angle model by changes in the coxal angles, which are confined to motion in the X-Z plane. D) Each leg is then represented by a femur connected to a fused tibia-tarsus, and these are confined to motions within the plane of the coxa from which they originate.

magnitude of the projection error was less than 5 pixels, the 3-D point was discarded. This required that features be digitized with an accuracy of ± 1 pixel in each camera view to be considered trustworthy.

2.2.4.5 Data smoothing and interpolation

The 3-D data for the features were then smoothed and interpolated using 3-D cubic B-splines, calculated using the SciPy functions `interpolate.splprep` and `interpolate.splev`. The B-splines were fit with a smoothing factor of 10^{-4}, and the spline values were then evaluated at intervals of 3.3 ms — i.e. a fivefold increase in sampling rate compared to the video data frame rate of 60 frames per second.

2.2.5 Joint-angle model

The estimated 3-D feature locations were used to estimate the posture held by the ant in each frame using a simplified joint-angle representation of the articulation of *C. atratus*. In this process, for a given frame the 19 3-D feature locations were converted into 21 joint angles representing the posture of the ant (Figure 2.3 shows this conversion process graphically).

The joint-angle representation relies on first defining a local coordinate system aligned with the trunk of the ant, and then using the coordinates of the digitized features in this local system to estimate joint angles.

2.2.5.1 Defining a local coordinate system:

The desired local coordinate system was one in which the x' axis was aligned with the anteroposterior axis, the y axis was aligned with the dorsoventral axis, and the z' axis was aligned with the sinistrodextral axis. The first step in defining this local coordinate system was to specify the local $x'y'$ plane (equivalent to the sagittal plane of the ant) using the 3-D locations of the axial features (the mandibles, head-trunk joint, trunk-petiole joint, petiole-gaster joint and sting; see Figure 2.3).

The coefficients of the plane $ax + by + cz + d = 0$ best fitting the axial points were determined using singular value decomposition (see Figure 2.3B). This plane was chosen as the sagittal plane of the ant, and the local z-axis of the ant was chosen as the normal to this plane ($[a, b, c]$). The local x-axis, or anteroposterior axis, was defined as the unit vector aligned with the trunk (i.e. the vector between the head-trunk joint and the trunk-petiole joint features), and the local y-axis, or dorsoventral axis, was chosen as the unit vector orthogonal to the x and z axes.

2.2.5.2 Axial joint angles:

A qualitative review of the video data revealed that gliding *C. atratus* ants in the wind tunnel primarily move the head, petiole and gaster dorsoventrally as opposed to sinistrodextrally. In the interest of the simplicity of the joint-angle model, it was assumed that the three axial

joints (head, petiole and gaster) were confined in movement to the xy (sagittal) plane, and so angles for these joints were calculated by computing the angle between the vector between the two ends of a joint and the unit y vector using the dot product:

$$\theta = \cos^{-1}(\hat{\mathbf{a}} \cdot \hat{\mathbf{b}}) \tag{2.1}$$

where θ is the angle between the unit vectors $\hat{\mathbf{a}}$ and $\hat{\mathbf{b}}$.

2.2.5.3 Leg joint angles:

While the leg of *C. atratus*, like all insect legs, has three joints between the femur and the trunk (the trunk-coxa joint, the coxa-trochanter joint and the trochanter-femur joint), it was not possible to resolve all of these joint angles with the 19 available digitized feature locations. A qualitative review of the video data provided reassurance that during bouts of gliding, the femurs were primarily rotated around the dorsoventral and anteroposterial axes; impacts with the walls of the working section tended to result in more complex leg bending modes, but these postures were not included in the analysis. Therefore, in the simplified joint angle model, each leg has three modes of articulation. The coxa angle rotates the entire leg about the local y axis, allowing for fore-aft motion of the legs. Each leg then has a femur and tibia joint, which are confined to rotation within the plane containing the coxa vector and the y unit vector, thereby enabling the femurs and tibiae to be raised and lowered dorsoventrally.

Calculation of these leg joint angles first requires the estimation of the femur for each leg, which in turn requires that the position of the coxae be estimated relative to the trunk vector. Based on morphometric estimates made from photographs of *C. atratus* trunks (the same photographs used for the morphometric analysis in Appendix B), the coxae locations in the joint-angle model were equally spaced along the trunk and displaced dorso-ventrally from the trunk axis vector by 0.2 trunk-lengths. The femur vectors were then defined as connecting the coxae to the femur-tibia joint of their respective legs. The six coxa angles were estimated by projecting the femur vectors onto the xz plane using the formula

$$\mathbf{A}_{\parallel}\hat{\mathbf{B}} = \hat{\mathbf{B}} \times \mathbf{A} \times \hat{\mathbf{B}} \tag{2.2}$$

where $\mathbf{A}_{\parallel}\hat{\mathbf{B}}$ represents the projection of the vector $\mathbf{A}$ onto a plane whose normal is defined by the unit vector $\hat{\mathbf{B}}$. The coxa angle for each leg was then defined as the angle between this projected femur vector and the local x unit vector. In a similar fashion, the femur and tibia angles (i.e. their dorso-ventral elevation, as illustrated in Figure 2.3D) were computed as the angle between the femur and tibia vectors and the local y axis.

2.2.6 Centroid and heading

The central hypothesis of this study states that *C. atratus* ants control the magnitude and direction of the net aerodynamic force acting upon them by changing posture. Evidence

of such control may be found by looking for correlations between changes in posture and changes in both the motion and body orientation of the ant while gliding in equilibrium. The motion of the ant over the course of a gliding bout was calculated by computing the location of the geometric center of the ant in each frame (approximated as the geometric centroid of the five axial features) and differentiating this positional data with respect to time.

The body orientation of the ant in each frame was defined as the trunk vector (i.e. the local x axis used in developing the joint-angle representation) expressed in the world coordinate system. This orientation vector represents the pitch and yaw orientation of the ant. A qualitative review of the video data did not reveal major visible changes in roll angle during steady gliding bouts.

2.2.7 Testing postural control

The final data set used for postural analysis consisted of a frame-by-frame account of the location of the geometric centroid of the ant, the vector heading of its central axis, and the 21 joint angles describing the orientation of its limbs. The centroid, heading and joint-angle data were imported into R (Version 2.13, `http://www.r-project.org`) for further analysis.

2.2.7.1 Aerodynamic stability

Passively stable parachuting objects achieve aerodynamic stability by elevating the center of aerodynamic pressure above the center of mass, creating a moment arm between the opposing aerodynamic and gravitation forces acting on the object. In *C. atratus*, the legs have a higher surface area to mass ratio relative to the axial body parts, and so a plausible aerodynamically stable posture for a gliding ant would most likely have the legs elevated above the axial body parts. The joint angles measured from the analyzed bouts of gliding were examined to determine the extent to which *C. atratus* adopts an elevated-leg posture while gliding.

2.2.7.2 Control of pitch orientation

As discussed in the Introduction, changes in pitch orientation were expected to be correlated with changes in the fore-aft location of the center of aerodynamic pressure, which is dependent on the fore-aft distribution of surface area. The most likely way for a *C. atratus* ant to adjust its fore-aft distribution of surface area without significantly adjusting the location of its center of mass would be to change the fore-aft angles of its legs (i.e. the coxae angles, in the joint-angle representation).

To determine whether this was indeed the mechanism by which the ants adjusted their orientation, for all pairs of legs (fore-, mid-, and hind-legs) in all frames of a given gliding bout, the coxa angles were compared with the pitch heading of the ant using a hierarchical linear mixed-effects model (using the `lme` function from the R `nlme` library) with the fixed

effect of the model being the global trend relating the coxa angles to overall pitch angle, and the random effects indicating the deviation by individual glide bouts from the global trend.

2.2.7.3 Control of turns

Turns in flyers are typically achieved through left-right asymmetries in generated lift (Alexander, 2003; Etkin and Reid, 1996; Taylor, 2001; Thomas and Taylor, 2001). In *C. atratus*, turns are expected to be correlated with left-right asymmetries in leg posture. Possibilities include fore-aft leg angle as well asymmetric dorso-ventral elevation angles; for each pair of legs, a hierarchical linear mixed-effects model was used to determine whether left-right asymmetries in the leg angles were correlated with turns, with the fixed effect being the global trend relating mean leg-pair angle to horizontal sideways motion by the ant, with the random effects accounting for individual deviation from the global trend. Horizontal sideways speed was computed as the component of the ant velocity orthogonal to both the direction of air flow and the local anteroposterior axis of the ant.

2.2.7.4 Control of lift-to-drag ratio

Flower (1964) postulated that wingless insects could generate lift by holding their bodies, approximated as a cylinder, at an angle to the incident flow field while falling. Modulating the pitch angle, by this model, would be expected to change the lift-to-drag ratio of the gliding ant. Again, a hierarchical mixed effects model was used to model the effect of pitch angle on horizontal fore-aft velocity, with the global trend modeled as a fixed effect and individual deviations from the global trend modeled as a random effect.

2.3 Results

2.3.1 Summary of collected sequences

Five subjects (mass = 30±8 mg) were used in trials. and each subject was dropped into the wind tunnel at least five times. From the 41 videos that were obtained in total, 20 sequences of 10-30 frames (median=16 frames) were selected for posture analysis. These sequences were digitized and processed as described in Section 2.2.4, yielding for each sequence the 3-D locations of the tracked features. From these feature locations the centroid, heading, and joint angles were determined.

2.3.2 Video data

An example frame from a representative video sequence is shown in Figure 2.4, showing a characteristic gliding posture with the anteroposterial axis held inclined to the horizontal and all legs elevated.

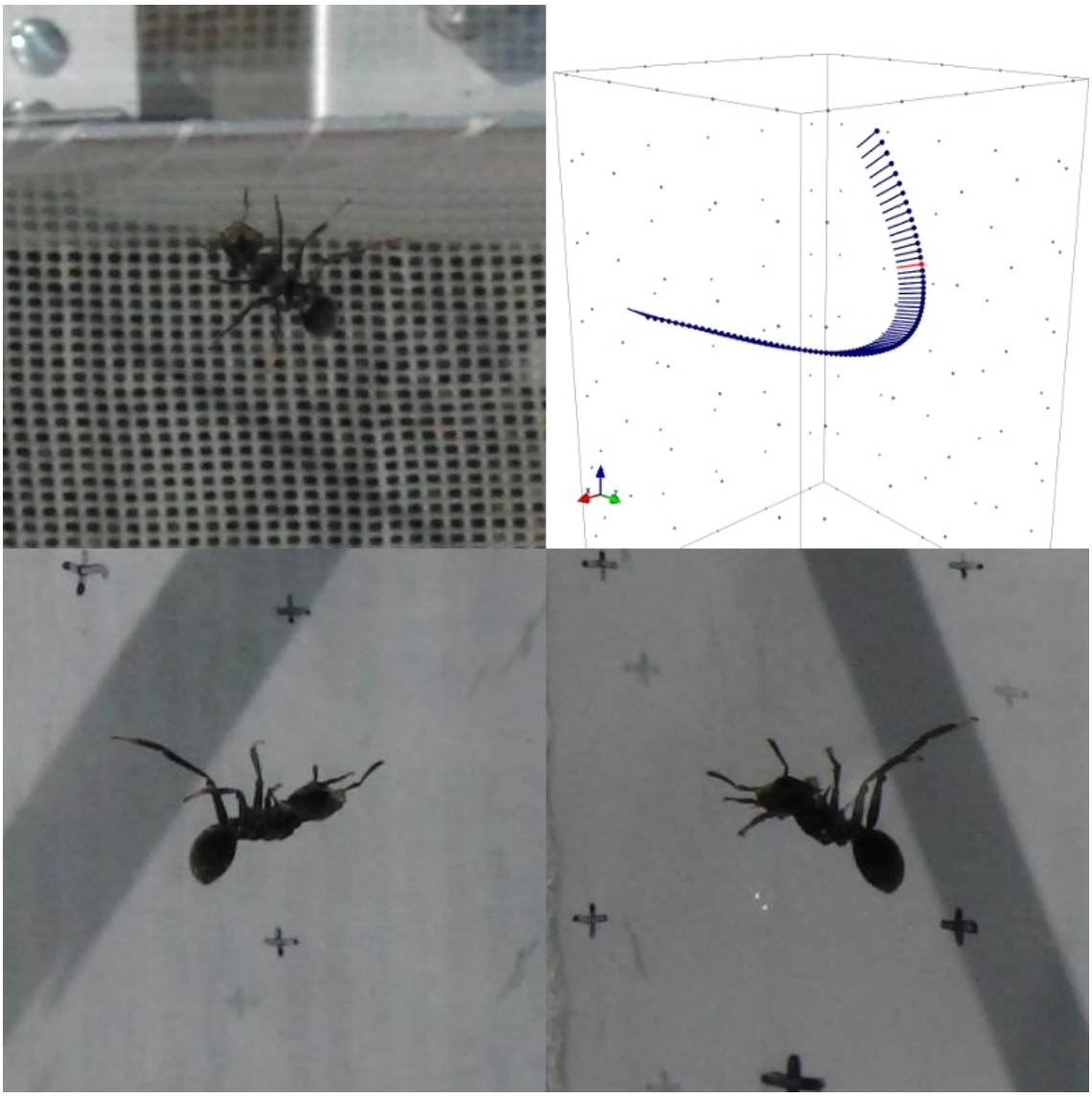

Figure 2.4: Example frame of video used for postural analysis. Each frame consisted of a three-up composition of the top, front and side camera views, each cropped to a 400×400 pixel window centered on the ant. The ball and stick trajectory for this glide sequence (see Figure 2.6 is shown at top right, with the current frame highlighted in red.

2.3.3 Tracked features

In Figure 2.5, for a single gliding sequence (the same gliding sequence from which the single frame in Figure 2.4 was extracted), the 3-D trajectories followed by all 19 tracked features are shown along with stick figure representations of the ant posture at every 5th frame. In Figure 2.5, it is possible to see a variety of postural changes as well as changes in both the heading of the ant and its direction of motion.

2.3.4 Kinematics

As discussed in the Methods, the kinematics of postural change, centroid velocity and body orientation were measured from the 3-D digitized data using a joint angle model. In Figure 2.6, the body kinematics for all analyzed glide sequences are shown using ball-and-stick models. The sticks are centered on the centroid of the ant body and the long axis of the stick is aligned with the local x axis of the ant body in each frame. The anterior end of the ant is indicated with a ball on one end of the stick.

In Figures 2.7 and 2.8, time series representing body kinematics and postural kinematics, respectively, are shown for a single analyzed glide sequence (the same sequence used in Figure 2.5. Figure 2.7 shows changes in the orientation vector of the ant and the 3 components of velocity over the range of the analyzed sequence. In this representative figure, variability is observed in all of the body kinematics — over the course of the glide sequence, the ant changes orientation in both pitch and yaw while simultaneously undergoing large changes in velocity. Figure 2.8 shows a subset of the joint-angle kinematics exhibited by the ant over the course of the same sequence, where femur and tibia elevation angles of all six legs have been omitted to conserve space. In Figure 2.8 it is clear that, over the course of the analyzed sequence, the axial joint angles (head, petiole, and gaster) as well as the fore-aft angles of all six legs are all changing with time.

2.3.5 Ensemble joint angles

The ranges of joint angles observed in all gliding sequences are presented as box plots in Figures 2.9 and 2.10. The samples from all sequences were joined as an ensemble and treated as independent samples to make these plots; the data in the box plots is also included in Table 2.1.

2.3.6 Stability

From the collected joint angle data treated as an ensemble, it can be seen that gliding *C. atratus* ants adopt a gliding posture where all six legs are elevated dorsoventrally above the anteroposterior axis, and the gaster is flexed dorsoventrally below the anteroposterior axis. The mean gaster flexion angle was 51.6°, and legs were elevated by 40-50° dorsoventrally; full statistics are presented in Table 2.1.

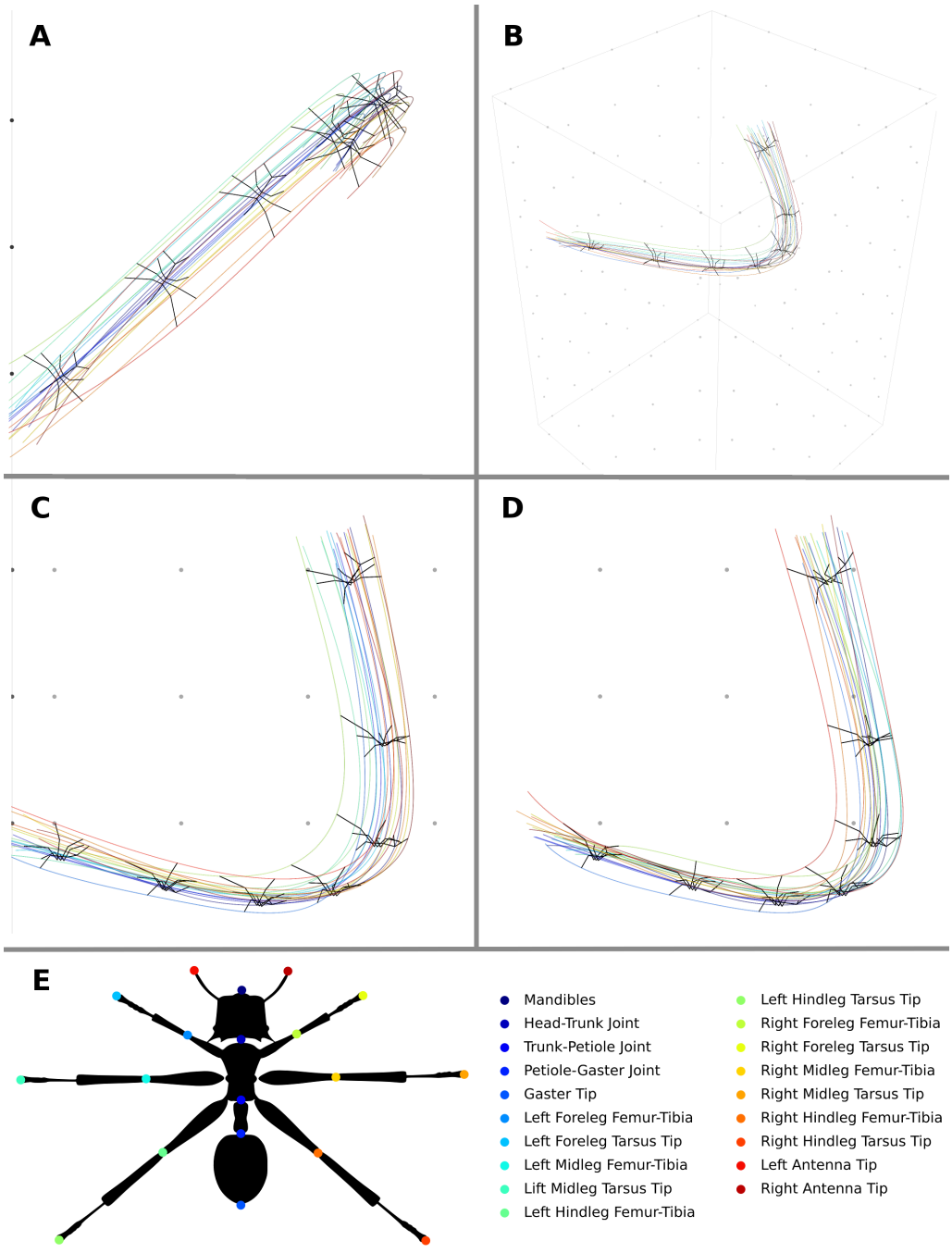

Figure 2.5: Four views showing a stick figure representation of an ant gliding in a wind tunnel. A) Top view (note asymmetric changes in fore-aft positioning of legs, correlated with changes in heading; B) an isometric perspective; C) and D) Front and side views, respectively; E) Key relating colors of trajectories to features.

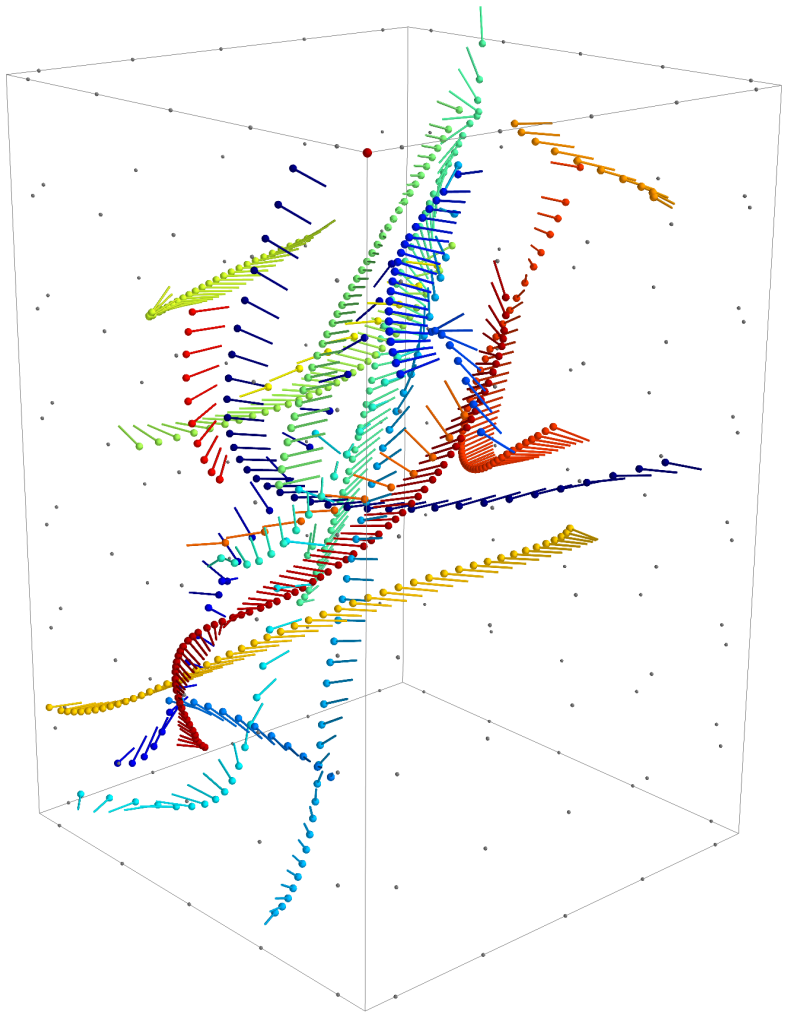

Figure 2.6: Simplified trajectories of all gliding sequences used in this study showing changes in ant heading and motion of centroid. The sticks show heading of ant in pitch and yaw, and the balls indicate the anterior end of the ant. The boundaries of the wind tunnel are shown in grey, and the calibration markers (spaced 3 cm apart from one another) are shown for scale.

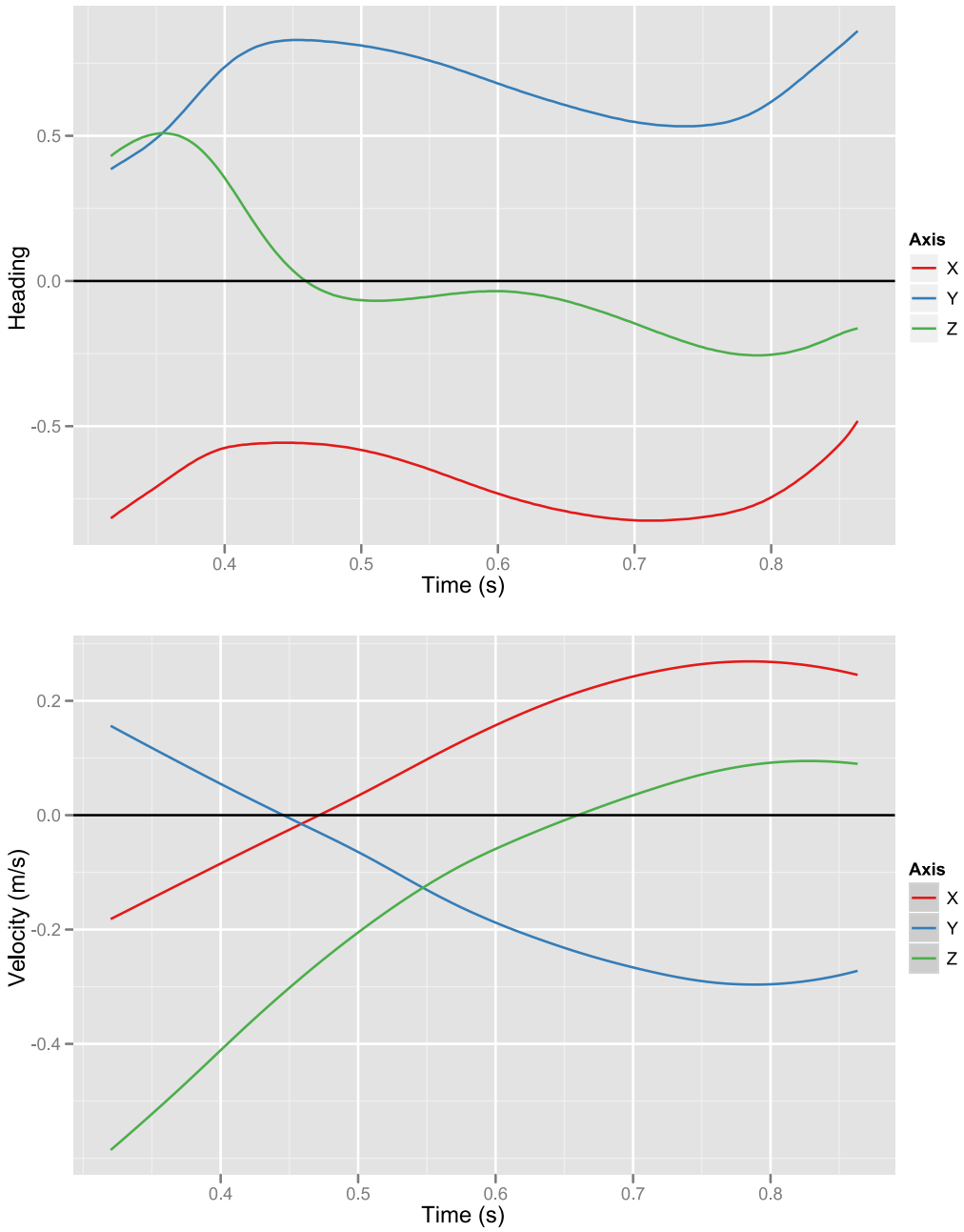

Figure 2.7: Body kinematics of glide sequence shown in Figure 2.5. **Top:** Changes in the 3-D angular orientation the ant as a function of time. The orientation is represented by a unit vector aligned with with local x axis of the ant body. The components of this unit vector when transformed into the XYZ coordinates of the wind tunnel working section are plotted here. **Bottom:** 3-D components of the velocity of the ant in the wind tunnel coordinate system plotted as a function of time.

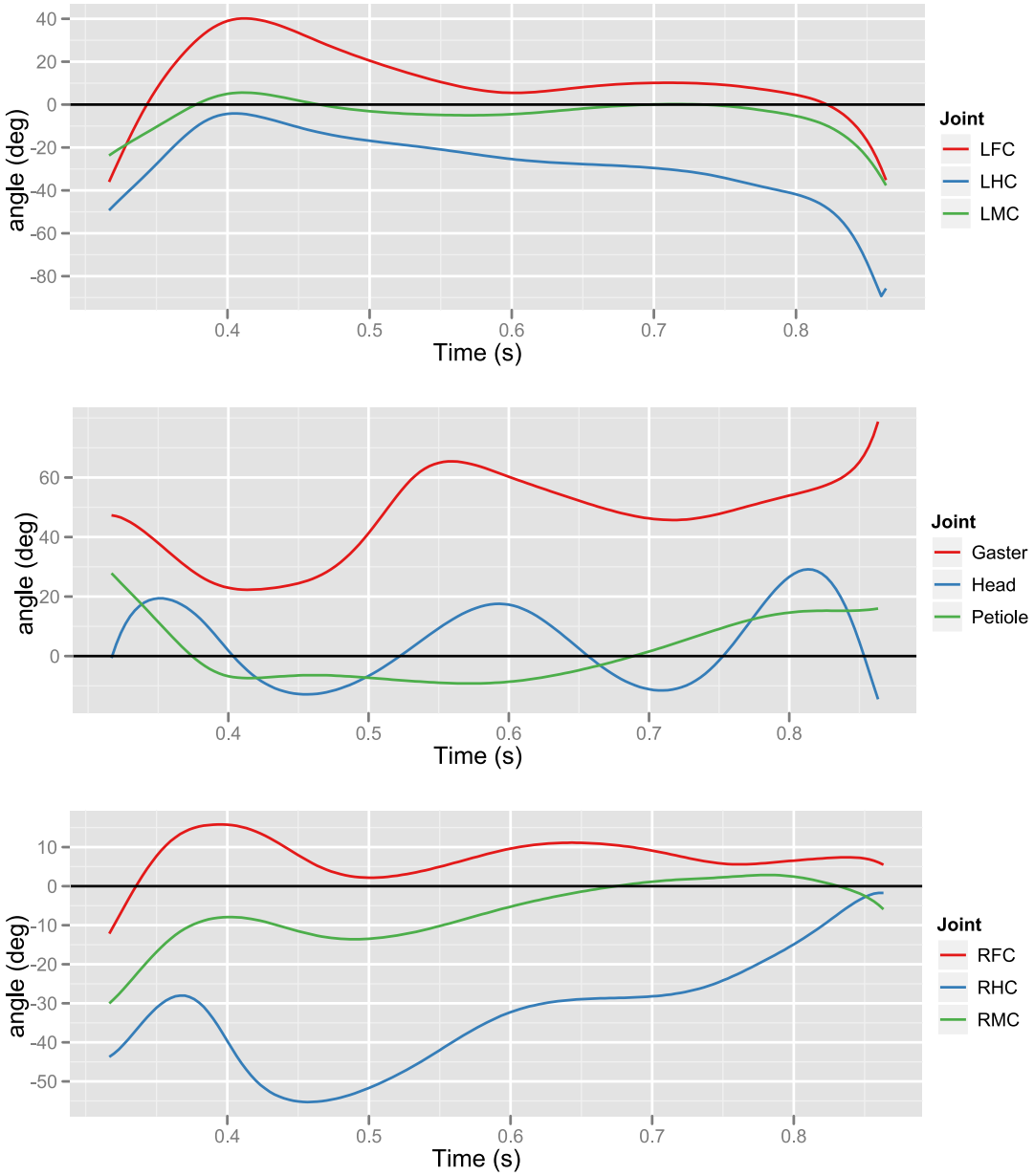

Figure 2.8: Posture kinematics of glide sequence shown in Figure 2.5. **Top:** Changes in the fore-aft coxae angles on the left side of the body, plotted against time. **Middle:** Changes in the dorsoventral flexion angle of the axial joint angles plotted against time. **Bottom:** Changes in the fore-aft coxae angles on the right side of the body, plotted against time.

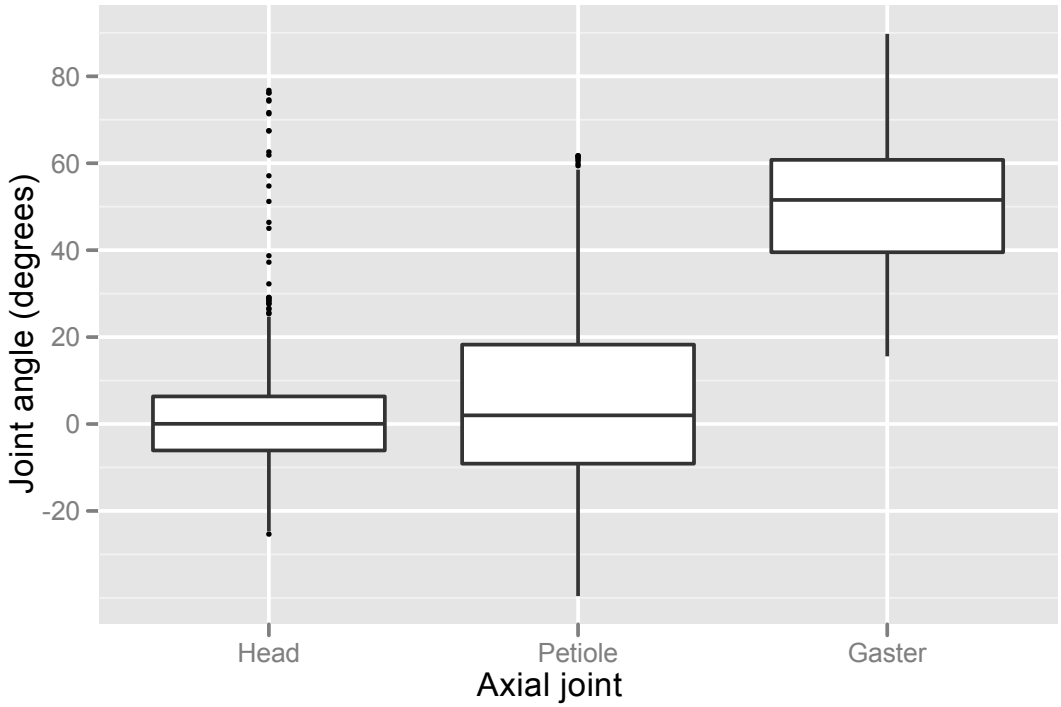

Figure 2.9: Boxplots showing measured variation in all axial joint angles for the ensemble dataset. Relevant statistics used to create these boxplots may be found in Table 2.1.

2.3.7 Pitch control

Figure 2.11 shows, for all analyzed sequences, body pitch orientation plotted against gaster flexion angle. Qualitatively, there is an apparent trend in the data which appears to show that low pitch angles ($< -10°$) correspond to low gaster flexion angles ($< 40°$), and higher pitch angles ($> +10°$) correspond to higher gaster flexion angles. To investigate this further, data from all trajectories were pooled and partitioned into two groups according to instantaneous body pitch angle, with one group containing all data where the instantaneous body pitch angle was $< -10°$ and the other group containing all data where the instantaneous pitch angle was $> +10°$. Within these datasets, the data were partitioned into individual sequences ($N = 5$ for pitch $< -10°$, $N = 10$ for pitch $> +10°$) and the median gaster flexion angle for each sequence was computed. A Welch two-sample t-test performed on the two groups of median gaster flexion angle values indicated support for the two groups having different means ($\mu_{\alpha<-10°} = 35.6°$, $\mu_{\alpha>+10°} = 54.2°$, $t = -2.75$, df $= 12.2$, $p = 0.017$).

However, when all data from all trajectories were considered together as part of a hierarchical linear mixed effects model (described in the Methods), support for a general trend linking pitch angle and gaster flexion was not found. A significant general trend was also not found for mean hind-leg coxa angle or the mean mid-leg coxa angle.

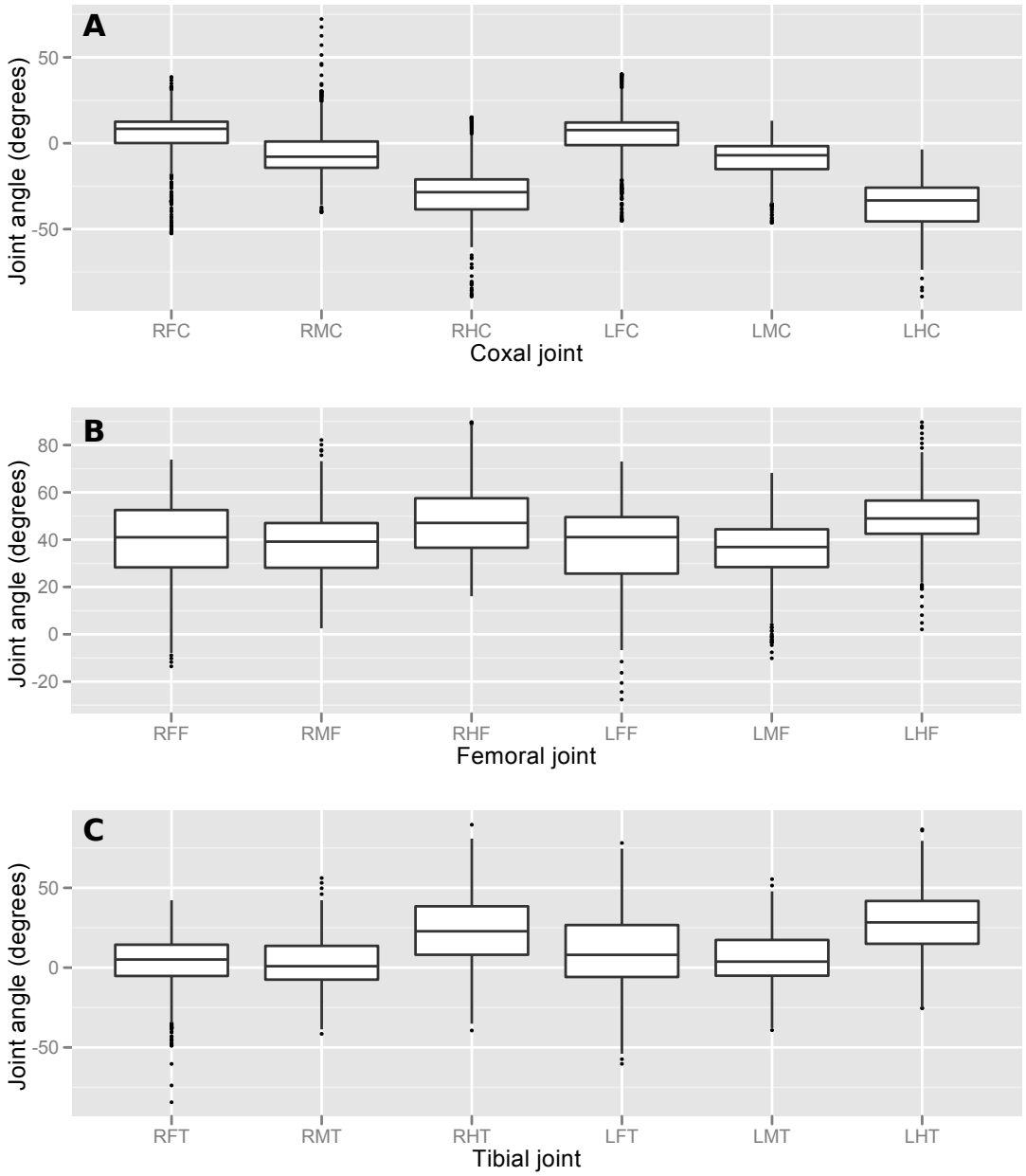

Figure 2.10: Boxplots showing measured variation in all leg joint angles for the ensemble dataset. Leg angles are referred to using a code of the form ABC, where A is a member of [L, R], denoting left or right; B is a member of [F, M, H], denoting fore-, mid-, or hind-leg; and C is a member of [C, F, T], denoting coxa, femur or tibia. **A:** Variation in coxa joint angles, controlling fore-aft leg angles. **B:** Variation in femoral joint angles, controlling dorsoventral elevation of the femurs. **C:** Variation in tibial angles, controlling dorsoventral elevation of the tibiae.

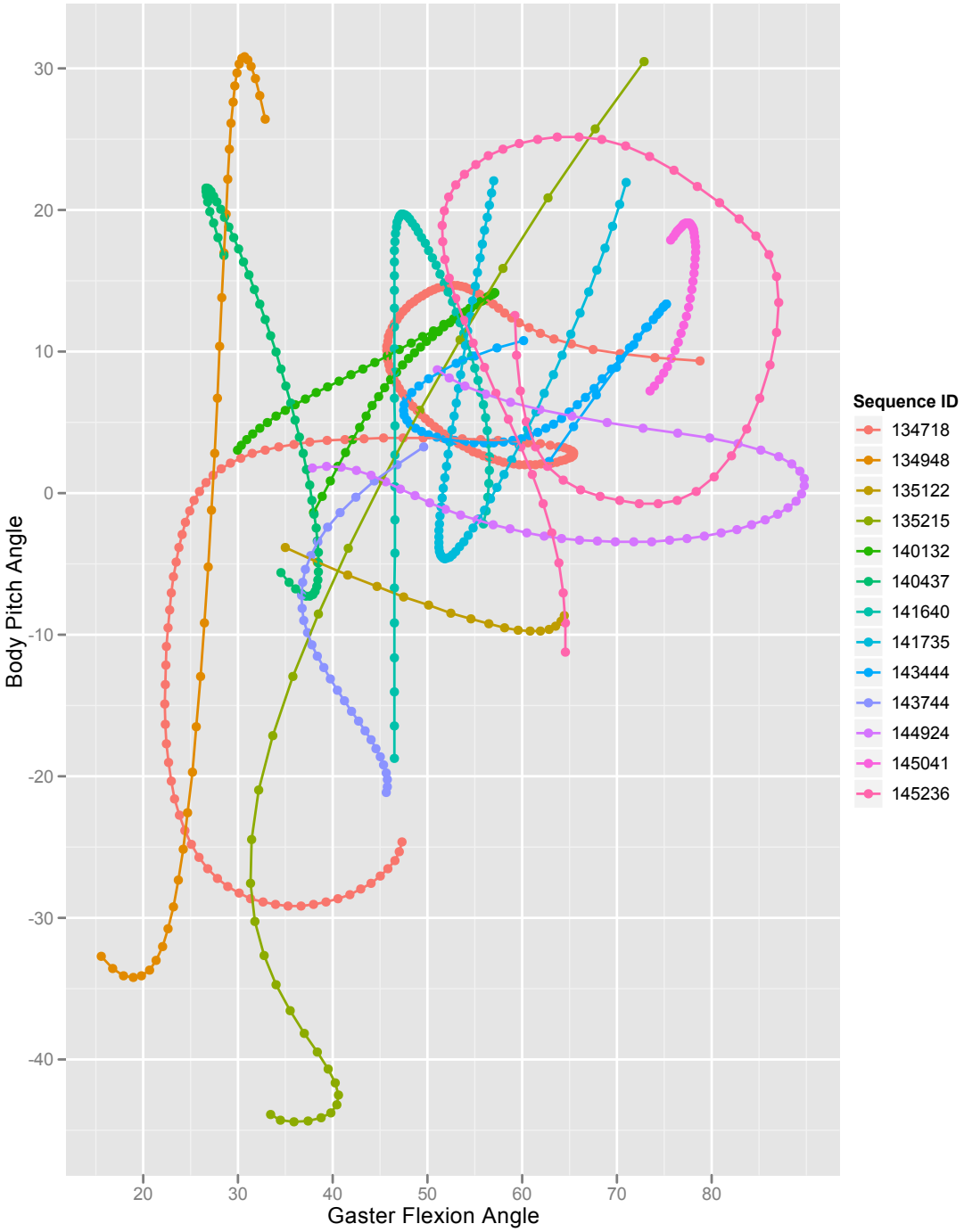

Figure 2.11: Instantaneous body pitch angle plotted against gaster flexion angle. Individual sequences are marked with different colors.

	Min	1st Quartile	Median	Mean	3rd Quartile	Max
Head	-25.3	-6.1	0.1	1.6	6.4	76.8
Petiole	-39.6	-9.1	2.0	5.4	18.3	61.8
Gaster	15.6	39.5	51.6	51.4	60.8	89.8
RFC	-52.5	0.1	8.4	4.6	12.5	38.6
RFF	-13.6	28.3	41.0	40.0	52.5	73.8
RFT	-84.3	-5.2	5.0	2.7	14.3	42.2
RMC	-40.2	-14.2	-7.8	-5.6	1.0	72.2
RMF	2.5	28.1	39.1	38.3	47.0	82.1
RMT	-41.4	-7.5	0.9	2.1	13.6	56.1
RHC	-89.2	-38.5	-28.4	-29.3	-21.0	15.1
RHF	16.0	36.6	47.0	47.8	57.5	89.7
RHT	-39.3	8.0	22.7	24.2	38.4	89.5
LFC	-45.2	-1.1	7.6	4.5	12.0	40.1
LFF	-27.6	25.6	41.0	38.1	49.5	73.0
LFT	-60.2	-5.8	8.0	9.8	26.6	78.0
LMC	-46.3	-15.0	-7.0	-8.9	-1.6	13.1
LMF	-10.1	28.4	36.8	36.8	44.3	68.2
LMT	-39.2	-5.0	3.7	6.1	17.3	55.4
LHC	-89.2	-45.5	-33.3	-35.2	-25.8	-3.6
LHF	2.0	42.5	48.9	49.4	56.5	89.6
LHT	-25.3	14.9	28.3	26.9	41.7	86.6

Table 2.1: Summary statistics for all postural angles in the ensemble dataset.

2.3.8 Fore-aft lift control

Figure 2.12 shows the variation, for all analyzed sequences, of horizontal fore-aft glide velocity (i.e. the component of the ant glide velocity orthogonal to the air flow direction and the local sinistrodextral axis of the ant body) with body pitch angle. A hierarchical mixed effects model fit to the data found no evidence supporting an overall trend linking these two variables.

2.3.9 Sideways lift control

Figure 2.13 shows the variation, for all analyzed sequences, of horizontal sideways glide velocity (i.e. the component of the ant glide velocity orthogonal to the air flow direction and the local anteroposterior axis) with the difference in hind-leg coxa angle, indicating asymmetry in fore-aft hind-leg posture. Differences in hind-leg coxa angles of up to $\pm 40^\circ$ were observed, but a hierarchical mixed effects model found no evidence for a general trend in the variations of these variables across individual bouts of gliding.

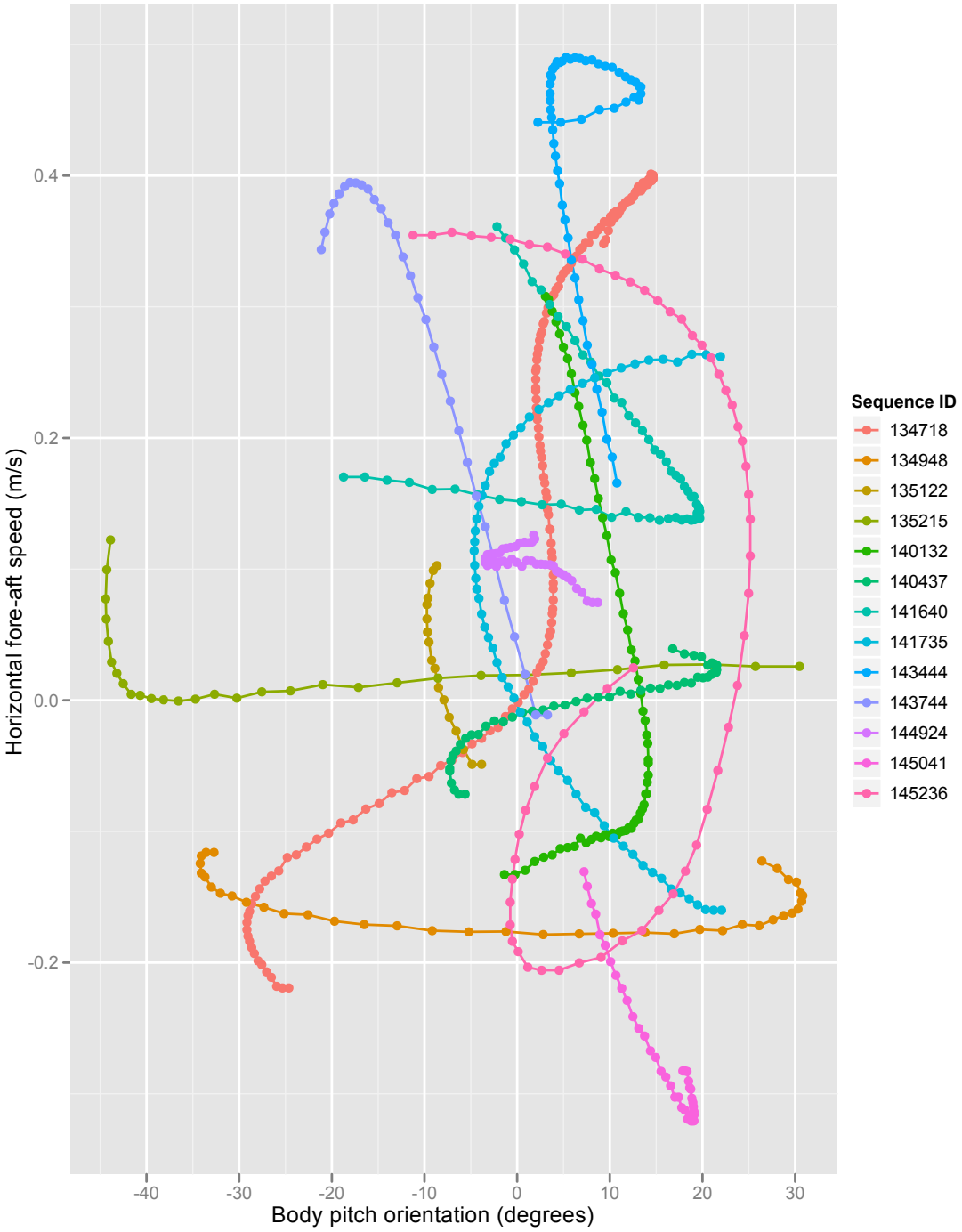

Figure 2.12: Instantaneous horizontal fore-aft speed (i.e. component of lift aligned with the anteroposterior axis of the ant) plotted against instantaneous body pitch orientation for all analyzed sequences.

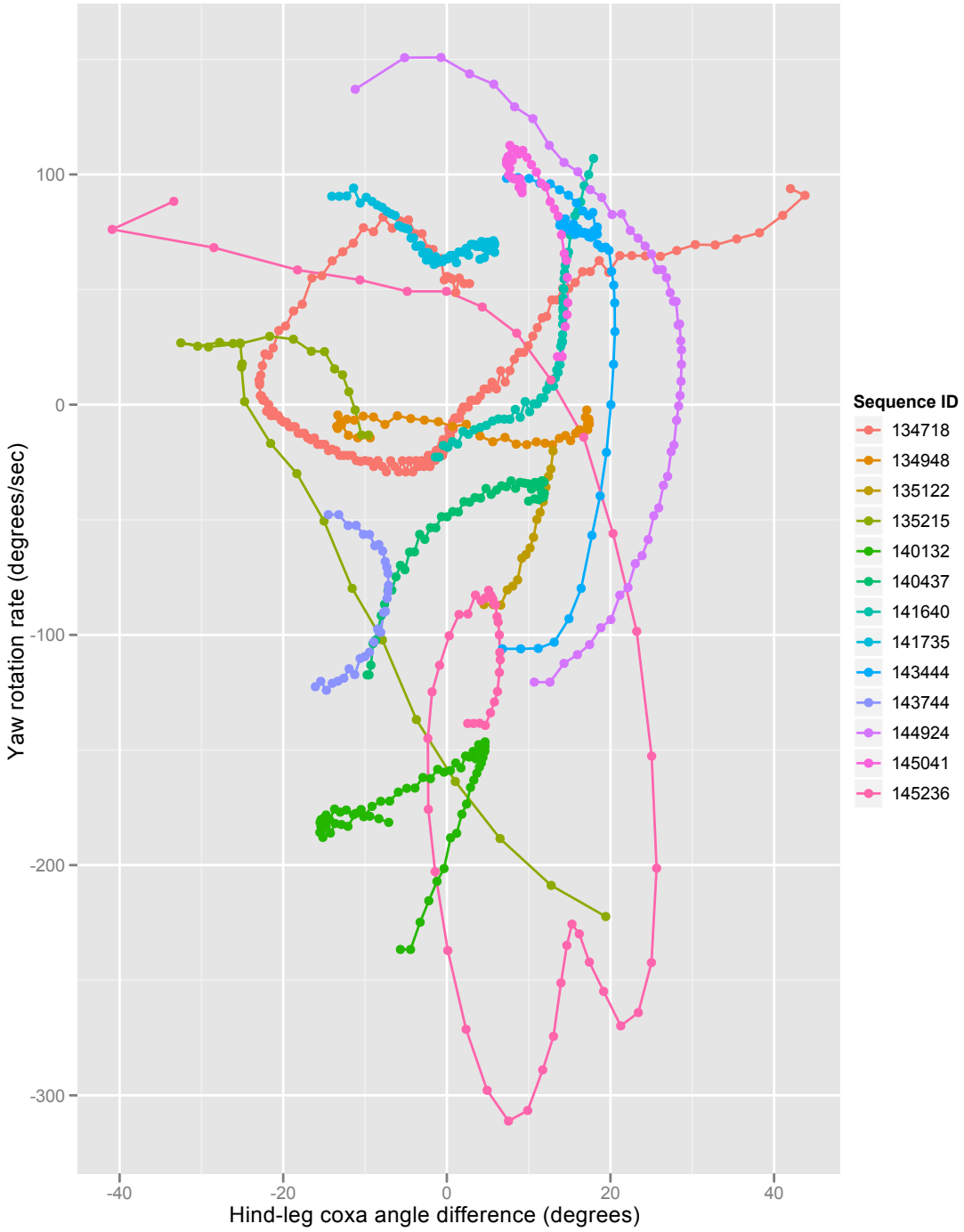

Figure 2.13: Instantaneous horizontal left-right speed (i.e. component of lift orthogonal to the anteroposterior axis of the ant) plotted against instantaneous fore-aft asymmetry of hind-leg coxa angles.

2.4 Discussion

The wind tunnel videos collected for this study provide an unprecedented view of how gliding *C. atratus* ants utilize posture. A kinematic analysis shows that the median posture held by a gliding *C. atratus* ant is characterized by the legs being elevated dorsoventrally above the anterposterior axis, and the gaster being flexed downwards underneath the body. Mean hind-leg elevation angle was 48.7°, mean mid-leg elevation was 37.6°, and mean fore-leg elevation was 41.3°, where 0° elevation would indicate horizontally outstretched leg. This is similar to elevated-limb skydiving postures observed in other animals (e.g. geckos (Jusufi et al., 2008)).

Large angular changes in gaster flexion angle and fore-aft leg coxa angles were observed in the analyzed trajectories, which were hypothesized to allow the ant to control the net aerodynamic force and moment acting upon it, thereby allowing the ant to perform pitching and turning maneuvers. A qualitative analysis of instantaneous body pitch angles and gaster flexion angles revealed that postures with high instantaneous gaster flexion angles corresponded to high instantaneous body pitch angles, and low gaster flexion angles corresponded to low instantaneous body pitch angles.

However, when hierarchical linear mixed model analyses were used on the data to attempt to uncover general trends linking instantaneous posture and instantaneous body kinematics, no statistically significant general trends were found. This is likely due to the fact that, in this kinematic analysis, the dynamics of the ant motions were ignored in the statistical models used to analyse postural change. That is, the posture at a given time t was compared to the body kinematics (angular orientation and velocity) at time t, ignoring the motions of the ant prior to t. However, if the ant at time $(t - \Delta t)$ has a certain angular acceleration α, the inertia of its body will cause that acceleration to affect the body kinematics at time t — an undetectable effect using the kinematic mixed effects models employed in this study.

It is clear, then, that a kinematic approach is insufficient to determine how posture controls body kinematics in gliding *C. atratus* ants. Given a sufficiently large dataset, a dynamical systems approach could be used to model the dynamics of the system, but given the high dimensionality of the postural variables (21 joint angles in the simplified model of *C. atratus* articulation) and the body dynamics (considering both the accelerations of the center of mass and the angular accelerations of the body), the size of the data set that would be required to extract a trustworthy dynamical model is intimidatingly large.

In this case, a modeling approach towards understanding how posture influences the body dynamics in a gliding *C. atratus* ant is a greatly preferable option. If the aerodynamics of gliding in *C. atratus* can be accurately modeled, either physically or computationally, this provides a framework wherein the effects of postural change on the dynamics of the gliding ant may be measured directly. The next step in this research, therefore, is to apply a selection of the postures observed during gliding bouts in this study to an aerodynamical model of a gliding *C. atratus* ant.

Chapter 3

Stability and control in skydiving ants

3.1 Introduction

The neotropical canopy ant *Cephalotes atratus*, despite exhibiting an absence of obvious morphological adaptations for aerial behavior, is capable of performing targeted directed aerial descent while falling. Following a fall from the rainforest canopy, *C. atratus* ants stabilize their descent, visually target a nearby tree trunk or other vegetative structure, and glide towards and land upon their target, therby avoiding a fall to the forest floor (Yanoviak and Dudley, 2006; Yanoviak et al., 2005). Gliding to a tree trunk rather than falling to the forest floor is likely advantageous in preventing a fallen worker from becoming separated from navigational chemical trails and in avoiding opportunistic attacks from ground- or water-dwelling species, often other ant species or insectivorous fish (Yanoviak et al., 2011) — impacts with hard substrates for *C. atratus* ants falling at their terminal velocity ($\sim$4 m/s) are not expected to be fatal (Flower, 1964; Yanoviak et al., 2005). Gliding *C. atratus* ants follow steep, curving, 3-dimensional trajectories towards their targets; a 3-D analysis of the shapes of these trajectories indicate that ants have some degree of control over the direction of the net aerodynamic force acting upon them while falling, allowing them to produce fore-aft and sideways motions (Chapter 1).

Drop experiments using *C. atratus* ants with ablated hind-legs, mid-legs or gasters, as well as combinations of those ablations, indicate that glide performance is severely diminished in the absence of the hind-legs (Yanoviak et al., 2010). Wind tunnel experiments conducted on *C. atratus* workers in a vertical wind tunnel have revealed that gliding *C. atratus* ants adopt a characteristic gliding posture in which the legs are held dorsoventrally elevated above the anteroposterior axis, with the gaster flexed downward (Yanoviak et al. (2011), Chapter 2). 3-D kinematic analysis of the use of posture by gliding *C. atratus* ants (Chapter 2) revealed that ants modulate their gaster flexion angle as well as the fore-aft angles of their mid- and hind-legs. Changes in the fore-aft angles of the mid- and hind-legs can either be symmetric (e.g. hind-legs both move forward by the same amount over a given time period) or asymmetric (e.g. left hind-leg moves forward while the right moves backwards). A kine-

matic analysis of postural changes and body kinematics (angular orientation and velocity direction) failed to find any significant correlations between posture and kinematics, with the important caveat that the kinematic analysis did not account for the dynamics of the system (Chapter 2. Furthermore, aerial maneuvers were not performed separately; pitching maneuvers would often occur at the same time as turning maneuvers, and pure bouts of straight gliding were rare. Therefore, to obtain a clear understanding of how changes in posture affect the aerodynamics of a gliding ant, it is necessary to exert a greater degree of control over the postural changes of a gliding ant so that the influence of a particular morphological feature over the dynamics of gliding might be demonstrated in a repeatable manner. Previous experiments have accomplished this through fixing experimental subjects to a rigid tether and exposing them to controlled visual stimuli (e.g. Arbas (1986); Hinterwirth and Daniel (2010); Zanker (1988)), other studies have avoided the use of a living organism and employed dynamically scaled physical models in their stead (e.g. Dickinson and Götz (1993); Dickinson et al. (1999); Emerson and Koehl (1990); Emerson et al. (1990); Kingsolver and Koehl (1989)). A review of dynamical scaling techniques may be found in Vogel (1994); see also Appendix A. The current study belongs to the latter school: using a morphologically accurate, dynamically-scaled model of a *C. atratus* worker ant, the variation in aerodynamic forces and moments exerted on a falling *C. atratus* ant are explored as a function of body posture.

Based on the kinematic observations presented in the Chapter 2, the following set of hypotheses were tested using a dynamically scale model:

- The aerial righting posture of the ant is passively stable, and adoption of this posture is sufficient to produce a righting maneuver without active control.
- Changes in the fore-aft positioning of the hind-legs as well as the flexion angle of the gaster should cause a significant change in the aerodynamic forces exerted on the ant, while simultaneously maintaining aerodynamic stability. These changes in aerodynamic forces should be sufficient to allow pitching and turning maneuvers.
- The postures employed by gliding *C. atratus* ants improve the aerodynamic stability of the ant: comparisons between a splayed, non-aerodynamic posture and the postures modeled after real ant behavior should demonstrate significantly greater aerodynamic stability in the latter.

An additional benefit of using models in the place of real animals is the ability to assess the relationship between morphology and performance. In previous work (Yanoviak and Dudley, 2006; Yanoviak et al., 2005, 2010, 2011), attention has been drawn to the relatively long legs exhibited by *C. atratus* in comparison to the leg length of similar sized terrestrial ants. Using dynamical models of gliding ants, the following hypotheses regarding the importance of leg length for aerodynamic stability and control may be tested:

- Ants with long legs are more aerodynamically stabile, and have a greater degree of control over the net aerodynamic force and moment they experience while falling.

- A leg length threshold exists below which aerodynamic forces on a falling ant are no longer controllable via leg posture change.

In the present study, results of a series of physical modeling experiments designed to test these hypotheses and advance understanding of the aerodynamics of skydiving in ants are presented.

3.2 Methods

The results presented in this study were obtained using a custom built robotic tow-tank apparatus, consisting of a physical model of an ant immersed in a tank of mineral oil — see Figure 3.1. The model is attached via a 6 degree of freedom force transducer to a robotic arm capable of rotating the model independently in pitch and roll, and the robotic arm is in turn bolted to a cart which allows the ant model to be towed through the mineral oil at speeds of up to 2 m/s. The forces and torques acting on the ant model are recorded as a function of posture assigned to the model, the orientation of the model in pitch and roll, and the speed with which the model is moved through the tank. In the following sections I will describe each component of the apparatus and the role it plays in the full experiment.

3.2.1 Mineral oil tank

The tank used in this experiment was made from clear acrylic plastic with dimensions 2.1 m L $\times$ 0.32 m W $\times$ 0.40 m D. The tank was filled with mineral oil having a viscosity of 0.049 Pa s (measured with a Brookfield DV-II digital viscometer, Brookfield Engineering Laboratories, Massachusetts USA) and a density of 850 kg/m^3 at lab temperature (25°C). Mineral oil was chosen as a fluid for experiments on account of its convenient force amplification factor when simulating the dynamics of objects moving through air (described in Appendix A).

Structural support for the sides of the tank was provided by a frame built from T-slotted aluminium framing (80/20 10 Series T-slot framing, `http://www.8020.net`). This frame prevented bulging of the tank when filled with mineral oil and provided a structure for mounting the towing equipment.

3.2.2 Towing apparatus

Models were towed through the oil in the tank by means of a towing apparatus attached to the aluminum frame of the tank. This apparatus consisted of a stepper motor used to drive the motion of a cart along the top of the tank, as shown in Figure 3.1. The cart was built from 80/20 T-slot framing and aluminum stock, and rolled on polyurethane scooter wheels (Kryptonics 100 mm 82A wheels with ABEC-5 bearings, `http://www.kryptonics.com`) within aluminum U-channel tracks mounted on the tank of the frame. A nylon toothed belt was connected to the cart using a custom aluminum clamping plate, and this belt was then looped around a freely rotating toothed pulley at one end of the tank and around

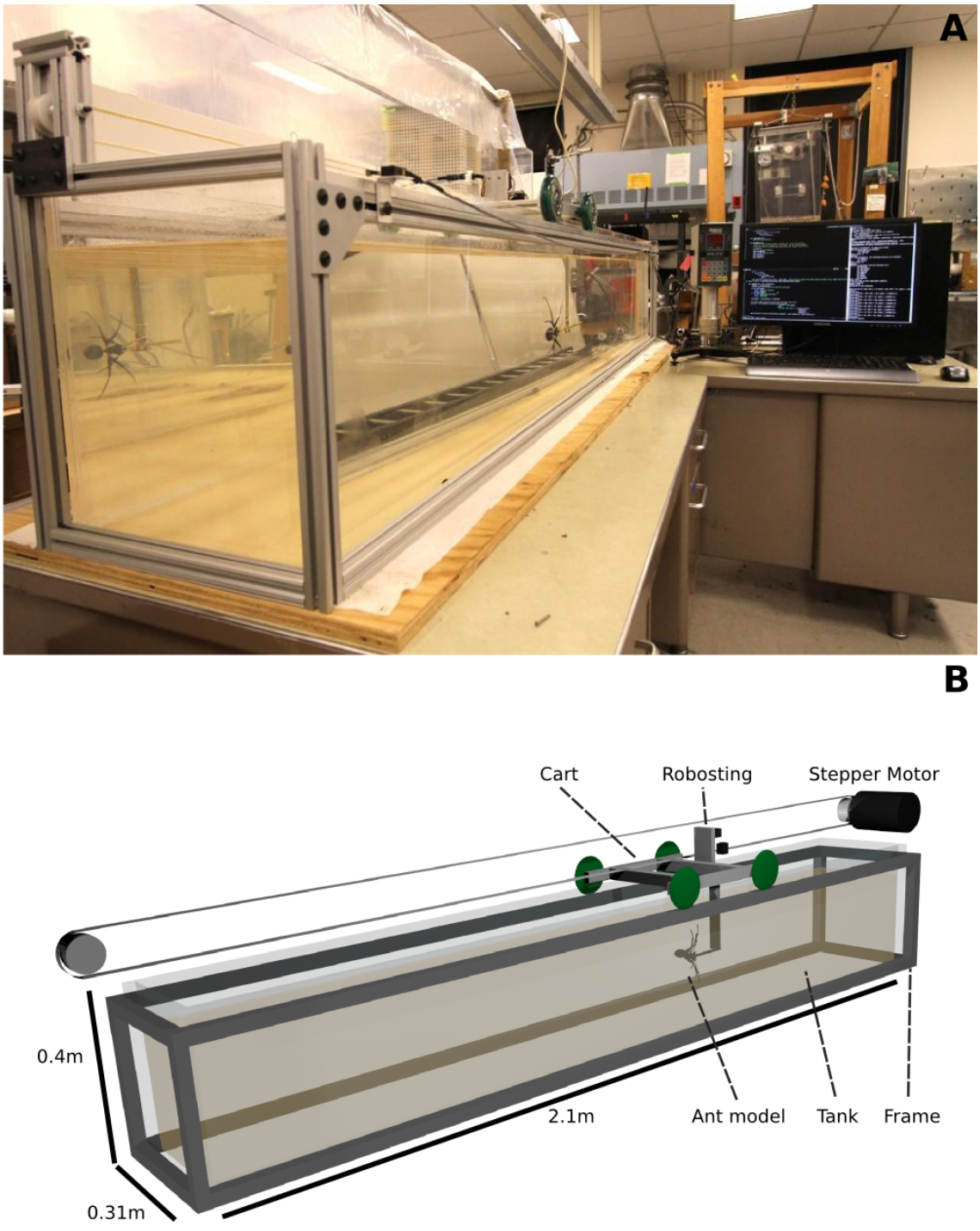

Figure 3.1: Tow tank apparatus. **A:** Photograph of apparatus. **B:** Schematic render of apparatus, with important components labeled.

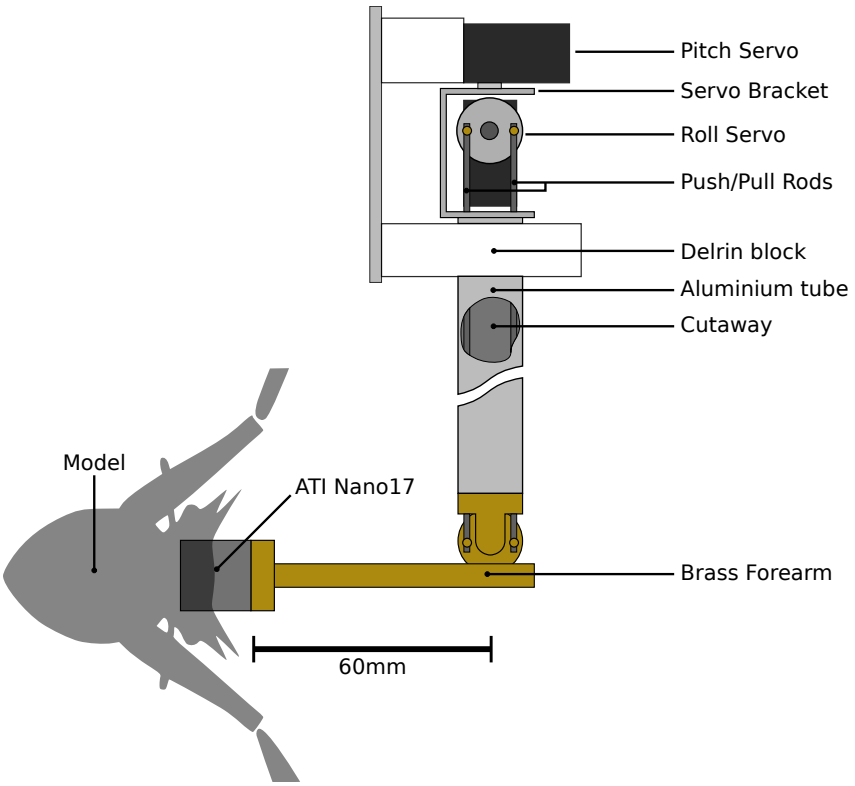

Figure 3.2: Robosting schematic, with important components labeled.

a toothed pulley connected to the drive motor at the other end of the tank. The driving motor in this apparatus was a Vexta PH2610-E2.9 standard resolution stepping motor (`http://www.orientalmotor.com`), driven and controlled by an Advanced Micro Systems SAX integrated driver/controller/power supply (`http://www.ams2000.com`). The motion of the driver was programmed via serial RS-422 connection from an attached computer (Ubuntu Linux OS, version 11.10). Limit switches were set up at either end of the tank to automatically stop the motion of the cart in the event of it overshooting its mark.

3.2.3 Robosting

A robotic arm held the model in a fixed orientation relative to the incident fluid flow was attached to the cart described in Section 3.2.2. This arm, dubbed Robosting, controlled the pitch and roll angles of the ant model by means of two hobby servo motors (Hitec HS-5475HB digital servos, `http://www.hitecrcd.com`). The Robosting is diagrammed in Figure 3.2, which shows the orientation of the two servo motors and how the action of these motors affected the pitch and roll angle of the ant model. The pitch motor rotated the arm about the vertical axis of the tank, which corresponds to the pitching axis of the model as it is mounted to the arm. The upper part of the arm was a hollow aluminium tube with two

steel push-pull rods descending through its interior. These rods were connected to the servo horn of the roll angle servo and to the forearm of the Robosting, allowing the model to be rotated about its local roll axis. Both servos were independently controlled using an Arduino (`http://www.arduino.cc`) microcontroller board and the `Servo.h` library provided in the standard Arduino library. The Arduino board received serial commands over USB in the form of pitch and roll commands, and output the appropriate control voltages to the servo motors to adjust their angles.

3.2.4 Data collection

The 3-D forces and moments acting on the model during a tow were measured with an ATI Nano17 (`http://www.ati-ia.com`) force transducer. The transducer was mounted between the Robosting and the model, thereby measuring the forces and torques exerted on the model over the course of a tow. As can be seen in Figure 3.2, the force transducer rotated with the entire model assembly, and the raw output from the force transducer was therefore relative to the local frame of reference of the ant — that is, the force transducer axes were aligned with the model orientation and not the direction of the incident flow. The force transducer was connected to a National Instruments PCI-6220 data acquisition (DAQ) card, with actual data acquisition tasks handled using the COMEDI library (`http://www.comedi.org/`) on the controlling Linux computer. Data samples over the course of a tow were obtained from the DAQ card at a sampling rate of 1000 Hz. The output received by the DAQ card was in the form of raw voltages measured across the strain gauges within the force transducer, and these were then converted into orthogonal components of force and torque in the local coordinate system of the transducer using the calibration matrix and C language SDK provided from the factory by ATI.

3.2.5 Model design and production

The physical model representing the ant was designed in a 3D modelling suite (Blender, Version 2.5, `http://www.blender.org`). To produce 3-D representations of the ant morphology, ant specimens preserved in alcohol were disassembled into individual pieces (head, trunk, gaster, and legs) and these pieces were photographed from a variety of angles using a dissecting microscope. These photographs were then imported directly into Blender and used as a background for the digital sculpting of a series of 3-D meshes representing the body parts of the ant. Measurements of the ant mesh were made to confirm that the relative sizes of the model components conformed to the morphometric measurements reported in Appendix B. The meshes were then modified so that the independent pieces terminated in tabs allowing for articulated connection of pieces, and an appropriately sized cutout with mounting holes was made in the trunk piece to allow for the attachment of the force transducer. Once the digital model was complete, the meshes of the individual pieces were exported as STL format files and printed in PA 2200 nylon material with a laser sintering 3-D printer by Shapeways (`http://www.shapeways.com`). The tabs holding the body parts together were joined with

a 0-80 bolt through the tab on one side connected to a corresponding 0-80 nut on the joining tab. The physical model was designed to have the same degrees of freedom as the joint angle model used to describe body posture in Chapter 2, with 21 adjustable joint angles in total. A series of photographs of the model used in this study is shown in Figure 3.3.

3.2.6 Control software

Custom control software was developed in Python to automate data collection from the tank. For a given posture and model, a suite of experiments was defined by selecting the range of angles in both pitch and roll that were to be tested (e.g. -50° to +70° in 5° increments) and the range of towing speeds to be tested (e.g. 0.5 m/s to 1.8 m/s, in 0.1 m/s increments). Once the suite of desired experiments had been defined, the control software automatically ran through the experiments in a randomized order, storing the forces and moments in each experiment in an individual file tagged with the pitch, roll and speed of that particular experiment. For the range of speeds required to simulate the dynamics of a gliding *C. atratus* ant, a settling time of 15 s between experiments was sufficiently long to ensure that a given experiment did not detectably affect the forces and moments measured in the subsequent experiment.

Prior to each experiment, the model was moved into position for the tow by the pitch and roll servos, and the background force exerted on the force transducer by the model due to gravity was measured. This measurement was used to remove gravity from the readings of the force transducer so that the forces measured during the tow related exclusively to the fluid forces acting on the model.

3.2.7 Tested postures

Three postures were tested based on observed postures in Chapter 2: 1) a "stable gliding" posture, 2) a "pitching" posture, and 3) a "turning" posture. The joint angles comprising these postures are tabulated in Table 3.1.

The stable gliding posture is shown in Figure 3.4, and is characterized by the extension of all legs above the body axis and the slight flexion of the gaster under the body.

The stable gliding posture is modified by moving the hind-legs forward and increasing the angle of flexion of the gaster to produce a pitching posture, which was observed to cause the whole body of the ant to pitch upward.

The turning posture tested here focuses on the effect of asymmetries in the fore-aft motion of the mid- and hind-legs, which was observed to be correlated with changes in yaw heading. The head, petiole and gaster angles are kept the same as for the gliding posture, but the mid- and hind-leg coxae are rotated anteriorly and posteriorly on the right and left sides, respectively, as shown in Figure 3.6.

To illuminate how these postures improve the stability of the ant, I ran tests on a dorsoventrally flattened body posture, referred to here as the "pancake" posture (Figure 3.7).

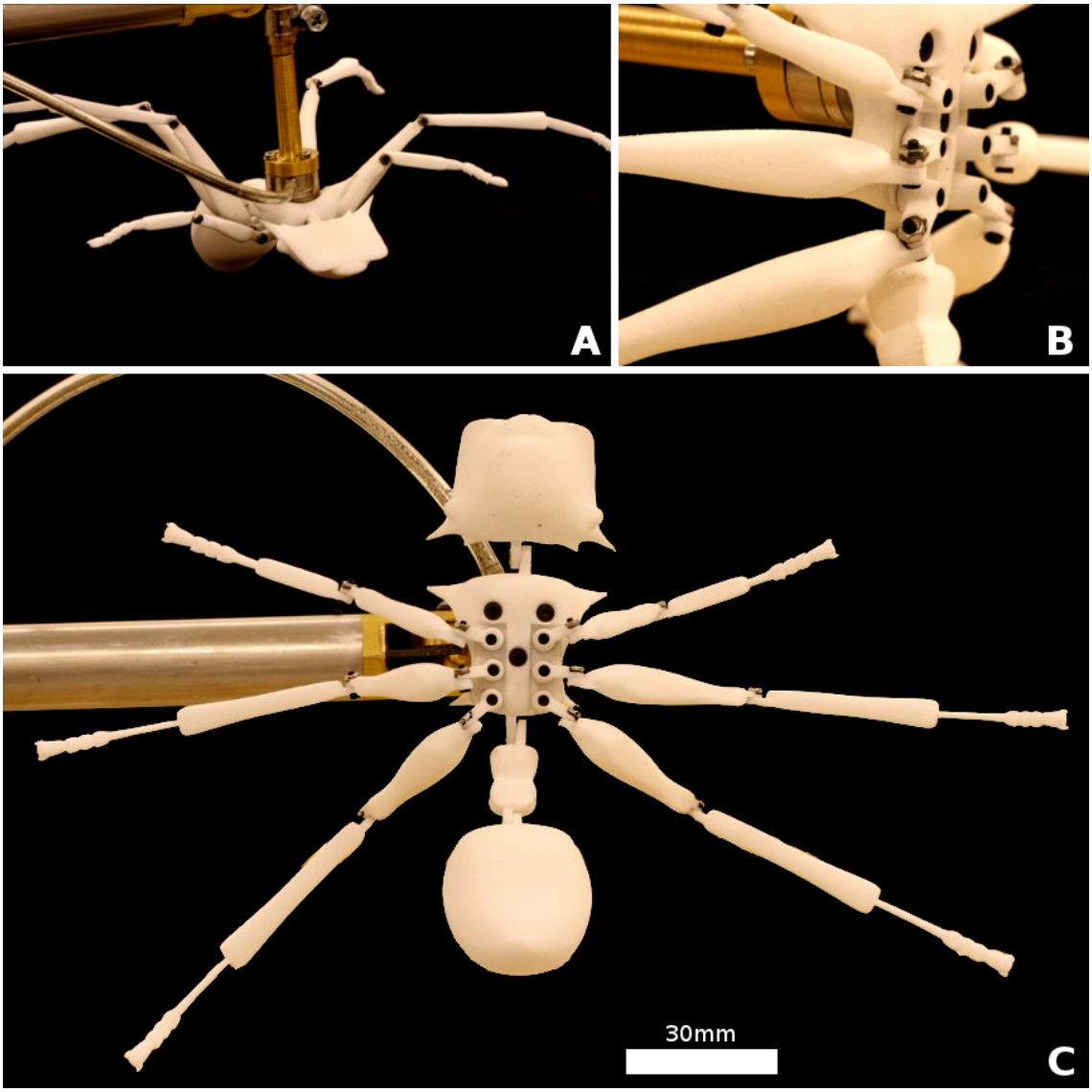

Figure 3.3: Model of ant used in experiments, showing articulation of joints and mounting of force transducer to Robosting.

	Gliding	Pitching	Turning	Pancake	Stumpy
Head	-15	-30	-15	0	-15
Petiole	20	-20	20	0	20
Gaster	-30	-65	-30	0	-30
RFC	50	50	50	20	50
RFF	30	30	30	0	30
RFT	0	0	0	0	0
RMC	-10	5	10	0	-10
RMF	45	45	45	0	NA
RMT	20	20	20	0	45
RHC	-50	-20	-15	-20	-50
RHF	65	65	65	0	NA
RHT	35	35	35	0	50
LFC	50	50	50	20	50
LFF	30	30	30	0	30
LFT	0	0	0	0	0
LMC	-10	5	-10	0	-10
LMF	45	45	45	0	NA
LMT	20	20	20	0	45
LHC	-50	-20	-70	-20	-50
LHF	65	65	65	0	NA
LHT	35	35	35	0	50

Table 3.1: Joint angles used in experiments. All values are expressed in degrees. Leg angles are referred to using a code of the form ABC, where A is a member of [L, R], denoting left or right; B is a member of [F, M, H], denoting fore-, mid-, or hind-leg; and C is a member of [C, F, T], denoting coxa, femur or tibia. The coxae angles represent the fore-aft angle of the leg orientation, where positive angles indicate an anterior position of the leg, and negative angles indicate a posterior position. All other angles are dorso-ventral angles, where positive angles represent elevated postures.

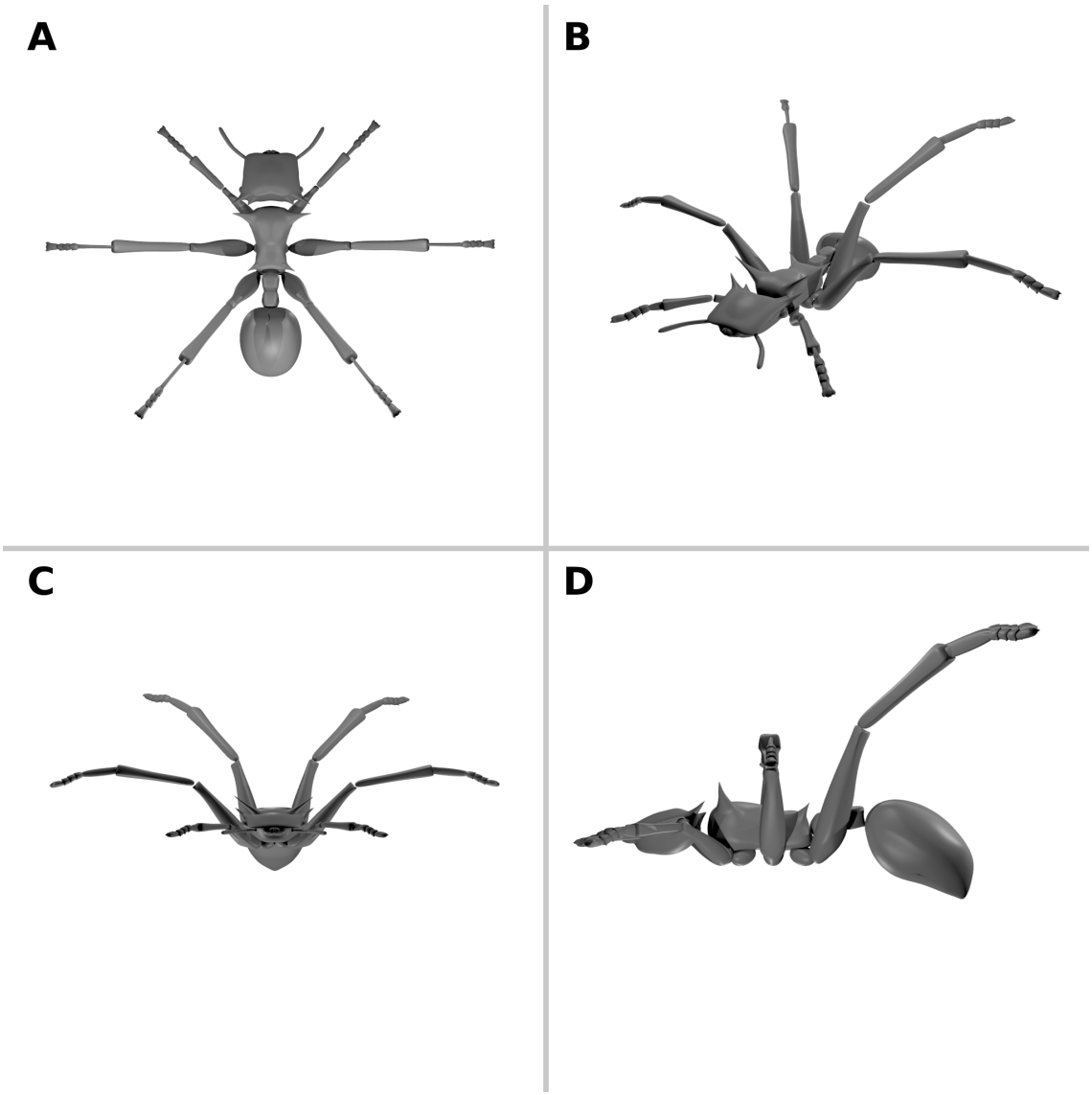

Figure 3.4: Render of computer model of ant in stable gliding posture. **A:** Top view. **B:** Perspective view. **C:** Front view. **D:** Side view.

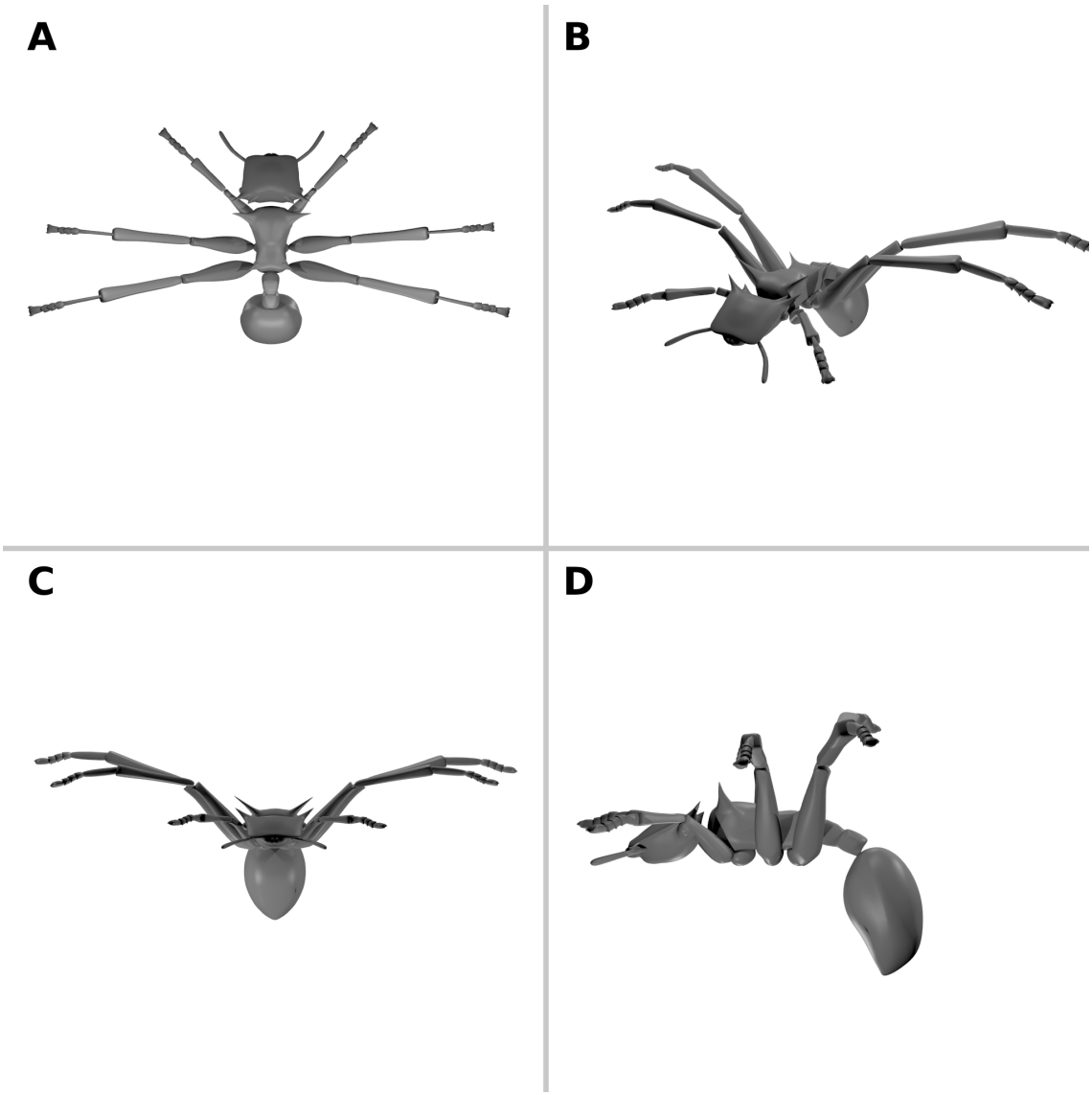

Figure 3.5: Render of computer model of ant in pitching posture. **A:** Top view. **B:** Perspective view. **C:** Front view. **D:** Side view.

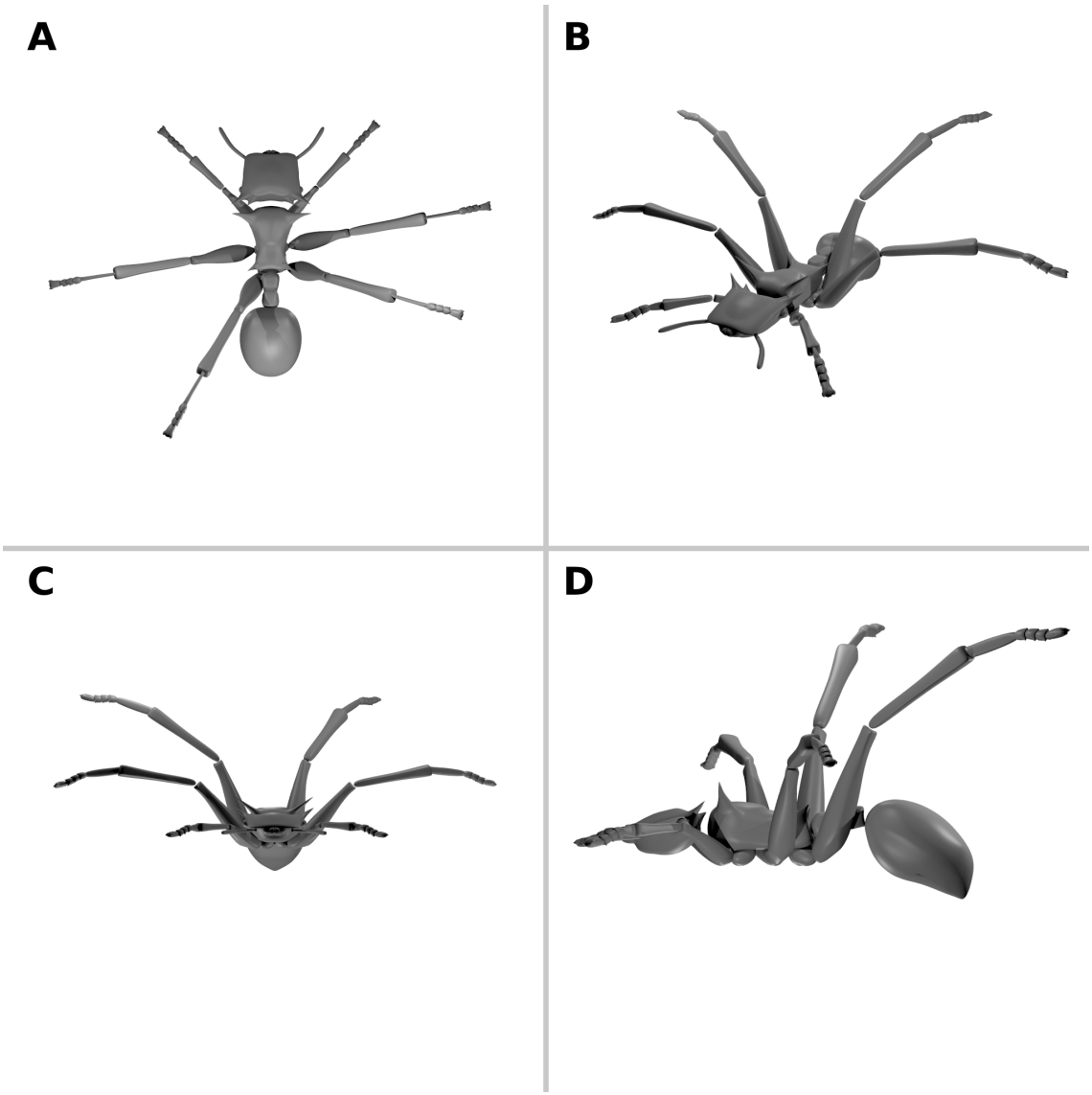

Figure 3.6: Render of computer model of ant in turning posture. **A:** Top view. **B:** Perspective view. **C:** Front view. **D:** Side view.

In this posture, all legs are held horizontally outstretched, and the head and gaster dorsoventral flexion angles are set to zero. It is important to note that this is not a posture based on observations made on real animals, but it is certainly a posture that they could potentially employ if they chose to.

Finally, in an effort to understand how leg length affects stability and gliding performance, I removed the mid- and hind-leg femurs from the model, attaching the mid- and hind-leg tibia directly to the coxa joints. This posture, referred to here as the "stumpy posture" (Figure 3.8), drastically shortens the mid- and hind-legs. Aside from the lack of mid- and hind-leg femurs, the posture was designed to be as similar as possible to the gliding posture, so that a reasonable comparison between the two could be made.

3.2.8 Data processing

3.2.8.1 Tabulation of data

For each tow, the time series data for each of the components of force and torque were trimmed to include only the section of the tow during which the model was being towed at a constant velocity equal to the velocity specified for that experiment (i.e. the forces and moments acting on the model as it was accelerated and decelerated at the beginning and end of the tow were not considered). Means and standard deviations of the forces and moments were computed for the steady state section and tabulated along with the tow speed, pitch angle, and roll angle.

3.2.8.2 Data transformation

The raw data obtained from the force transducer represented the forces and moments acting on the force transducer relative to the local axes of the transducer itself. To be able to compare the forces and moments experienced by the ant in different orientations of pitch and roll, it was necessary to transform the raw data from the transducer into the forces and moments acting on the ant at its center of mass, within a coordinate system aligned with the direction of the incident flow.

The center of mass of the ant was computed using a custom Python script running within Blender, relying on morphometric data for *C. atratus* (see Appendix B). The morphometric data include separate measurements of mass for the head, trunk, gaster and legs, each of which are assumed to be of uniform density for the purposes of estimating the location of the center of mass. A virtual armature controlling the joint angles of a *C. atratus* model in Blender is used to represent a given posture, and the center of mass of each body part is computed as the geometric center of the mesh representing it. Finally, the center of mass of the entire ant mesh is computed as the mean of these geometric centers, weighted according to the fractional contribution of the body part to the total mass.

Once the location of the center had been determined, the forces and moments measured at the transducer were used to calculate the aerodynamic forces and moments acting at the

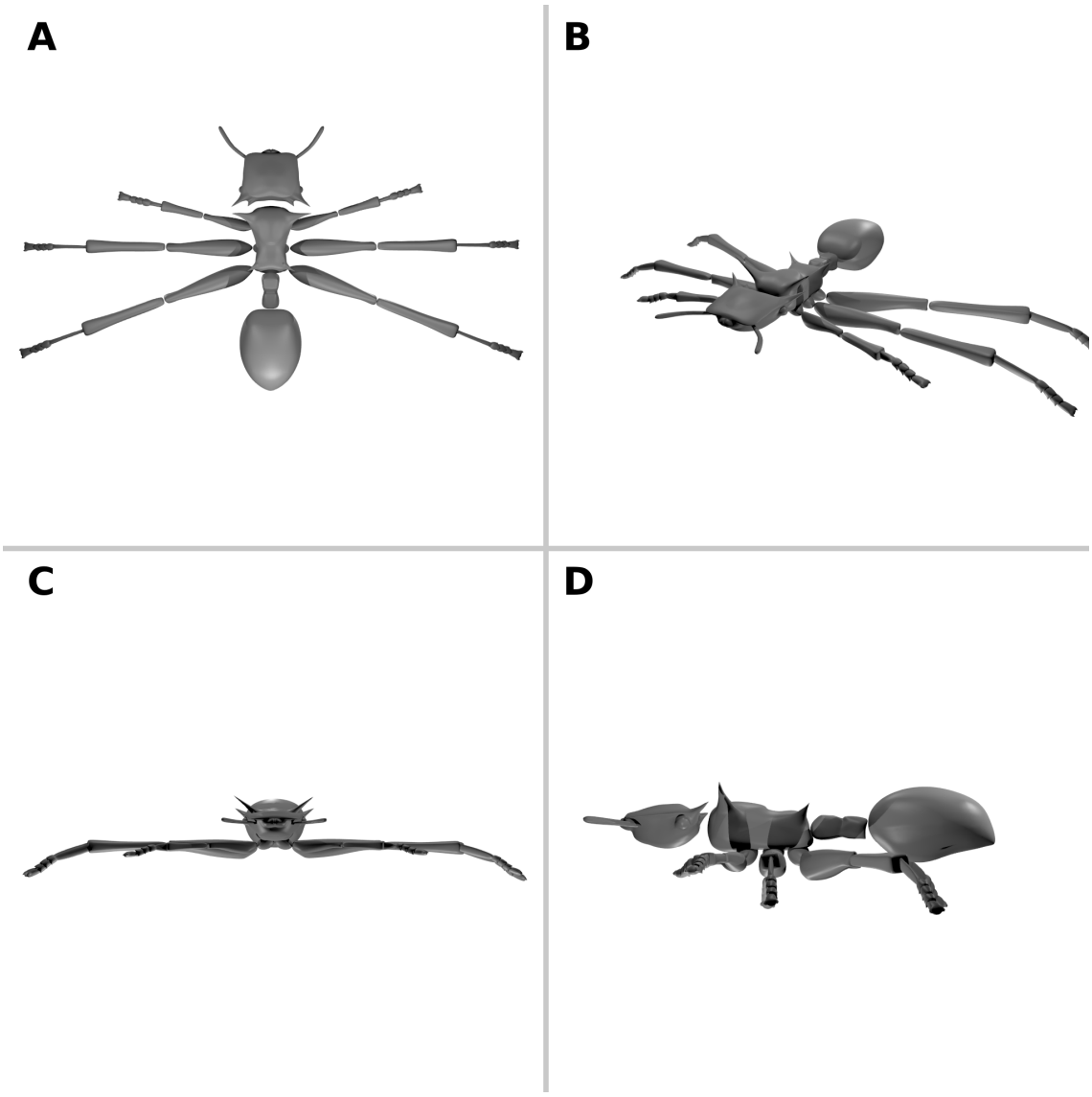

Figure 3.7: Render of computer model of ant in pancake posture. **A:** Top view. **B:** Perspective view. **C:** Front view. **D:** Side view.

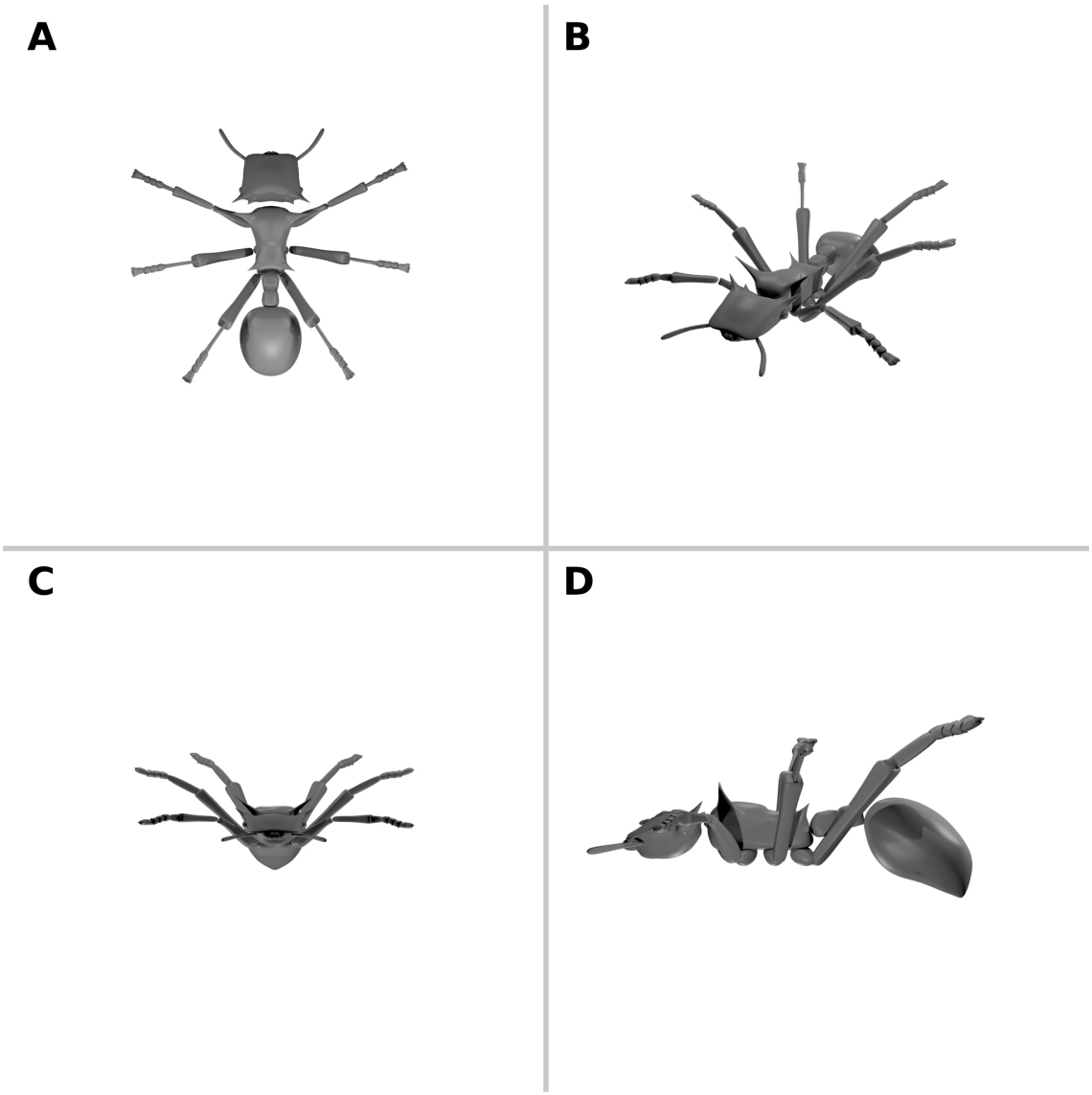

Figure 3.8: Render of computer model of ant in stumpy posture. **A:** Top view. **B:** Perspective view. **C:** Front view. **D:** Side view.

center of mass. The translation of the forces was trivial, as the frame of reference local to the center of mass is non-accelerating during the steady-state phase of the tow: the forces measured at the location of the force transducer must be equal to the forces exerted at the center of mass. To translate the moments from the force transducer mounting location to the location of the center of mass, it was necessary to add a component of torque due to the moment arm between the center of mass and the transducer mount, such that

$$\boldsymbol{\tau}_{\mathrm{CM}} = \boldsymbol{\tau}_{\mathrm{FT}} - \mathbf{r} \times \mathbf{F} \tag{3.1}$$

where $\boldsymbol{\tau}_{\mathrm{CM}}$ is the vector torque exerted about the center of mass, $\boldsymbol{\tau}_{\mathrm{FT}}$ is the vector torque measured by the force transducer, $\mathbf{r}$, is the vector between the center of mass and the transducer mounting, and $\mathbf{F}$ is the vector force measured by the force transducer.

Finally, once the moments at the center of mass had been calculated, it was necessary to rotate the coordinate system of the forces and moments from the local force transducer coordinate system to a coordinate system aligned with the flow. This was accomplished by by calculating the inverse rotation matrices for the pitch and roll angles of each experiment and applying these matrices to the measured data, thereby rotating the measured data into a coordinate system aligned with the tank coordinate system.

3.2.8.3 Forces and stability

Once all processing was complete, the result was six three-dimensional data arrays containing the three components of force and torque along the shared axes of pitch angle, roll angle, and tow speed. To investigate the dynamics of a posture as held by a real ant it is important to note that, for an ant of a given mass m, the terminal velocity of an ant shape is not expected to be constant with respect to its pitch and roll angle (assuming that the projected area of the ant as experienced by the oncoming flow changes with pitch and roll angle). It was therefore necessary to probe the dataset to find a subset of the array containing the expected dynamics of a falling ant of a specified mass m. This process was accomplished by first defining the mass of interest (e.g. 30 mg, a typical mid-range worker mass (Yanoviak et al., 2005)), and noting that the gravitational force acting on the real ant is therefore approximately 0.3 mN. The force amplification factor provided by switching from air to mineral oil (see Section 3.2.1) is 1.04×10^5, so the fluid force that would counterbalance a simulated 30 mg ant falling in equilibrium measured in the tow tank would be 3.06 N. It is unlikely that, for every available combination of pitch and roll, the tow tank was run at a speed yielding a net force exactly equal to this value, and so interpolation of the available data was required. For every orientation angle of pitch and roll, the three components of force and torque were plotted as a function of tow speed. Cubic smoothing splines were fit to each component of force and torque using the Scipy function `interpolate.splrep` (`http://www.scipy.org`). Least squares optimization (using the Scipy function `optimize.leastsq`) was then used in concert with the spline evaluation function `interpolate.splev`) to determine the tow speed at which the magnitude of the force vector (using the three interpolated force component splines) was equal to the expected gravitational force on an ant of the specified mass. A

new matrix was then produced containing the forces and torques relevant to the specified ant mass at all available pitch and roll angles, using these interpolated values.

Once this matrix had been produced for an ant of specified mass m, the forces and moments acting on the ant at any combination of pitch and roll angle could be determined. The first question asked for a given ant and posture was whether or not a fixed point existed, where a fixed point is defined as a pitch and roll orientation where the net aerodynamic torque acting on the ant is zero. That is, as long as the ant remains at the fixed point, it will not experience an aerodynamic torque altering its orientation. The follow-up question, assuming that at least one fixed point exists, is whether or not that fixed point is stable. A stable fixed point is one where perturbations away from the fixed point result in the ant experiencing a correcting moment, whereby the torque acts in opposition to the original perturbation and returns the ant to the fixed point. For example, consider an ant at a fixed point that experiences an external perturbation that causes it to pitch upward (increasing pitch angle). If the fixed point is stable, the aerodynamic torque acting on the ant at its new orientation after the perturbation has acted must be negative to counteract the action of the perturbation.

Conversely, if the fixed point is unstable, perturbations away from the fixed point will be intensified through positive feedback. For example, if an ant at an unstable fixed point is perturbed so as to pitch upward, the moment it will experience at this new pitch angle will cause it to continue to pitch upward, away from the fixed point.

In a single dimension, stability plots are typically plotted as shown in Figure 3.9, where the aerodynamic moment is plotted as a function of heading angle (e.g. pitching moment as a function of pitch angle). The sign and slope of the relationship between angle and moment determines the stability of the fixed point, assuming that it exists: a positive slope indicates an unstable fixed point, a negative slope indicates a stable fixed point, and the magnitude of the slope indicates how stable or unstable the fixed point is.

The notion of stability can be extended to higher dimensions, as shown in Figure 3.10. Here moments are plotted as a function of two orthogonal angles, and arrows indicate the magnitude and direction of those moments. Note that in higher dimensions, it is possible to have saddle points, whereby a restoring moment exists on one axis and a divergent moment exists on the other. This type of fixed point is classified as unstable.

For the data obtained in this study, stability was plotted in the form shown in Figure 3.10, where the angles α_1 and α_2 are the pitch and roll angles, respectively. A second plot, also on axes of pitch and roll, was generated to show the fore-aft and lateral forces exerted on the animal as a function of pitch and roll.

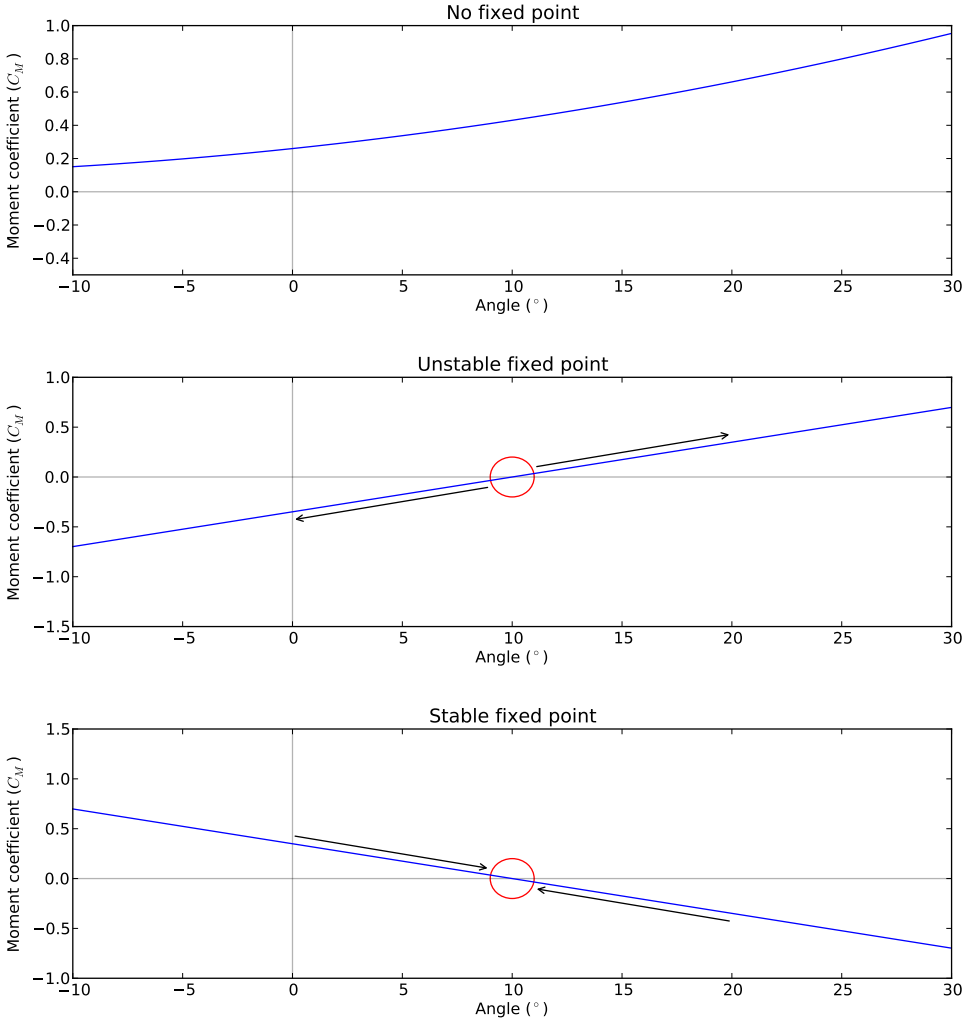

Figure 3.9: Plots showing variation of moment coefficient with angle. **Top:** No fixed point exists. **Middle:** Unstable fixed point at $x = 10$. Perturbations away from the fixed point lead to moments of equal sign to the perturbation, thereby exacerbating the perturbation. **Bottom:** Stable fixed point at $x = 10$. Perturbations away from the fixed point result in exerted moments of opposite sign to the perturbation, restoring the system to the fixed point.

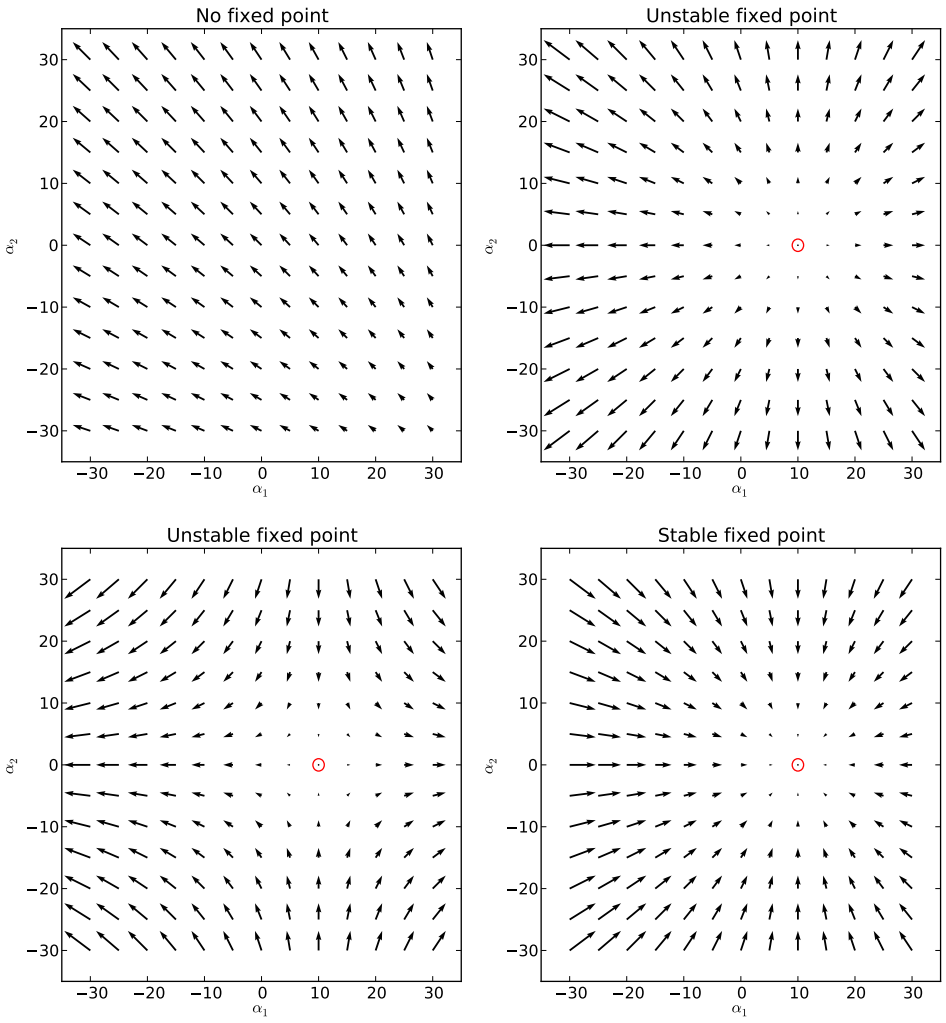

Figure 3.10: Quiver plots demonstrating moments as a function of two orthogonal angles α_1 and α_2. **Top Left:** No fixed point in observed range. **Top Right:** Unstable fixed point at (10,0). **Bottom Left:** Unstable fixed point, saddle type, at (10,0). **Bottom Right:** Stable fixed point at (10,0).

3.3 Results

3.3.1 Example tow data

Figure 3.11 shows the forces and moments measured by the force transducer over the course of a single tow with fixed pitch and roll angle. As expected, the forces and moments are initially zero and begin to increase in magnitude as the cart is accelerated from rest. Once the cart reaches its prescribed tow speed, the acceleration halts and the forces and moments level out for the steady state section of the tow. As the cart reaches the end of the tank, the cart is decelerated to a stop, with a consequent reduction in force and torque magnitude.

3.3.2 Stable gliding posture

The stable gliding posture was tested over a range of $[-50°, +70°]$ in pitch and $[-15°, +15°]$ in roll at 5° intervals, over a range of tow speeds from 0.5 to 1.4 m/s in 0.1 m/s intervals (Reynolds number range ∼1000-3000). There are 1925 possible combinations of these values, all of which were tested in the suite of experiments. Each suite of experiments, furthermore, was repeated 5 times to ensure repeatability of the results. For each experiment, 300-500 samples (equivalent to 0.3-0.5 s at 1000 Hz) were taken from the steady state section of the tow, and the mean and standard deviation of these sample were recorded into a table of raw values. These raw values were then transformed as described in the Section 3.2.8.2 into the forces and moments about the center of mass of the ant. Figure 3.12 shows a single slice through the resulting dataset, where variation in the forces and moments acting at the center of mass of an ant in gliding posture is shown as function of changing pitch angle, with roll angle and tow speed held constant. Note that this slice shows the variation of forces and moments that were exerted on the model, not the variation of forces and moments that would act on a real ant of a fixed mass: the net magnitude of the aerodynamic force, which must be equal and opposite to the fixed gravitational force acting on the body of the ant at equilibrium, is clearly not constant over the range of pitch angles shown.

As described in Section 3.2.8.3, the aerodynamic forces and torques exerted on an ant of fixed mass were estimated by calculating an interpolated tow speed for each pitch and roll angle such that the magnitude of the aerodynamic force at that speed was equal to the gravitational force acting on the mass of the ant. These results were put into a new data array representing the simulated forces and moments acting on an ant of fixed mass. Figure 3.13 shows one such data set as a pair of quiver plots of the non-drag components (i.e. orthogonal to the direction of the incident flow) of the aerodynamic force and the torques about the pitch and roll axes, respectively. In this plot we see that the magnitude and direction of the non-drag forces change as a function of pitch and roll angle, and that the torques experienced by the ant are stabilizing in both pitch and roll.

The force and moment data presented in Figure 3.13 are shown again in Figure 3.14. Here the two quiver plots from Figure 3.13 are combined on a single field of pitch and roll angles; the torques acting on the ant are plotted as contours, and the forces are plotted as

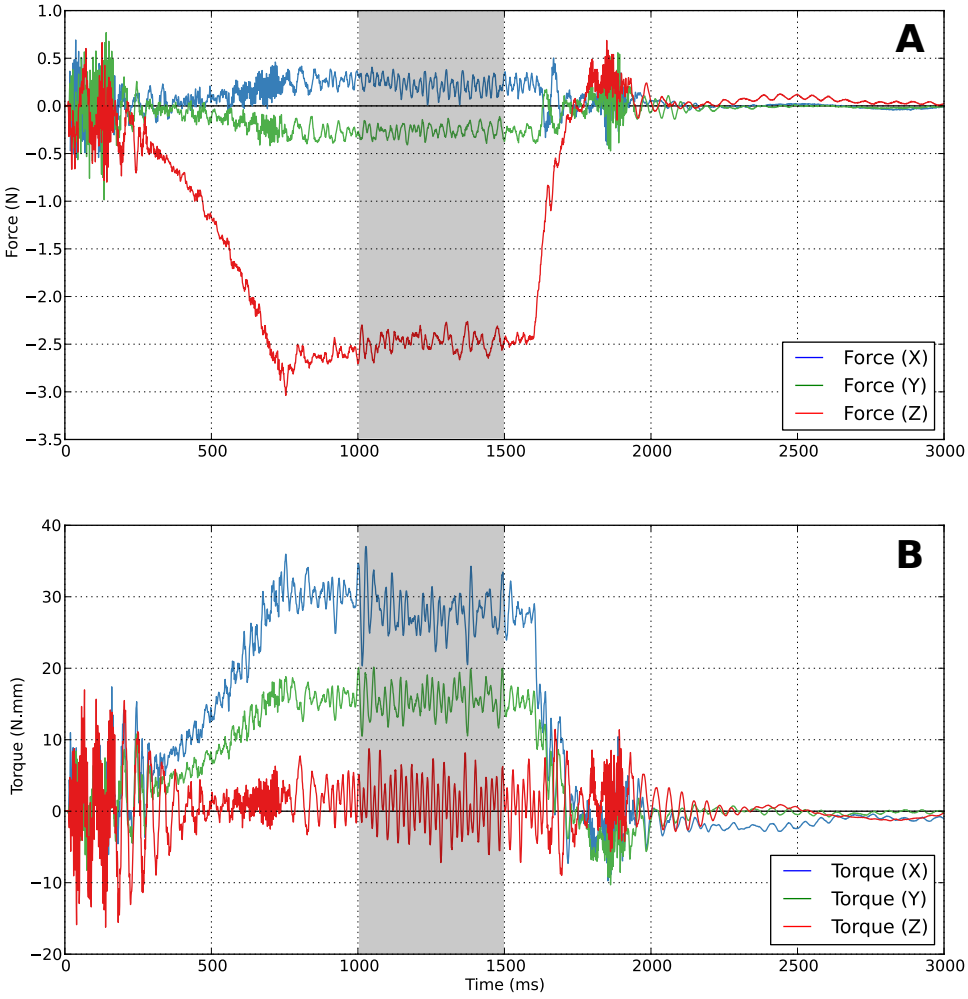

Figure 3.11: Forces and moments measured on a *C. atratus* model in gliding posture at a pitch angle of 15°, a roll angle of 0°, and tow speed of 1.1 m/s. Note that the XYZ coordinate system used here is local to the orientation of the force transducer and is not aligned with the incident flow. The steady state section used for further analysis occurs from 1000-1500 ms.

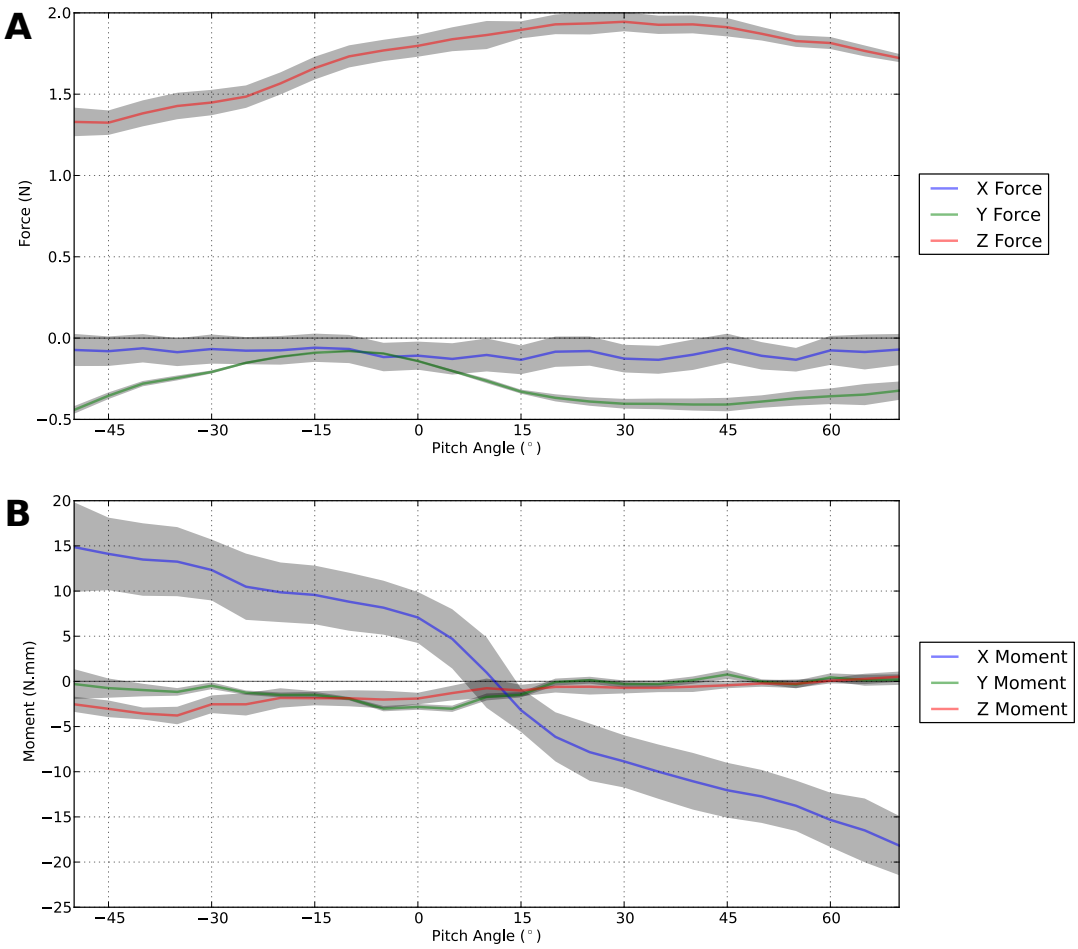

Figure 3.12: Forces and moments as a function of pitch angle, with roll angle fixed at 0° and tow speed fixed at 1.0 m/s. Forces and moments about orthogonal axes are represented with different colors, and standard deviations are represented by a grey area surrounding each line.

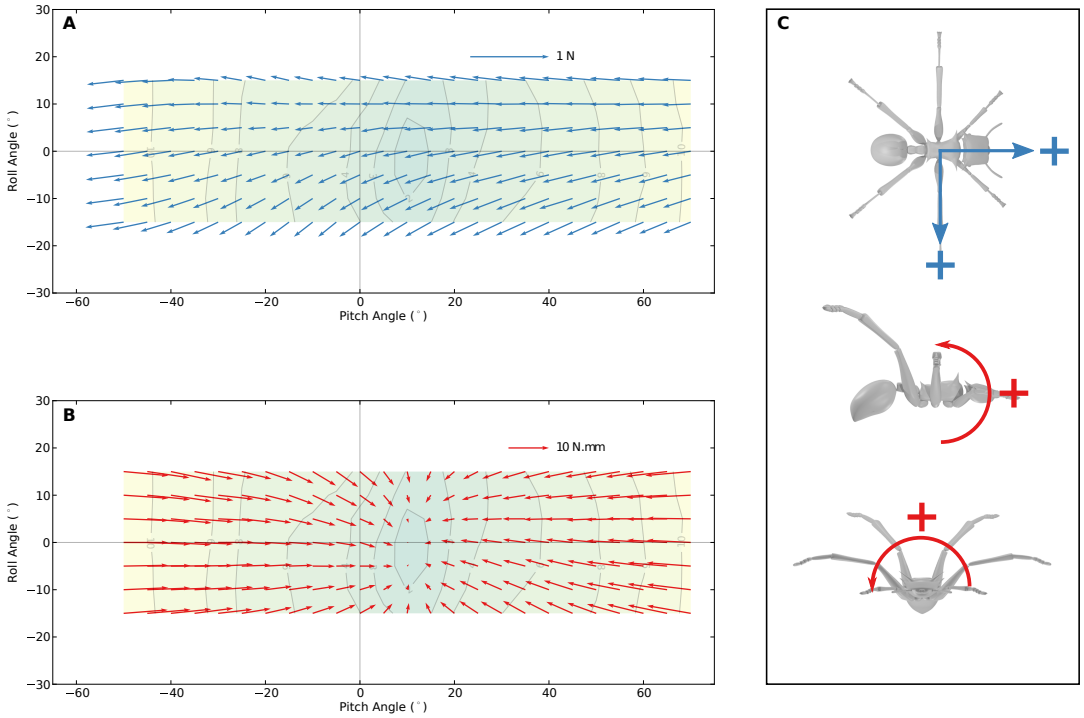

Figure 3.13: Quiver plots of forces and moments exerted on a 25 mg *C. atratus* ant in gliding posture (see Fig 3.4) plotted against pitch and roll angle. **A:** Non-drag forces plotted as arrows over a field of pitch and roll angle. The magnitude of the arrows along the x-axis indicates the fore-aft force exerted on the ant, and the magnitude along the y-axis indicates the sideways force. **B:** Aerodynamic torque plotted as arrows over a field of pitch and roll angle. The x-component of the vector represents the pitching torque, and the y-component represents the rolling torque.

vectors as in Figure 3.13. Figure 3.14 also provides a representation of how the terminal velocity of the ant changes as a function of pitch and roll angle — as the projected area of the ant decreases at high angles of pitch and roll, the speed at which the aerodynamic forces balance the gravitational force increases.

3.3.3 Size-dependent effects, or lack thereof

Figure 3.15 shows the moments, forces and terminal velocities for a 10 mg ant, representing a smaller *C. atratus* worker ant. Changes in the coefficients of lift and drag with the decrease in Reynolds number between a 25 mg ant and a simulated 15 mg ant could potentially alter the stable orientation of the ant as well as the lift and drag forces exerted on the ant at its stable fixed point. However, no such changes were observed — a range of ant masses from 8 mg to 25 mg were simulated for the gliding posture, and a linear regression analysis revealed no statistically significant trend in either the change in angle of the stable orientation or the lift-to-drag ratio as a function of simulated mass. A qualitative comparison of the contours and vectors plotted in Figures 3.14 and 3.15 reinforces this finding; the contours and vector fields are largely indistinguishable with regard to their shape. The only significant differences between these plots are the absolute magnitudes of the moments exerted on the model and the estimated terminal velocity of the simulated ant, as is to be expected.

3.3.4 Pitching posture

In Figure 3.16, the forces and moment contours for the pitching posture (see Table 3.1 and Figure 3.5) are illustrated over a range of $[0°, +70°]$ in pitch and $[-15°, +15°]$ in roll. Compared to the gliding posture shown in Figure 3.14, the location of the stable fixed point has moved from $(12.7°, 1.2°)$ to $(23.7°, 6.8°)$, and the lift-to-drag ratio has increased from 0.32 to 0.39.

Superficially, the variation in direction and magnitude of the lift-to-drag vectors appears similar between Figures 3.14 and 3.16, and it is reasonable to question whether the aerodynamic characteristics of the gliding and pitching postures are essentially equivalent, with the change in location of the stable fixed point being due to the change in location of the center of mass caused by the change in posture. This turns out to not be the case: if the location of the center of mass of the pitching posture is used to calculate the force surface for the data obtained from the model in the gliding posture, the location of the stable fixed point moves to $(-3.7°, -4.6°)$ and the lift-to-drag ratio is reduced to 0.28.

3.3.5 Turning posture

The forces and moment contours for the turning posture (ref. Table 3.1, Figure 3.6) are shown in Figure 3.17. Compared to the gliding posture (Figure 3.14, the stable orientation has shifted from $(12.7°, 1.2°)$ to $(25.6°, -15°)$, and the lift-to-drag ratio has increased from 0.32 to 0.45. The substantially higher lift-to-drag ratio observed in this case is due to the

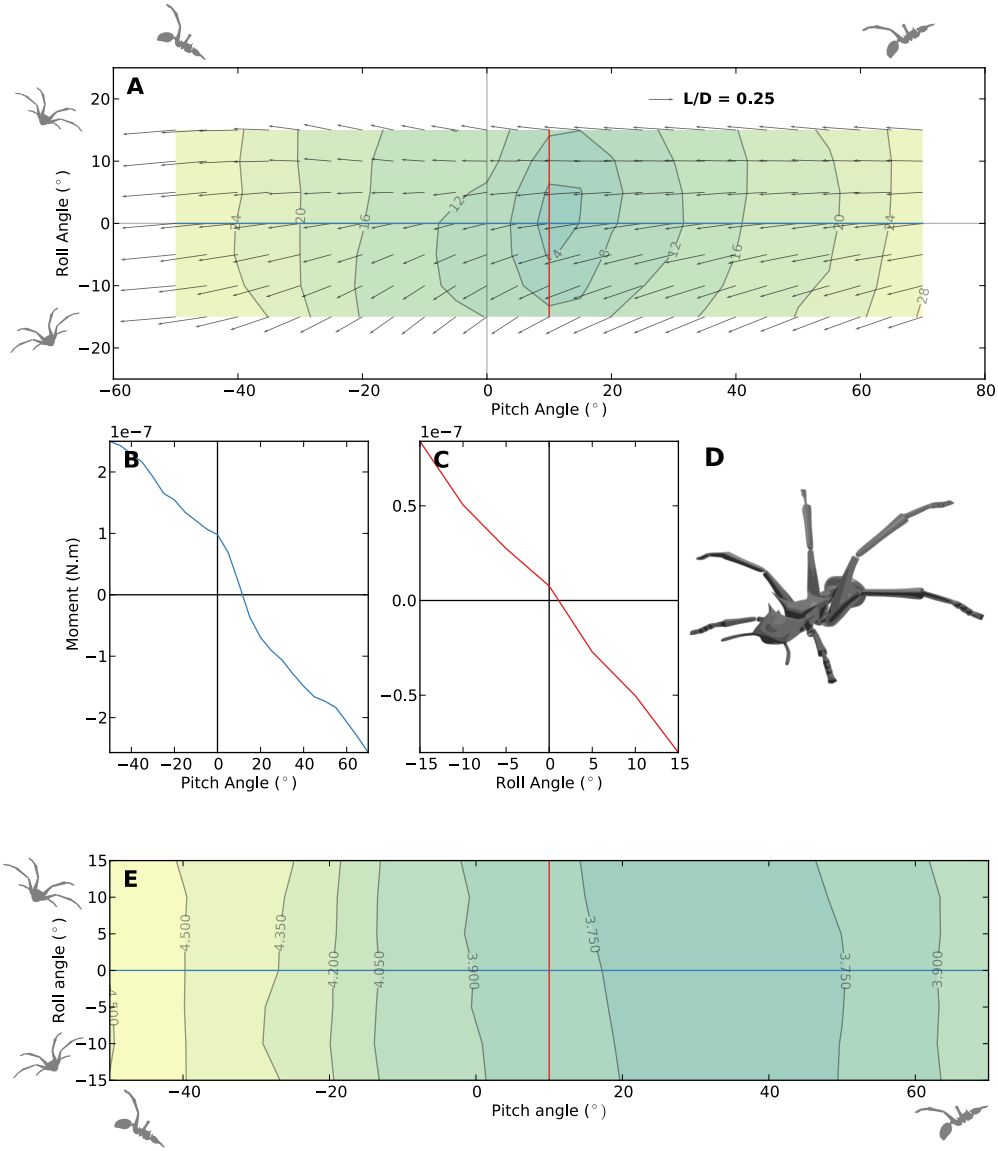

Figure 3.14: **A:** Lift as a function of pitch and roll angles, normalized to the drag force at that orientation to produce a lift-to-drag ratio. The vectors are plotted on top of a contour representation of the net aerodynamic torque acting on the ant. **B & C:** Slices through dataset showing stability of fixed point $(12.7°, 1.2°)$ in pitch and roll, respectively. **D:** Render of gliding posture. **E:** Contour plot of equilibrium glide velocity as a function of orientation.

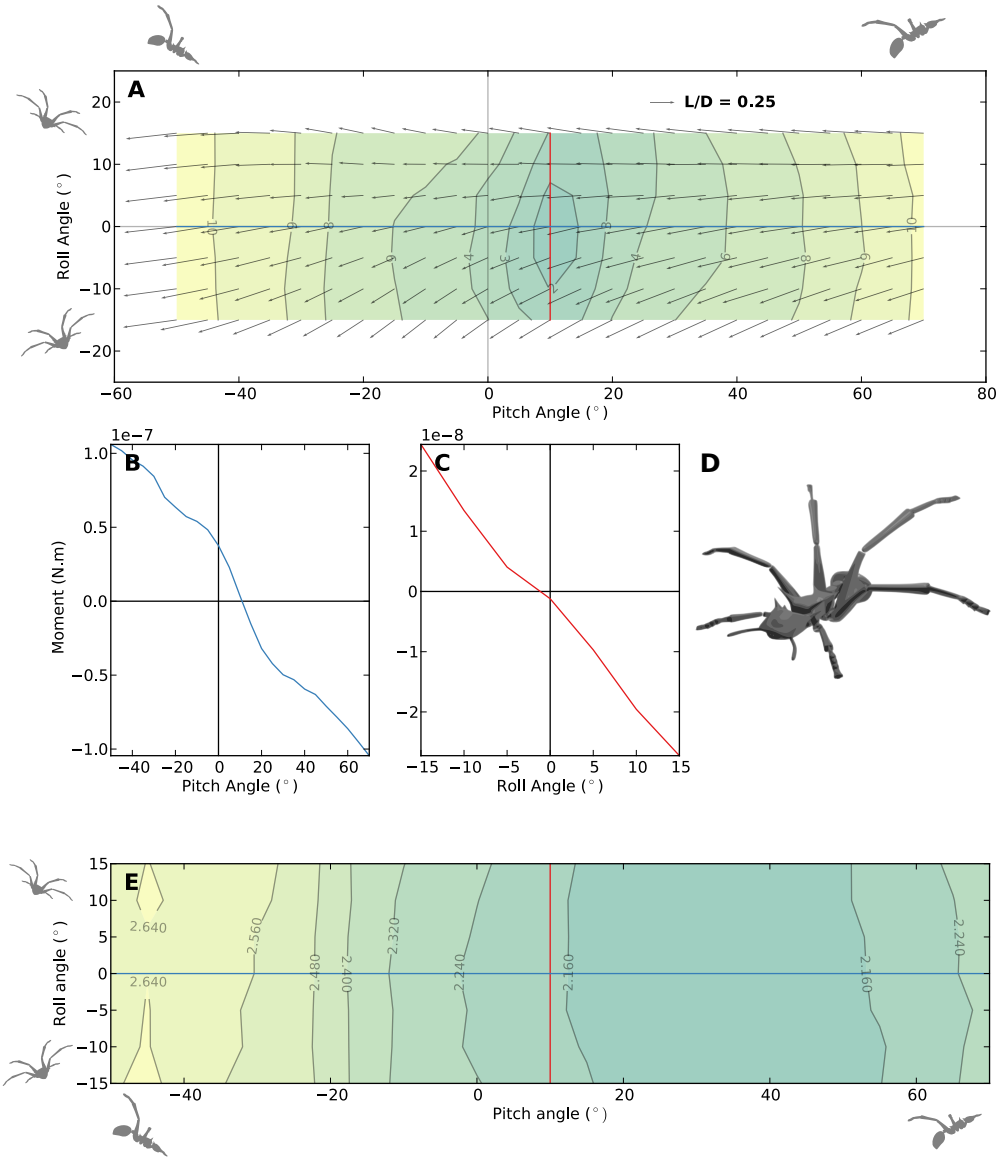

Figure 3.15: **A:** Lift-to-drag quiver plot over moment contours for a 10 mg *C. atratus* ant in gliding posture. **B&C:** Pitch and roll moment plots at fixed point, showing stability of posture. **D:** Render of gliding posture. **E:** Contour plot of equilibrium glide velocity as a function of orientation angle.

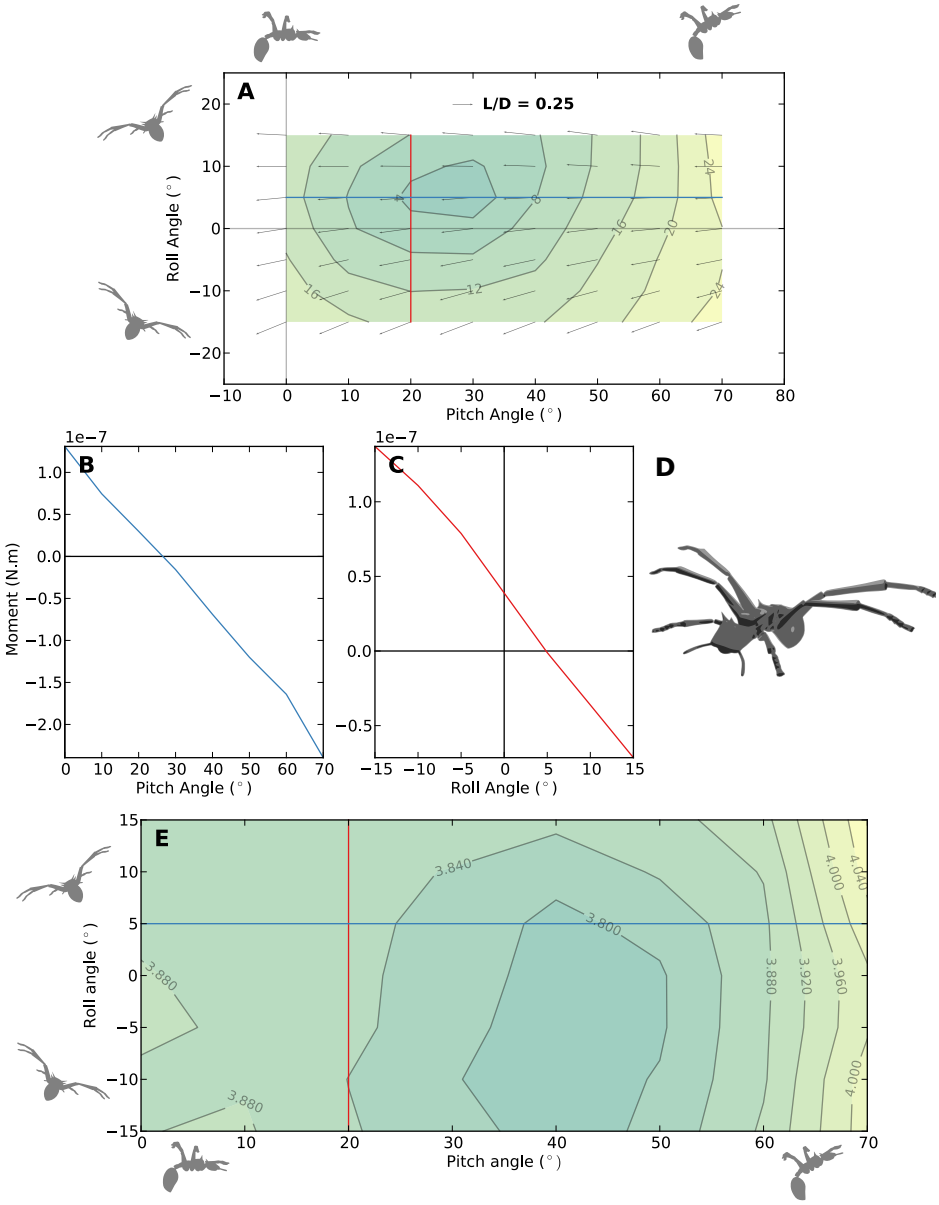

Figure 3.16: **A:** Lift-to-drag quiver plot over moment contours for a 25 mg *C. atratus* ant in pitching posture. **B&C:** Pitch and roll moment plots at fixed point $(23.7°, 6.8°)$, showing stability of posture. **D:** Render of pitching posture. **E:** Contour plot of equilibrium glide velocity as a function of orientation angle.

	Pitch (°)	Roll (°)	L/D ratio
Gliding	12.7	1.2	0.32
Pitching	23.7	6.8	0.39
Turning	25.6	-15	0.45
Pancake	-5.8	5.5	0.25
Stumpy	NA	NA	NA

Table 3.2: Summary of stable orientations for postures in this study, along with lift-to-drag ratios at that stable orientation.

large increase in the sideways force achieved in the turning posture, which has increased from 0.049 to 0.21 as a relative decimal fraction of the drag force. The estimated aerodynamic forces that would act on an ant in this posture would cause a counter-clockwise turn, which is consistent with expectations based on the analysis of wind tunnel postures and maneuvers in Chapter 2.

3.3.6 Pancake posture

As noted in Section 3.2.7, the pancake posture (ref. Table 3.1, Figure 3.7) is not based on any posture observed as being used by gliding *C. atratus* ants. The forces and moment contours of this posture, shown in Figure 3.18, show that this splayed and dorso-ventrally flattened posture is marginally stable about a fixed point at $(-5.8°, +5.5°)$, with a lift-to-drag ratio at this stable point of 0.25.

3.3.7 Stumpy posture

The stumpy posture, described in Section 3.2.7, was designed to investigate how leg length contributes to stability for a gliding *C. atratus* ant. The forces and moment contours shown for this posture in Figure 3.19 do not indicate the presence of a stable fixed point over the range of pitch and roll angles tested. The aerodynamic forces exerted on the ant are highly dependent on orientation, but the magnitude of the aerodynamic moment on the ant over the range of tested angles tends to be smaller than observed for the gliding posture for the morphology with full-sized legs.

3.3.8 Summary of results

The stable orientations and corresponding lift-to-drag ratios of the various postures tested in this study are summarized in Table 3.2.

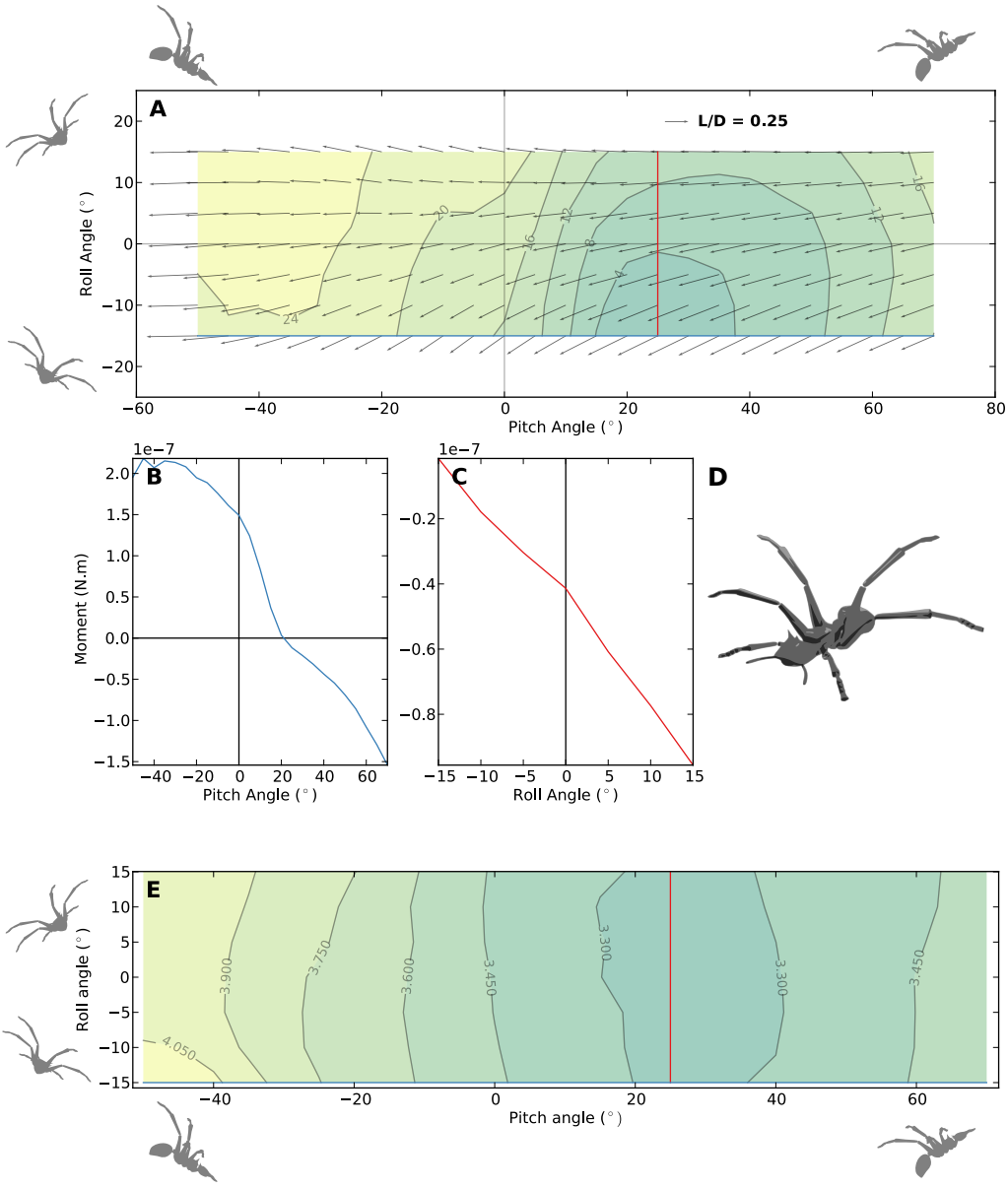

Figure 3.17: **A:** Lift-to-drag quiver plot over moment contours for a 20 mg *C. atratus* ant in turning posture. **B&C:** Pitch and roll moment plots at fixed point $(25.6°, -15°)$, showing stability of posture. **D:** Render of turning posture. **E:** Contour plot of equilibrium glide velocity as a function of orientation angle.

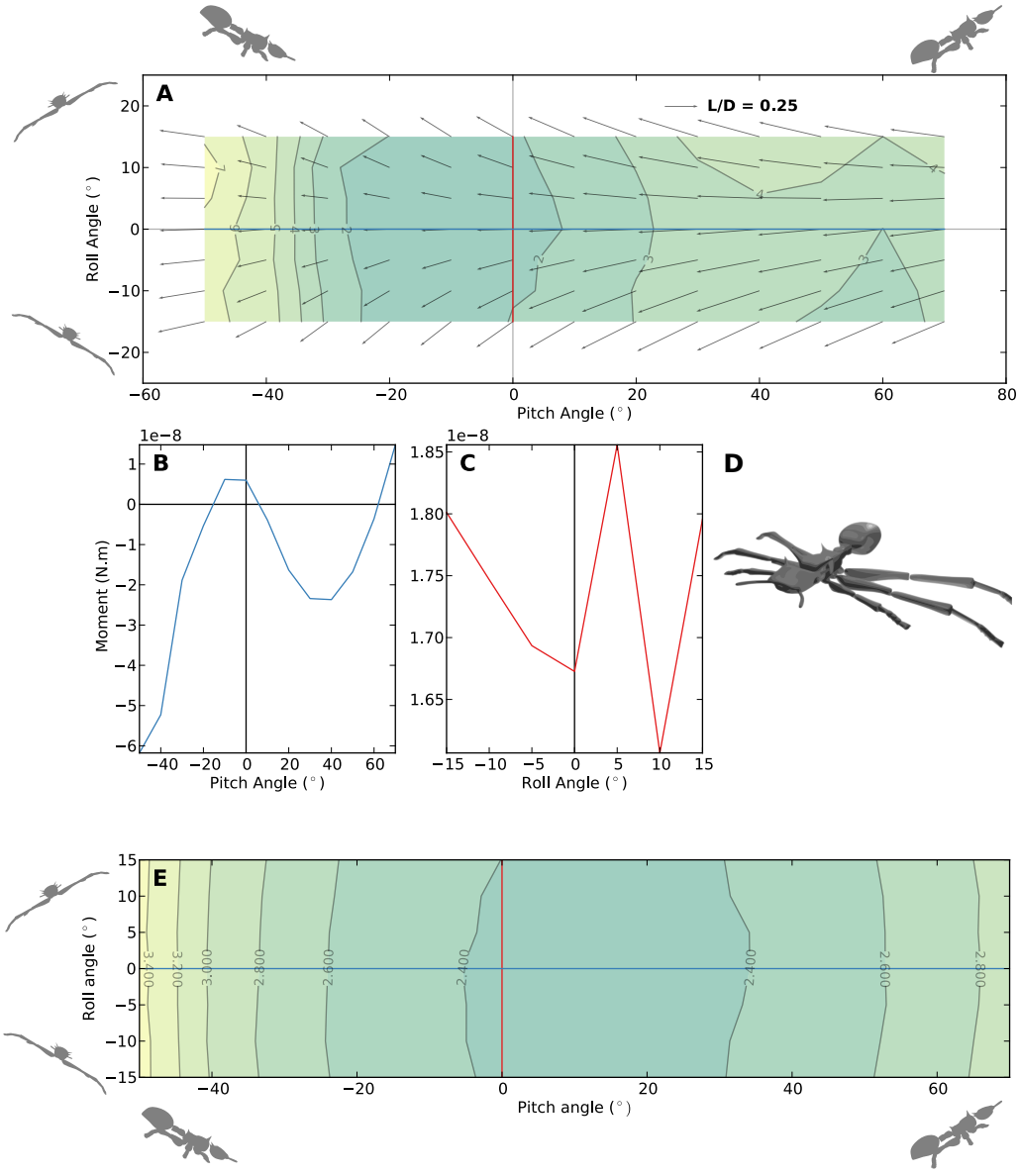

Figure 3.18: **A:** Lift-to-drag quiver plot over moment contours for a 15 mg *C. atratus* ant in pancake posture. **B&C:** Pitch and roll moment plots at $(0°, 0°)$. The pancake posture is marginally stable over a small range of pitch angles, but unstable in roll. **D:** Render of pancake posture. **E:** Contour plot of equilibrium glide velocity as a function of orientation angle.

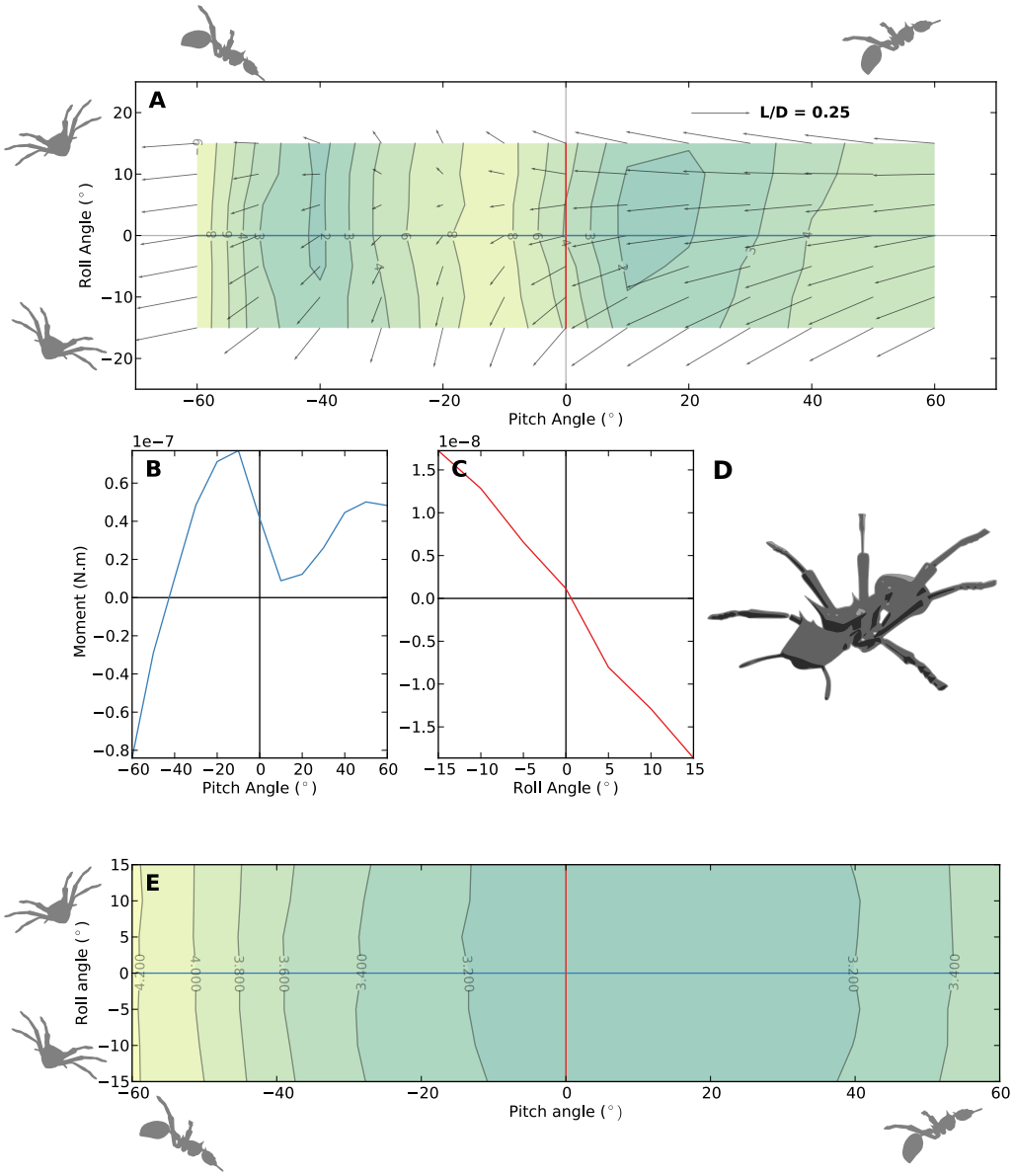

Figure 3.19: **A:** Lift-to-drag quiver plot over moment contours for a 15 mg ant in stumpy posture. **B&C:** Pitch and roll moment plots at $(0°, 0°)$. The stumpy posture is stable in roll, but unstable in pitch. **D:** Render of stumpy posture. **E:** Contour plot of equilibrium glide velocity as a function of orientation angle.

3.4 Discussion

3.4.1 Passive stability in gliding posture

A key result of the moment contours shown for all of the postures based on observations from prior wind tunnel work (Figures 3.14, 3.16, and 3.17) is that each of these postures has a passively stable fixed point. This result means that for small perturbations about the pitch and/or roll axes, no active control is required for the ant to recover from those perturbations and return to its stable orientation. Furthermore, this simplifies the strategy that a falling ant must employ in order to right itself before beginning a bout of gliding. Larger animals (e.g. geckos (Jusufi et al., 2008), among many others) must typically execute some form of axial twisting maneuver to orient their ventral surface downward when dropped in an upside-down posture. In contrast, *C. atratus* simply needs to adopt its typical gliding posture with the legs elevated above the anteroposterior axis and the passively stable nature of this posture will automatically right the falling ant.

The lift-to-drag ratios measured for the gliding posture (≈ 0.3 at the stable fixed point, according the force surface shown in Figure 3.14) match well with the lift-to-drag ratios measured from trajectories of actual gliding ants in Chapter 1, and the pitch and roll angles of the stable fixed point orientation $(12.7^\circ, 1.2^\circ)$ match well with the postures I measured in Chapter 2. This result gives some reasonable degree of confidence that the simulations performed in this study are capturing the dynamics of real-world performance in gliding *C. atratus* ants.

3.4.2 Pitching and turning maneuvers

In Chapter 2, it was hypothesized that symmetric changes in the fore-aft posture of the legs and flexion of the gaster could be used by a *C. atratus* ant to perform pitching maneuvers, and that asymmetric leg postures could be used to perform turns. A kinematic analysis of the postures employed by gliding *C. atratus* ants in a vertical wind tunnel showed that *C. atratus* varies fore-aft leg posture during gliding (exhibiting both symmetric and asymmetric changes in the fore-aft angles of leg pairs) and also varies gaster flexion angle. These observations were used to develop the maneuvering postures (i.e. pitching and turning) used in this study.

The results of the physical simulation of the dynamics of these maneuvers show that *C. atratus* ants are able to effect large, controllable changes in both their stable orientation angle and the aerodynamic forces acting upon them at that stable angle. Compared to the gliding posture, the pitching posture increases the stable pitch angle by 11° and increases the lift-to-drag ratio of the ant by 22%.

The turning posture, which is identical to the gliding posture except for the coxae angles of the mid- and hind-legs, caused a significant change in both pitch and roll orientation, moving the stable orientation angle from $(12.7^\circ, 1.2^\circ)$ for the stable gliding pose to $(25.6^\circ, -15^\circ)$ for the turning pose. Fore-aft forces and sideways forces both increased by factors of 1.3 and 4.1, respectively. This combined change in pitch and roll orientation at the stable fixed

point, along with the increase in both fore-aft and sideways forces, shows that the ants turn using a banked turning maneuver (as opposed to a "crabbed" turn, *sensu* McCay (2001), in which changes in yaw heading are accomplished through the generation of a yaw moment while keeping all other forces and moments approximately equal).

3.4.3 Size effects

Field studies on gliding *C. atratus* ants have shown that larger individuals exhibit a lower glide index than smaller individuals (Yanoviak et al., 2005), meaning that for the same point of release a larger *C. atratus* ant will land lower on a target tree trunk than a smaller *C. atratus* ant. One hypothesis that could explain this phenomenon would be that lift-to-drag ratio for a *C. atratus* shape decreases with increasing Reynolds number, which would cause the glide angle for larger *C. atratus* workers to decrease relative to smaller *C. atratus* workers.

Comparison of simulated ants in gliding posture over a range of body masses from 10 mg to 25 mg revealed no significant trends in either the change in location of the stable fixed point or the lift-to-drag ratio of the ant at that stable fixed point. However, it is important to note that this assumes that leg length in *C. atratus* scales isometrically with body size — that is, using the same model at different Reynolds numbers implies an assumption that the leg length relative to body size is constant over the 10-25 mg range of *C. atratus* masses. A morphometric analysis of 21 *C. atratus* worker ants (Appendix B) provides preliminary evidence that leg length scales allometrically with body mass by the relationship $L \propto M^{\sim\frac{1}{4}}$, rather than $L \propto M^{\frac{1}{3}}$ as would be expected if leg length scaled isometrically.

3.4.4 Comparing gliding posture to splayed posture

In the wind tunnel study documented in Chapter 2, all tested ants immediately raised their legs above the anteroposterior axis when dropped into the working section of the wind tunnel. The effect of this postural change on the aerodynamic stability of the falling ant is marked, as can be seen by comparing the moment contours of the gliding posture (Figure 3.14) with those of the pancake posture (Figure 3.18). While the pancake posture is marginally stable, with a fixed point at $(-5.8°, +5.5°)$, a perturbing moment applied to the ant model of 5 N.mm is sufficient to push the model to any orientation from $[-35°, +70°]$ in pitch and $[-15°, +15°]$ in roll. Over that range, the ant experiences large changes in both the magnitude and the direction of the non-drag forces acting upon its body. For the gliding posture, that same perturbing moment would cause a maximum deviation from the stable fixed point of $\pm 10°$ in pitch and roll, with only minor changes in the aerodynamic forces experienced by the ant.

This means that for an ant gliding in a turbulent air environment (where small perturbations may be assumed to be present) the aerodynamic forces on the ant are controllable when the ant is in its stable gliding posture, and would not be controllable if the ant were to employ the pancake posture.

3.4.5 Leg length and stability

The stumpy posture (ref. Table 3.1 and Figure 3.8) is an approximation of the gliding posture for a model missing the femurs of its mid- and hind-legs (i.e. with the tibiae connected directly to the coxae). This effective shortening of the mid- and hind-legs has profound effects on the aerodynamic stability of the ant, as can be seen from the moment contours for the stumpy posture shown in Figure 3.19. There is no stable fixed point for this posture over the range of orientations tested, and very low magnitude perturbations are sufficient to cause drastic changes in both the orientation of the ant and the aerodynamic forces exerted on the ant. This result demonstrates conclusively that over the range of Reynolds numbers tested in this study, leg length is a key morphological feature in enabling controllability of aerodynamic forces during gliding.

Following this result, it is reasonable to question whether the long legs found in *C. atratus* ants are adapted for gliding performance; this is probably not the case. Long legs are commonly found in diverse species of canopy specialist ants and ants that forage in canopy environments, including many species of ants that do not exhibit directed aerial descent behavior (Yanoviak et al., 2005, 2011). Long legs are assumed to improve the ability to walk on rough bark surfaces in an arboreal environment; clearly the legs are maintaining their primary functionality for *C. atratus*, but this adaptation for canopy navigation is being co-opted (*sensu* Gould and Vrba (1982)) for aerodynamic control in directed aerial descent.

3.4.6 Future work

This study is perhaps the most exhaustive analysis of the aerodynamics of full-body stability and control in a gliding animal, and the methods I have outlined here open a path for a diverse array of potential follow-up experiments. Of highest priority is application of these methods in experiments to measure aerodynamic stability and control in ancestrally wingless insects, such as bristletails and silverfish. The current analysis of gliding in wingless worker ants tells us little about the origins of insect flight, on account of worker ants being highly morphologically derived and secondarily wingless insects. Now that gliding has been observed in extant bristletails (Yanoviak et al., 2009), it would be highly illuminating to perform tow-tank experiments like those described here on dynamically scaled models of gliding bristletails to characterize their aerodynamic stability and lift-to-drag performance. A long-standing theory regarding the evolutionary pathway by which insect wings evolved holds that proto-wing structures in the ancestral lineage of the modern winged insects were used for gliding prior to their being exapted for powered forward flight. It would be informative to investigate the dynamics of gliding in extant bristletails using the model-based approach described here, and then test the aerodynamic effects of adding proto-wing structures to the model to determine whether or not these structures contribute favourably to gliding performance.

References

R. M. Alexander. *Principles of Animal Locomotion*. Princeton University Press, 2003.

E. A. Arbas. Control of hindlimb posture by wind-sensitive hairs and antennae during locust flight. *Journal of Comparative Physiology A*, 159:849–857, 1986.

J. B. Barlow, W. H. Rae, and A. Pope. *Low-speed wind tunnel testing*. Wiley-Interscience, 3rd edition, 1999.

J. M. Camhi. Sensory control of abdomen posture in flying locusts. *Journal of Experimental Biology*, 52:533–537, 1970.

I. M. Cohen and P. K. Kundu. *Fluid Mechanics*. Academic Press, 3rd edition, 2004.

S. A. Combes and R. Dudley. Turbulence-driven instabilities limit insect flight performance. *Proceedings of the National Academy of Sciences*, 106(22):9105–9108, 2009.

M. H. Dickinson and K. G. Götz. Unsteady aerodynamic performance of model wings and low reynolds number. *The Journal of Experimental Biology*, 174:45–64, 1993.

M. H. Dickinson, F.-O. Lehmann, and S. P. Sane. Wing rotation and the aerodynamic basis of insect flight. *Science*, 284(5422):1954–1960, June 1999.

R. Dudley. *The Biomechanics of Insect Flight*. Princeton University Press, 2000.

C. P. Ellington. Aerodynamics and the origin of insect flight. *Advances in Insect Physiology*, 23:171–210, 1991.

S. B. Emerson and M. A. R. Koehl. The interaction of behavioral and morphological change in the evolution of a novel locomotor type: "flying" frogs. *Evolution*, 44(8):1931–1946, 1990.

S. B. Emerson, J. Travis, and M. A. R. Koehl. Functional complexes and additivity in performance: A test case with "flying" frogs. *Evolution*, 44(8):2153–2157, 1990.

B. Etkin and L. D. Reid. *Dynamics of flight: stability and control*. John Wiley & Sons, Inc., 1996.

J. W. Flower. On the origin of flight in insects. *Journal of Insect Physiology*, 10:81–88, 1964.

S. J. Gould and E. S. Vrba. Exaptation — a missing term in the science of form. *Paleobiology*, 8(1):4–15, 1982. ISSN 00948373. doi: 10.2307/2400563. URL `http://dx.doi.org/10.2307/2400563`.

R. Hartley and A. Zisserman. *Multiple View Geometry in Computer Vision*. Cambridge University Press, 2 edition, 2004. ISBN 0521540518.

A. J. Hinterwirth and T. L. Daniel. Antennae in the hawkmoth *Manduca sexta* (Lepidoptera, Sphingidae) mediate abdominal flexion in response to mechanical stimuli. *Journal of Comparative Physiology A*, 196:947–956, 2010.

J. Jepson. *The tree climber's companion: a reference and training manual for professional tree climbers*. Beaver Tree Pub., 2000.

A. Jusufi, D. I. Goldman, S. Revzen, and R. J. Full. Active tails enhance arboreal acrobatics in geckos. *Proceedings of the National Academy of Sciences*, 105:4215–4219, 2008.

J. G. Kingsolver and M. A. R. Koehl. Selective factors in the evolution of insect wings: response to Kukalová-Peck. *Canadian Journal of Zoology*, 67:785–787, 1989.

J. G. Kingsolver and M. A. R. Koehl. Selective factors in the evolution of insect wings. *Annual Reviews of Entomology*, 39:425–451, 1994.

E. Leigh. *Tropical Forest Ecology: A view from Barro Colorado Island*. Oxford University Press, 1999.

S. R. Madigosky and I. Vatnick. Microclimatic characteristics of a primary tropical Amazonian rain forest, ACEER, Iquitos, Peru. *Selbyana*, 21:165–172, 2000.

M. G. McCay. Aerodynamic stability and maneuverability of the gliding frog *Polypedates dennysi*. *Journal of Experimental Biology*, 204(16):2817–2826, 2001.

R. D. Mehta and P. Bradshaw. Design rules for small low speed wind tunnels. *Aeronautical Journal*, page 443:449, 1979.

G. K. Taylor. Mechanics and aerodynamics of insect flight control. *Biological Reviews*, 76: 449–471, 2001.

A. L. R. Thomas and G. K. Taylor. Animal flight dynamics i. stability in gliding flight. *Journal of Theoretical Biology*, 212:399–424, 2001.

S. Vogel. *Life in Moving Fluids*. Princeton University Press, 1994.

S. P. Yanoviak and R. Dudley. The role of visual cues in directed aerial descent of *Cephalotes atratus* workers (Hymenoptera: Formicidae). *The Journal of Experimental Biology*, 209: 1777–1783, 2006.

S. P. Yanoviak, R. Dudley, and M. Kaspari. Directed aerial descent in canopy ants. *Nature*, 433:624–626, 2005.

S. P. Yanoviak, M. Kaspari, and R. Dudley. Gliding hexapods and the origins of insect aerial behaviour. *Biology Letters*, Mar. 2009. doi: 10.1098/rsbl.2009.0029. URL `http://dx.doi.org/10.1098/rsbl.2009.0029`.

S. P. Yanoviak, Y. Munk, M. Kaspari, and R. Dudley. Aerial manoeuvrability in wingless gliding ants (*Cephalotes atratus*). *Proceedings of the Royal Society B: Biological Sciences*, 277(1691):2199–2204, July 2010. doi: 10.1098/rspb.2010.0170. URL `http://dx.doi.org/10.1098/rspb.2010.0170`.

S. P. Yanoviak, Y. Munk, and R. Dudley. Evolution and ecology of directed aerial descent in arboreal ants. *Integrative and Comparative Biology*, May 2011. doi: 10.1093/icb/icr006. URL `http://dx.doi.org/10.1093/icb/icr006`.

J. M. Zanker. How does lateral abdomen deflection contribute to flight control of *Drosophila melanogaster*? *J Comp Physiol A*, 162:581–588, 1988.

Appendix A

Dynamic similarity in fluid dynamics experiments

In the tow tank experiments described in this thesis, the dynamics of gliding in ants are simulated by measuring the forces exerted on a geometrically similar model of an ant towed through mineral oil. In this appendix, I will explain some of the concepts that make this simulation possible.

A.1 Reynolds number

Please note at the outset that this will necessarily be a brief treatment of the subject, and that more detailed treatments of the subject may be found in elementary texts on fluid mechanics (e.g. Cohen and Kundu (2004)).

For an immersed body moving through a fluid at speeds much lower than the speed of sound in that fluid (such that compressibility effects may be comfortably ignored), the surrounding fluid exerts two separate forces on that moving body. One of these forces is inertial: that is, the fluid has mass and occupies the space that the object is moving into, and the object must exert a force on the fluid in order to accelerate that fluid out of the way. The second force is viscous: as the object moves through the fluid, there is a no-slip condition that states that there is a very thin layer of fluid stuck to the outer edge of the object. As the object moves through the fluid, the layer of fluid immediately next to the surface of the object, which travels with the object, must shear past the adjacent layers of fluid. This shearing of fluid is resisted due to the viscosity of the fluid; the higher the fluid viscosity, the greater the tendency of the layers of fluid to resist shearing and the greater the force is that is required to move an object through that fluid.

The Reynolds number is a useful concept in fluid dynamics that represents the ratio, or relative importance, of the inertial forces to the viscous forces in a fluids problem. For an object moving through a fluid, if the Reynolds number is high, the forces exerted on that object are predominantly due to the intertial forces. As an example, a hand extended from

a moving car on the highway experiences a significant drag force from the apparent wind, and this drag force is overwhelmingly due to the inertial forces acting on the hand due to the air, with a comparatively miniscule component deriving from the viscous forces.

As a counter example, a ball bearing dropped into a jar of honey will sink very slowly. The force that resists the tendency of gravity to act on the ball bearing is predominantly viscous forces within the honey, not inertial forces — honey is no denser than water, and so in the absence of the viscous forces a ball bearing might be expected to sink as rapidly in honey as it does in a jar of water.

The Reynolds number expresses this ratio of interial to viscous forces according to the following equation:

$$\mathrm{Re} = \frac{UL\rho}{\mu} \tag{A.1}$$

where Re is the Reynolds number, U is the velocity of the object as it moves through the fluid, L is some characteristic length of the object, ρ is the density of the fluid and μ is the dynamic viscosity of the fluid. Dimensional analysis shows that the Reynolds number is a dimensionless quantity.

From the perspective of one who wishes to simulate the flow around an object of a given shape, the Reynolds number is extraordinarily convenient. It essentially guarantees (with the aforementioned caveat that compressible effects are ignoreable) that as long as the Reynolds numbers are equal, the flow patterns around two geometrically similar objects will be identical, regardless of the manipulations that are done to the various parameters involved.

For example, in the case of gliding ants, I might wish to avoid constructing a model on the scale of an ant, and instead wish to use a geometrically similar model of an ant that was larger than a real ant by a factor of ten. If the real ant falls at 4 m/s, I can simulate the flow of air around a real ant using my larger model by reducing the flow speed of the air around the model to 0.4 m/s. Alternatively I could use a denser fluid, or a less viscous fluid — as long as the Reynolds number for the flow around my model ant matches that of the flow around the real ant.

A.2 Scaling forces

While Reynolds number similarity has given the convenience of being able to construct a model on any desired scale, measuring the forces exerted by the fluid on the model is still a very challenging prospect. The force exerted on an object moving through a fluid for reasonably high (i.e. inertially dominated) Reynolds number are given by the following equation:

$$F = 0.5\rho S U^2 \,\mathrm{C(Re)} \tag{A.2}$$

where F is the force, ρ is again the density of the fluid, S is a characteristic surface area of the object, U is the speed with which the object moves through the fluid, and C(Re) is a dimensionless non-linear function of the Reynolds number, often expressed with subscripts

as C_D and C_L to denote the coefficiencts of drag and lift, where drag forces are those forces that are aligned with the velocity vector U and lift forces are those forces that are orthogonal to U.

To continue our previous example of a model ant ten times larger than a real ant but moved ten times more slowly than a real ant through air to ensure dynamic similarity by Eqn. A.1, Eqn. A.2 shows us that the forces that we measure on the model of the ant will be equal to the forces exerted on the real ant. We have increased L in Eqn. A.1 by a factor of 10, which means that for our geometrically similar model ant the reference area in Eqn. A.2 has increased by a factor of 100. However, to maintain Reynolds number similarity, we had to reduce U by a factor of 10, which means that the U^2 term in Eqn. A.2 has been reduced by a factor of 100. The density of the fluid, ρ, has remained the same and, as the Reynolds number is the same, the non-linear force coefficient (being a function of the Reynolds number) has remained the same as well. Thus, by increasing the size of the model by a factor of 10 we have made the model easier to construct, but we are still faced with the prospect of having to measure forces of an equal magnitude to those experienced by the ant. This is problematic: a large ant might weigh 30 mg, and so at terminal velocity the fluid force experienced by the ant will be equal in magnitude to the gravitational force acting upon it — that is, $mg = 30 \times 10^{-6}\,\mathrm{kg} \times 9.8\,\mathrm{m.s^{-2}} \approx 3 \times 10^{-4}\,\mathrm{N}$. These sub-milli-Newton forces are very small, and would be impossible to measure using almost any off-the-shelf force transducers available.

A.3 Amplifying forces

All is not lost, however: we have so far only discussed modifications of the size (L) and speed (U) of the model and, as it turns out, linear amplifications of the forces exerted on the model by the fluid may be achieved by changing fluids. Looking again at Eqn. A.2, let us modify it slightly by exchanging the reference area S for aL^2, where L is the reference length from Eqn. A.1 and a is some constant (as long as geometric similarity is conserved, a will have the same value regardless of the value of L). Now Eqn. A.2 may be written as

$$\begin{aligned} F &= 0.5\rho S U^2\,\mathrm{C(Re)} \\ &= 0.5\rho a L^2 U^2\,\mathrm{C(Re)} \end{aligned}$$

Throwing out all of the coefficients and variables which remain constant assuming dynamic similarity, we get:

$$F \propto \rho(LU)^2 \tag{A.3}$$

If we manipulate Eqn. A.1 and substitute for LU in Eqn. A.3, we get

$$F \propto \rho\left(\frac{\mathrm{Re}\mu}{\rho}\right)^2 \tag{A.4}$$

Now consider the difference between the forces that we would measure on a real ant in air (assuming that were possible) and the forces that we could measure on a model of an ant

towed through, say, mineral oil. If we express Eqn. A.4 for both oil and air and take their ratio, we obtain the following expression:

$$\begin{aligned} F_{\text{oil}} &\propto \frac{\text{Re}^2 \mu_{\text{oil}}^2}{\rho_{\text{oil}}} \\ F_{\text{air}} &\propto \frac{\text{Re}^2 \mu_{\text{air}}^2}{\rho_{\text{air}}} \end{aligned}$$

Taking the ratio of these two equations, we get (finally):

$$\frac{F_{\text{oil}}}{F_{\text{air}}} = \frac{\mu_{\text{oil}}^2 \rho_{\text{air}}}{\mu_{\text{air}}^2 \rho_{\text{oil}}} \tag{A.5}$$

This is the amplification factor obtained by moving from air to oil. The fact that the Reynolds number is equal in both cases tells us that the relative importance of the inertial and viscous forces for both the real ant and the model are identical, and hence the fluid flow patterns around the real ant and the model ant should be identical as well. This manipulation of the fluid has allowed us to increase the magnitudes of both the inertial and the viscous forces so that higher forces are exerted by the fluid on the model while maintaining dynamic similarity.

For the oil used in the tank described in Chapter 3 of this thesis, the amplification factor is 10,400, which brings those previously mentioned sub-milli-Newton forces into the several-Newtons range, and makes those forces easily measureable with off-the-shelf force transducers.

One might reasonably ask why I did not use water instead of oil, and there is a very good reason for this. While the density of water is roughly three orders of magnitude greater than the density of air, its dynamic viscosity is lower by a factor of approximately 15 (see, e.g., Table 2.1 in Vogel (1994)), which would mean that by dragging a model of an ant through water I would have achieved a force amplification factor of just under 4, which is at best a mild improvement.

Appendix B

Morphometric scaling in *Cephalotes atratus* workers

B.1 Introduction

The dynamic scaling work in this thesis uses a single model of a *Cephalotes atratus* worker towed at a range of Reynolds numbers to investigate how body size influences the aerodynamics of skydiving. These data are relevant only if *C. atratus* scales approximately geometrically with mass, i.e. if small *C. atratus* workers are linearly scaled copies of larger *C. atratus* workers. In this appendix, I present morphometric data supporting this assumption.

B.2 Data collection

Morphometric data was collected from 21 *C. atratus* workers collected on Barro Colorado Island in Panama in 2007. Live workers were anesthetized in a cold room ($-15°C$) for 10 minutes and then dissected using fine scissors and tweezers. Masses of individual body parts were measured with a Mettler-Toledo balance accurate to 10^{-4} g. Digital photographs of all body parts were taken of all body parts using a Canon Powershot SD300 digital camera held against the eye-piece of a dissecting microscope, with millimeter graph paper placed underneath the body parts for calibration. Photographs were obtained from a variety of orthogonal angles to facilitate measurements of length, width and depth, which were performed in ImageJ.

B.3 Tables of Measurements

For convenience of fitting the data to the printed page, the morphometric data presented here has been split into three tables. Table B.1 collects all of the measurements of masses

obtained for the 21 ant workers measured, in mg. Table B.2 collects the length, width and depth measurements of the head, trunk and gaster, in mm. Table B.3 collects the leg length measurements in mm.

Ant ID	Total	Head	Gaster	Trunk+Legs	RH	RM	RF	LH	LM	LF	Trunk
1	42.7	12	9.7	21.7	2.3	1.8	1.1	2.3	1.7	1.1	12.1
2	18.2	3.8	6.5	8.5	0.6	0.6	0.4	0.6	0.7	0.5	4.4
3	47.3	12.4	11.6	24	1.8	1.1	2.2	1.5	1.3	14.2	2.942
4	40.5	10.7	9.2	20.5	2.2	1.6	1.2	1.9	1.3	1.2	11.7
5	47.9	13.1	10.9	24.1	2.2	1.5	1.1	2.2	1.6	1.2	13.9
6	42.2	11.1	11.4	20.1	1.9	1.6	1.2	2.2	1.5	1.1	11.4
7	37.7	9.9	8.8	19	2	1.6	1.3	1.9	1.7	1	10.8
8	43.4	12.7	9.4	21.4	2.1	1.5	1.2	2.1	1.5	1	12.4
9	44.1	12.4	9.3	22.8	2.3	1.6	1.1	2.1	1.6	1.5	13
10	43.4	10.5	12.9	19.3	1.6	1.4	0.9	1.8	1.5	1	11
11	49.27	12.84	11.72	24.46	2.26	1.55	1.21	2.23	1.6	1.25	13.78
12	26.67	6.11	6.37	14.07	1.35	0.98	NA	1.39	1	0.72	7.65
13	45.25	11.64	10.12	23.46	2.26	1.56	1.16	2.25	1.65	1.21	13.02
14	36.49	9.52	7.14	19.98	2.05	1.45	1.07	2.01	1.33	0.9	10.61
15	25.38	6.09	5.28	13.99	1.53	0.92	0.7	1.44	0.95	0.73	7.2
16	38.98	9.83	8.52	20.47	2.04	1.49	1.07	2.08	1.48	1.09	10.96
17	31.52	10.05	10	19.8	2.05	1.4	1.13	1.98	1.43	1.01	10.63
18	35.68	9.16	7.87	17.76	1.72	1.21	1.01	1.75	1.18	0.98	9.52
19	39.84	10.05	10	19.8	2.05	1.4	1.13	1.98	1.43	1.01	10.63
20	47.56	12.31	11.93	23.29	2.35	1.64	1.32	2.34	1.56	1.27	12.54
21	50.45	12	15.81	22.36	2.13	1.56	1.23	2.16	1.57	1.21	12.52

Table B.1: Measured masses of body parts of 21 *Cephalotes atratus* workers, in mg. Legs are identified using a code in the form AB, where A is a member of [R,L] and indicates right and left side, and B is a member of [F,M,H] and specifies fore-, mid- or hind-leg.

B.4 Allometric scaling

The morphometric dataset was used to determine whether the lengths of the body parts scale isometrically with body mass. For this analysis, the morphometric data were log-transformed, and linear regression analysis was used to measure how various length dimensions scale was body mass. If a given length L dimension scales isometrically with mass M, it is expected that $L \propto M^{\frac{1}{3}}$ (Alexander, 2003). Taking the logarithmic transform of this equation gives $\log L = 0.33 \log M$ — that is, if L is plotted against M on a log-log scale, L scales isometrically if the slope of this line is equal to 0.33. Slopes that deviate from the 0.33 value indicate allometric rather than isometric scaling, whereby L does not scale geometrically as M increases. If the slope is less than 0.33, this indicates that the dimension L is relatively shorter for individuals with higher M, and vice versa for slopes greater than 0.33.

In Figure B.1, covariance plots are presented for total body mass and all measured lengths (width and depth measurements of the head, trunk and gaster are omitted). To determine whether length dimensions scale isometrically in *C. atratus*, linear regressions were fit to the log transforms of the measured dimensions and body mass and the computed slope was recorded. The results of this analysis are tabulated in Table B.4. On the basis of the available measurements, trunk length and gaster length scale approximately isometrically with body mass. Head length and leg lengths, on the other hand, appear to scale as $L \propto M^{\sim\frac{1}{4}}$. This implies that, within the range of measured body masses, larger ants have relatively shorter legs than smaller ants.

B.5 Summary of analysis

A morphometric analysis of 21 *C. atratus* workers revealed that, within the range of masses represented, leg length scales allometrically with size: relative to their size, larger *C. atratus* workers have shorter legs than smaller *C. atratus* workers. The lengths of all legs were found to scale according to $L \propto M^{\sim\frac{1}{4}}$.

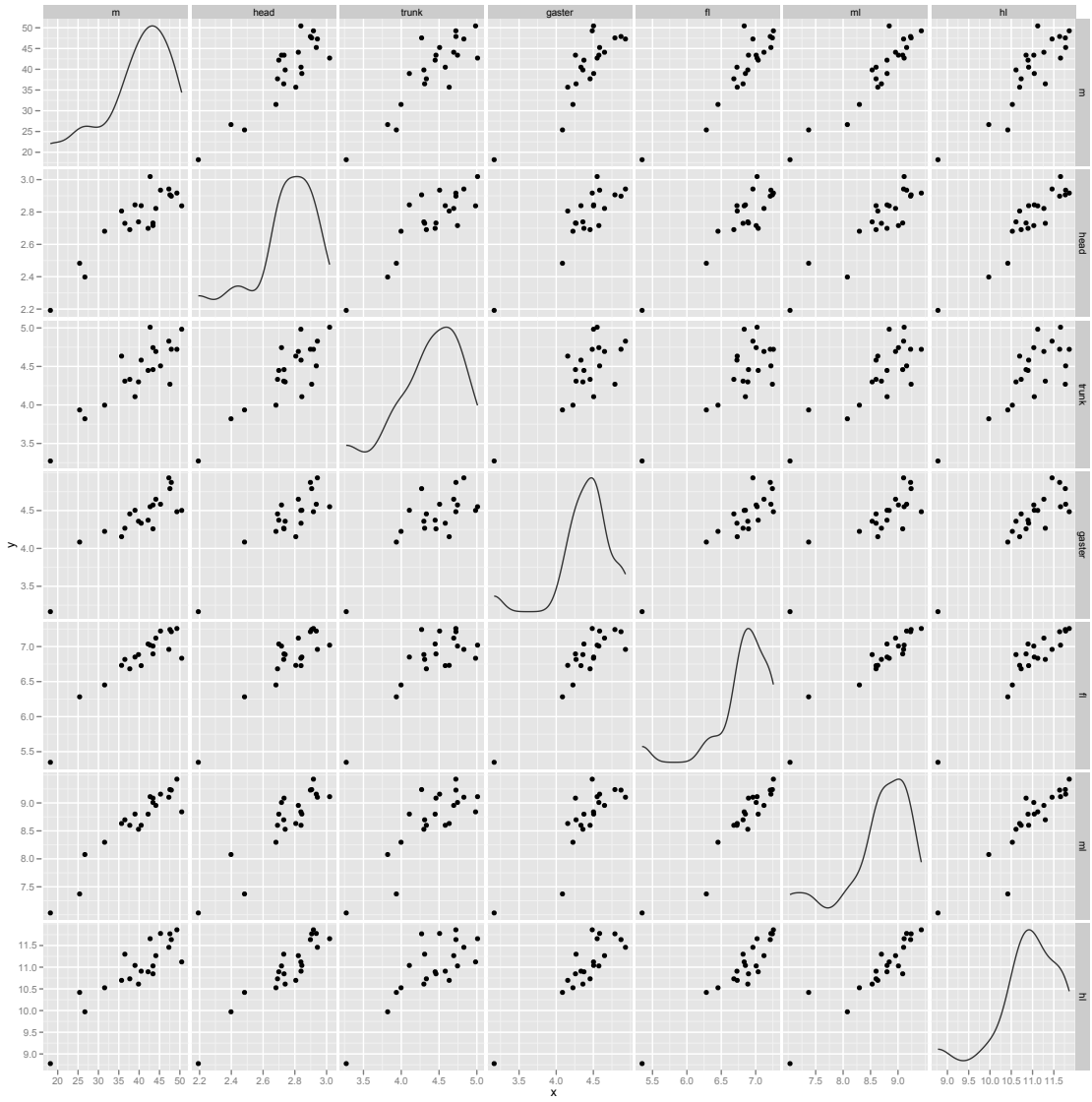

Figure B.1: Covariance plots for mass, lengths of axial body parts, and leg lengths. Kernel density of the variable is shown along the diagonal.

Ant ID	HL	HW	HD	TL	TW	TD	GL	GW	GD
1	3.568	3.522	1.954	5.009	2.556	1.771	4.551	3.553	2.818
2	2.192	2.326	1.437	3.272	1.654	1.179	3.165	2.928	2.214
3	3.606	2.051	4.828	2.516	1.918	4.932	3.811	2.814	11.564
4	2.839	3.193	2.039	4.582	2.543	1.568	4.333	3.587	2.558
5	2.898	3.602	2.26	4.723	2.627	1.679	4.872	3.86	2.825
6	2.699	3.259	2.178	4.448	2.307	1.581	4.373	3.489	2.721
7	2.691	3.138	2.016	4.332	2.413	1.65	4.456	3.522	2.458
8	2.716	3.433	2.157	4.744	2.376	1.721	4.574	3.612	2.755
9	2.822	3.491	2.239	4.694	2.55	1.7	4.65	3.598	2.861
10	2.732	3.274	2.085	4.459	2.309	1.572	4.259	3.515	2.733
11	2.917	3.625	2.289	4.722	2.597	1.737	4.485	3.672	2.787
12	2.398	2.965	1.711	3.82	2.096	1.43	NA	NA	NA
13	2.935	3.643	2.185	4.507	2.506	NA	4.584	3.562	2.809
14	2.73	3.292	1.892	4.309	2.304	1.544	4.267	3.583	2.755
15	2.483	2.931	1.771	3.935	2.088	1.573	4.084	3.48	2.321
16	2.844	3.545	2.026	4.107	2.416	1.499	4.504	3.569	2.768
17	2.681	3.112	1.854	3.997	2.21	1.301	4.225	3.364	2.401
18	2.806	3.29	1.981	4.634	2.351	1.504	4.155	3.538	2.538
19	2.739	3.195	2.06	4.299	2.382	1.901	4.359	3.493	2.601
20	2.906	3.465	1.991	4.269	2.496	1.711	4.179	3.552	2.609
21	2.838	3.378	2.078	4.983	2.53	1.838	4.502	3.593	2.582

Table B.2: Length, width and depth measurements for the axial body parts of the ants in mm. Measurements are coded in the form AB, where A is a member of [H,T,G] and specifies head, trunk or gaster, and B is a member of [L, W, D] and specifies length, width or depth.

Ant ID	RH	RM	RF	LH	LM	LF
1	11.566	9.134	5.347	11.748	9.09	5.251
2	8.931	7.196	5.386	8.624	6.869	5.311
3	9.122	7.112	11.353	9.082	6.807	NA
4	10.945	8.581	6.506	10.871	8.62	6.949
5	11.618	8.992	7.255	11.655	9.467	7.169
6	10.818	8.783	7.058	10.97	8.816	7.015
7	10.657	8.408	6.819	10.808	8.792	6.546
8	11.212	8.976	7.159	10.846	9.04	6.855
9	11.219	8.997	7.155	11.313	8.914	7.086
10	NA	9.211	6.87	11.19	10.505	6.92
11	11.88	9.532	7.312	11.844	9.318	7.203
12	10.149	8.107	NA	9.794	8.048	5.993
13	11.874	9.365	7.254	11.681	8.949	7.189
14	11.398	8.723	6.733	11.202	8.673	6.9
15	10.557	NA	6.12	10.28	7.372	6.445
16	11.087	8.618	6.838	10.994	8.984	6.863
17	10.42	8.367	6.474	10.631	8.226	6.43
18	10.901	8.632	6.779	10.492	NA	6.684
19	10.648	8.485	6.857	10.574	8.573	6.914
20	11.61	9.254	7.323	11.929	9.224	7.163
21	11.278	8.876	6.901	10.965	8.804	6.765

Table B.3: Leg lengths in mm. Measurements are coded in the form AB, where A is a member of [R,L] and indicates right and left side, and B is a member of [F,M,H] and specifies fore-, mid- or hind-leg.

	Slope vs log(Total Mass)	Std Error	R^2
log(Head Length)	0.272	0.028	0.84
log(Trunk Length)	0.354	0.041	0.8
log(Gaster Length)	0.338	0.039	0.81
log(Fore-leg Length)	0.263	0.022	0.89
log(Mid-leg Length)	0.274	0.02	0.91
log(Hind-leg Length)	0.243	0.026	0.82

Table B.4: